

Doctoral dissertation

Prepared in the Institute of Physics of the Jagiellonian University

Submitted to the Faculty of Physics, Astronomy and Applied Computer
Science of the Jagiellonian University



Methods to control systematic uncertainties in search
of EDM in storage ring

Anjali Aggarwal

Supervised by:
prof. dr hab. Andrzej Magiera

Cracow 2022

Wydział Fizyki, Astronomii i Informatyki Stosowanej
Uniwersytet Jagielloński

Oświadczenie

Ja niżej podpisana Anjali Aggarwal (nr indeksu: 1142424) doktorantka Wydziału Fizyki, Astronomii i Informatyki Stosowanej Uniwersytetu Jagiellońskiego oświadczam, że przedłożona przeze mnie rozprawa doktorska pt. "Methods to control systematic uncertainties in search of EDM in storage ring." jest oryginalna i przedstawia wyniki badań wykonanych przeze mnie osobiście, pod kierunkiem prof. dr. hab. Andrzej Magiera. Pracę napisałam samodzielnie.

Oświadczam, że moja rozprawa doktorska została opracowana zgodnie z Ustawą o prawie autorskim i prawach pokrewnych z dnia 4 lutego 1994 r. (Dziennik Ustaw 1994 nr 24 poz. 83 wraz z późniejszymi zmianami).

Jestem świadoma, że niezgodność niniejszego oświadczenia z prawdą ujawniona w dowolnym czasie, niezależnie od skutków prawnych wynikających z ww. ustawy, może spowodować unieważnienie stopnia nabytego na podstawie tej rozprawy.

Kraków, dnia 31.05.2022

.....

Abstrakt

Metoda określenia wartości elektrycznego momentu dipolowego (EDM) cząstek naładowanych przy wykorzystaniu synchrotronu polega na pomiarze wertykalnej składowej polaryzacji dla początkowo horyzontalnie spolaryzowanej wiązki. Kolaboracja JEDI (Jülich Electric Dipole Moment Investigation) prowadzi badania zmierzające do pomiaru EDM protonu i deuteronu przy wykorzystaniu synchrotronu COSY. Te pilotażowe badania powinny pozwolić na wyznaczenie dolnej granicy wartości EDM 10^{-19} e-cm dla tych cząstek. Pomiary prowadzone są na synchrotronie COSY w Forschungszentrum, Jülich. Kolejnym krokiem będzie budowa nowego synchrotronu w FZ Jülich pozwalającego na dokładniejszy pomiar. W dalszej perspektywie planowana jest budowa docelowego synchrotronu w CERN w ramach kolaboracji cpEDM. Docelowo powinno to pozwolić na pomiar EDM protonu i deuteronu z dokładnością 10^{-29} e-cm. Taka dokładność ze względu na statystykę pomiaru jest możliwa do osiągnięcia, natomiast konieczne jest określenie wielkości niepewności systematycznych.

Celem tej rozprawy doktorskiej jest opacowanie metod pozwalających na dokładne określenie niepewności systematycznych w planowanych pomiarach EDM dla protonu i deuteronu. W rozprawie zaproponowano dwie metody pozwalające na określenie tych niepewności. Pierwsza metoda wykorzystuje oddziaływanie elektrycznego momentu kwadrupolowego (EQM) z gradientami pól elektromagnetycznych i ma zastosowanie tylko w pomiarze z deuteronom. Oddziaływanie to daje taki sam efekt jakiego oczekuje się w pomiarze EDM, jakkolwiek wymagana jest zmiana ustawień pól magnesów synchrotronu. Wartość EQM deuteronu jest dobrze określona, więc jej odtworzenie w pomiarze powinno udowodnić dobrą kontrolę nad niepewnościami systematycznymi. W pracy pokazano zastosowanie tej metody dla jednej z propozycji pomiaru EDM deuteronu. Druga zaproponowana metoda pozwala

na określenie niepewności systematycznych powodowanych niewspółosiowością magnesów synchrotronu. Nawet niewielkie odchylenia ustawień magnesów powodują powstanie takiego samego efektu jak indukowany przez EDM. Wielkość tego fałszywego efektu może być istotnie większa od sygnału oczekiwanego od EDM. Przedstawiona metoda polega na analizie Fouriera czasowego przebiegu wertykalnej składowej polaryzacji wiązki w synchrotronie. Zastosowanie tej metody wymaga próbkowanie tej polaryzacji w dwóch oddalonych od siebie miejscach, czyli konieczna jest instalacja dwóch polarymetrów. W pracy przedstawiono zastosowanie tej metody dla pomiaru EDM na synchrotronie COSY. Pokazano iż dla obecnej precyzji ustawienia magnesów COSY możliwe jest wyznaczenie wartości EDM deuteronu z dokładnością 10^{-19} e·cm. Przedstawiona metoda może być zastosowana do dowolnych pomiarów EDM, które wymagają użycia pierścienia akumulacyjnego.

Abstract

The method of determining the value of the electric dipole moment (EDM) of charged particles using a synchrotron consists of measuring the vertical component of polarisation for an initially horizontally polarised beam. The JEDI (Jülich Electric Dipole Moment Investigation) collaboration conducts research aimed at measuring the EDM of the proton and deuteron using the COSY synchrotron. These pilot studies should allow to obtain an EDM lower limit of 10^{-19} e·cm for these particles. Measurements are ongoing at the COSY synchrotron at Forschungszentrum, Jülich. The next step will be the construction of a new synchrotron at FZ Jülich, allowing for more accurate measurements. In the longer term, it is planned to build a target synchrotron at CERN as part of the cpEDM collaboration. Ultimately, this should allow the EDM of the proton and deuteron to be measured with an accuracy of 10^{-29} e·cm. Due to the measurement statistics, such accuracy is possible to achieve, but it is necessary to determine the magnitude of the systematic uncertainty.

The aim of this doctoral dissertation is to develop methods to accurately determine systematic uncertainties in planned EDM measurements for proton and deuteron. In the dissertation, two methods were proposed for the determination of these uncertainties. The first method uses the interaction of electric quadrupole moment (EQM) with electromagnetic field gradients and is only applicable to the measurement with deuteron. This interaction has the same effect as expected in an EDM measurement, although a change in the settings of the synchrotron magnet fields is required. The deuteron EQM value is well known, so its reproduction in the measurement should prove good control over systematic uncertainties. The thesis shows the application of this method for one of the proposed deuteron EDM measurements. The second proposed method allows for the determination of systematic uncer-

tainties caused by the misalignment of the synchrotron magnets. Even slight variations in the settings of the magnets produce the same effect as induced by EDM. The magnitude of this false effect may be significantly greater than the signal expected from the EDM. The presented method is based on the Fourier analysis of the time dependence of the vertical component of the beam polarisation in the synchrotron. The use of this method requires sampling of this polarisation at two distant places, i.e., it is necessary to install two polarimeters. The thesis presents the application of this method for EDM measurement on the COSY synchrotron. It has been shown that for the current precision of COSY magnets positioning, it is possible to determine the EDM value of a deuteron with an accuracy of 10^{-19} e·cm. The presented method can be applied to any EDM measurements that require the use of a storage ring.

Dedication

This work is dedicated to my parents. My father and my late mother, who believed in me and inspired me.

Acknowledgements

I would like to show my gratitude to many people who have been a part of my journey and helped me throughout the process of completing my dissertation.

First and foremost, I want to express my gratitude to my supervisor, Prof. dr hab. Andrzej Magiera, for giving me the opportunity to join his JEDI collaboration group in Poland. Thanks to his great patience, guidance, and support throughout this journey, and for continuing to have faith in me over these years.

Furthermore, I'd like to express my gratitude to the JEDI collaboration for allowing me to be a part of this prestigious collaboration. Thank you for inviting me to participate in such interesting precursor experiments and lively discussions. I want to thank Dr. Vera Poncza in particular for her assistance in getting me acquainted with the BMAD software and delivering me the required information at the beginning of my PhD.

I would also like to thank all my colleagues and friends for making this journey memorable and easy. Most importantly, I would like to thank Dr. Udai Singh for his constant support and motivation during the years of my Ph.D. studies. His endless efforts helped me finish this work. Without him, I would not have completed my dissertation. Along with that, I would like to thank my another friend, Chetna Khosla, for being there for me to understand, listen to, and never let go. I also would like to thank my first roommate and friend, Dr. Jaya Sravanthi Mokappati, for teaching me how to be a nice human being and be successful at the same time.

Last but not least, I'd like to express my gratitude to my entire Aggarwal family for being my support system. Especially my father, Mr. Subhash Ag-

garwal, who believed in me, allowed me to pursue my dreams, and provided me with the best life lessons. I thank my late mother, Mrs. Raj Rani Aggarwal, from the bottom of my heart for giving me birth and providing me with the best upbringing. I'd also like to thank my elder brothers, Mr. Atul and Rahul Aggarwal, and sisters-in-law, Mrs. Shikha Aggarwal and Richa Aggarwal, for their unconditional love and motivation during my difficult times. I'd also like to thank my nephews and nieces (Karthik, Riyanshi, Raghavi, and Tanush Aggarwal) for their beautiful smiles, which give me strength and inspire me to keep going.

Contents

1	Introduction	12
2	Theory and Motivation	15
2.1	Baryons-Antibaryons Asymmetry	15
2.2	Discrete Symmetries And Their Violations	16
2.2.1	Parity Transformation	16
2.2.2	Charge Conjugation Transformation	17
2.2.3	Time Reversal Transformation	18
2.2.4	\mathcal{CP} Symmetry Violation	18
2.3	Electric Dipole Moment	19
2.3.1	Definition Of EDM	19
2.3.2	EDM Leads To \mathcal{CP} Violation	20
2.4	Current EDM Limits	20
2.5	JEDI Collaboration	22
3	Beam and Spin Dynamics In Storage Ring	24
3.1	Beam Physics	24
3.1.1	Lorentz Force	25
3.1.2	Coordinate System	25
3.2	Beam Dynamics	27
3.2.1	Transverse Motion	27
3.2.2	Beta Function And Betatron Oscillation	32
3.2.3	Beam Emittance And Betatron Tune	35
3.2.4	Longitudinal Motion	37
3.3	BMAD Software	39
3.4	Spin Dynamics	40
3.4.1	Polarisation Formalism	40
3.4.2	Spin $\frac{1}{2}$ Particles	40

3.4.3	Spin 1 Particles	42
3.5	Spin Motion In Storage Ring	43
3.5.1	Spin Evolution In Electric And Magnetic Field	44
3.5.2	Spin Precession – TBMT Equation	44
3.6	Methods Proposed For EDM Measurement In Storage Ring . .	47
3.6.1	Basic Idea Of EDM Measurement	47
3.6.2	Frozen Spin Method	49
3.6.3	Quasi Frozen Spin Method	50
3.6.4	RF Wien Filter Method (Partially Frozen Spin)	54
4	Method To Control Systematics And Its Effects On Spin Pre- cession	56
4.1	QFS Lattice	57
4.1.1	Optical Functions	59
4.2	BMAD Simulations For Quasi-Frozen Spin Method	61
4.2.1	New Method For Controlling Systematics	61
4.2.2	Extending TBMT Equation	61
4.2.3	Realistic Electromagnetic Field Definition	63
4.3	2D Analytical Field Equations	65
4.4	3D Analytical Field Equations	68
4.4.1	Dipole Field	68
4.4.2	Quadrupole Field	69
4.4.3	Field For Wien Filter	73
4.4.4	Realistic Field For Two Quadrupoles (Superimposition Of Quadrupoles)	73
4.5	Spin Tracking	76
4.6	Results And Discussion	78
5	Method For Evaluating Systematic Uncertainties Due To Magnet Misalignment In EDM Measurements Using A Stor- age Ring	80
5.1	The Cooler Synchrotron COSY Accelerator Facility	81
5.2	Lattice Of COSY	84
5.3	Analytical Calculation Using Mathematica	86
5.4	Fourier Analysis Of Vertical Spin Component	89
5.5	BMAD Simulations For EDM And Misalignment Effects . . .	92
5.5.1	Magnets Misalignment Introduction	93
5.5.2	Effect Of Emittance On Vertical Spin Component	95

5.5.3	Orbit Correction By Replacing Kickers With Dipole Magnets	96
5.6	EDM Limit Determination Using Fourier Analysis	98
5.7	EDM Limit Determination Using Fourier Analysis And Slope Induced By Wien Filter	102
5.8	Result And Conclusion	104
6	Summary	106
A	Derivatives For Quadrupole For The Full Half-Symmetric Function	114

Chapter 1

Introduction

One of the intriguing problems in particle physics is the asymmetry of matter and antimatter in the universe. The asymmetry of matter and antimatter can exist only if a number of conditions are fulfilled, known as the Sakharov conditions [1]. One of the important Sakharov conditions is \mathcal{CP} symmetry violation. Many sources have been known so far for \mathcal{CP} symmetry violations and can be introduced into the Standard Model. However, these sources are inadequate to explain the observed asymmetry of baryons. This leads to the search for more \mathcal{CP} symmetry violation sources.

A fundamental particle or an atom's permanent electric dipole moment (EDM) violates time-reversal symmetry and hence violates \mathcal{CP} symmetry according to \mathcal{CPT} theorem. To explain the additional causes of \mathcal{CP} violation, some new physics beyond the Standard Model would be necessary and lead us closer to a solution to the baryon asymmetry. The study of the search for the EDM of many elementary particles is in process. However, the particle's EDM upper limits are only known. The Jülich Electric Dipole Moment Investigation (JEDI) collaboration [2] is working on one of these measurements, which aims to determine the EDM limit of protons and deuterons at the Cooler Synchrotron (COSY) storage ring at Forschungszentrum, Jülich. The collaboration is also involved in designing and proposing methods to perform this investigation. The physics scenario, precursor experiment, and future plans are discussed in further detail in [3] and a precursor experiment has already been set up.

The concept behind this measurement is to observe the vertical polarisation component induced by an EDM for an initially horizontally polarised beam. However, systematic uncertainties are undeniable and will eventually lead to fake EDM signals. For such high precision experiments, it is necessary to find methods to control systematics. The aim of this thesis is to develop methods to control systematic uncertainties. In this study, two methods for controlling systematic uncertainties have been proposed. The first method is based on the measurement of electric quadrupole moment (EQM) interaction with field gradients, which has the same effect as electric dipole moment (EDM). Using a different setup of Wien filter fields allows us to separate the EQM contribution from the true EDM effect. Because the EQM value is known with high accuracy, reproducing it using the same method as in the EDM search will demonstrate that systematic uncertainties can be controlled to the required level. The second method discussed is to evaluate the systematic uncertainties due to magnet misalignment in the storage ring. This is a very important source of systematic uncertainties that can mimic the EDM effect. Even with very small magnet misalignments, this false signal might be much larger than the expected EDM signal. A Fourier analysis of the time-dependent vertical polarisation is used to evaluate the magnitude of this effect. This might be accomplished by sampling the vertical polarisation at a frequency greater than the beam revolution frequency, resulting in polarisation measurements in at least two positions in the storage ring. This method can be applied to any case for EDM measurements utilising a storage ring.

This thesis is divided into six chapters.

- Chapter 2 discusses in detail baryon-antibaryon asymmetry, discrete symmetries in physics, \mathcal{CP} symmetry violation, how EDM leads to \mathcal{CP} violation and a summary of previous EDM experiments and their results.
- Chapter 3 discusses in detail beam and spin dynamics in the storage ring. Also, the equations of motion that describe particle trajectories and the time-dependent evolution of spin in electromagnetic fields. The methods proposed for EDM measurement in the storage ring are also discussed.

- Chapter 4 discusses the first method to control systematic uncertainty using the interaction of electric quadrupole moment (EQM) and magnetic dipole moment (MDM) with electromagnetic field gradients. Also, it discusses particle and spin tracking simulations by introducing realistic fields and defining their gradients, as well as extending the TBMT equation to evaluate the true effect of MDM and EQM interaction with field gradients using BMAD software for Quasi Frozen Spin lattice (QFS lattice).
- Chapter 5 focuses on systematic uncertainties due to magnet misalignment in the storage ring. In order to estimate the systematic uncertainties due to magnet misalignment, simulations using BMAD software for the Cooler Synchrotron (COSY) storage ring were performed. A simple analytical model is also discussed that allows to directly determine the effect of magnet misalignment on the vertical spin component. A Fourier analysis of the time-dependent vertical polarisation is used to estimate the effect of the magnet's misalignments on the expected EDM signal.
- Chapter 6 concludes with a summary of the thesis.

Chapter 2

Theory and Motivation

The dissertation was completed as part of the JEDI collaboration [2]. The collaboration's main objective is to study feasible experiments for measuring charged particles' EDM in storage rings. This chapter discusses why EDMs are of particular interest in particle physics, what leads to baryon-antibaryon asymmetry, and a discussion regarding discrete symmetries in physics and a summary of previously conducted EDM experiments and their outcomes.

2.1 Baryons-Antibaryons Asymmetry

Our universe is matter-dominated, with more matter than antimatter. This disparity between matter and antimatter is frequently referred to as the baryon asymmetry problem. The matter and antimatter asymmetry is described using a parameter η known as the baryon asymmetry parameter:

$$\eta = \frac{N_B - N_{\bar{B}}}{N_\gamma} \quad (2.1)$$

where N_B denotes the number of baryons, $N_{\bar{B}}$ denotes the number of antibaryons, and N_γ denotes number of photons. After the Big Bang, the universe's temperature reached a point where pair formation and annihilation occurred in thermal equilibrium. After the temperature went below the threshold for pair production, matter and anti-matter annihilated and photons were created, resulting in $2N_\gamma \approx N_B + N_{\bar{B}}$. The number for η is estimated to be around $(6.047 \pm 0.074) \cdot 10^{-10}$ according to the Cosmic Microwave Background (CMB) spectrum, although the current model of particle physics

and cosmology allows for only a value of $1 \cdot 10^{-18}$. This mismatch indicates that there must be some information not yet known. To explain this cosmic enigma, Andrei Sakharov [1] proposed three conditions for baryogenesis to occur:

1. **Baryon number violation:** At the beginning of the Big Bang, the universe was symmetric, which means baryon number $B = 0$ ($B = N_B - N_{\bar{B}}$). Therefore, in order to do transition from a symmetric to an asymmetric universe, baryon number must be violated, which means that the system must evolve from baryon number $B = 0$ to baryon number $B \neq 0$.
2. **\mathcal{C} and \mathcal{CP} symmetries violation:** Only a violation of the baryon number is insufficient to account for matter-antimatter asymmetry. If \mathcal{C} and \mathcal{CP} symmetries are not violated, baryons are formed at the same rate as anti-baryons, and hence no baryon asymmetry develops.
3. **Interaction outside of thermal equilibrium:** In order to transit from $B = 0$ to $B \neq 0$ state, the system must be brought out of thermal equilibrium, since an equilibrium state attempts to maintain an equal quantity of baryons and anti-baryons, making transit from one state to another difficult. As a result, baryogenesis should occur in the absence of thermal equilibrium.

2.2 Discrete Symmetries And Their Violations

Symmetry conservation is a critical aspect of physics [4]. Presently, there is considerable interest in the investigation of symmetry violations. In particle physics, the discrete symmetries are as follows: parity transformation \mathcal{P} , charge conjugation \mathcal{C} , and time reversal \mathcal{T} symmetry.

2.2.1 Parity Transformation

The parity transformation \mathcal{P} changes the sign of a single spatial coordinate. A process being symmetric under the parity transformation means that it behaves identically to its mirror image process. The parity transformation has an effect on polar vectors such as displacement, momentum, and acceleration but has no effect on axial vectors such as angular momentum. When

it comes to the electromagnetic field, the \mathcal{P} transformation reverses the direction of the electric field vector, while the direction of the magnetic field vector keeps their orientation since they are represented by axial vectors [5].

In the Standard Model, electromagnetic and strong interactions are symmetric under \mathcal{P} transformation, but weak interactions violate \mathcal{P} transformation. Following the discovery of K^+ meson decays into final states of two and three pions, Lee and Yang [6] proposed investigating β decays to explore parity violation in weak interactions in 1956. Later that year, Wu performed an experiment [7] to establish parity conservation in weak interaction. The aim was to measure the angular distribution of electrons for emission angles relative to the polarised nucleus spin direction. In that experiment, the beta decay of a polarised cobalt was observed:

$${}^{60}\text{Co} \rightarrow {}^{60}\text{Ni} + e^- + \tilde{\nu}_e. \quad (2.2)$$

It was seen that no matter what the sign of the polarising field was, the ejected electrons were more favoured to travel in the direction opposite to the nuclear spin. Because the parity transformation has no effect on the polarisation direction but affects the momentum and hence the flight direction, the measurement provides evidence of parity violation. Furthermore, investigations of charged pion decays revealed that the neutrino spin is always anti-aligned to the momentum vector, whereas the anti-neutrino spin points in the direction of the flight. Therefore, left-handed neutrinos and right-handed anti-neutrinos couple to the weak interaction in the SM if massless neutrinos are assumed [8, 9].

2.2.2 Charge Conjugation Transformation

In this transformation, all particles are replaced with their corresponding antiparticles. As a result, additive quantum numbers like charge, baryon, and lepton number, as well as strangeness, are reversed, but other quantities like spin, position, and momentum remain unaffected. Charge inversion leads to a change in the direction of electric and magnetic fields. In SM, weak interactions violate the \mathcal{C} symmetry, e.g. in pion decay:

$$\pi^+ \rightarrow \mu_L^+ + \nu_{\mu,L} \xrightarrow{\mathcal{C}} \pi^- \rightarrow \mu_L^- + \tilde{\nu}_{\mu,L}. \quad (2.3)$$

A left-handed anti-neutrino does not participate in weak interaction in SM. Thus, pion decay is an example of the weak interaction violating \mathcal{C} symmetry.

2.2.3 Time Reversal Transformation

Time reversal transformation inverts the time coordinate's sign while keeping the spatial coordinates the same. It is the third discrete transformation. The particular reaction rate for a time symmetric process should be the same as the reverse reaction rate. There is no evidence of the presence of time violation in strong and electromagnetic interaction. Violation of time reversal transformation symmetry was observed in weak interactions, such as in the decay of neutral kaons [10].

2.2.4 \mathcal{CP} Symmetry Violation

\mathcal{CP} violation is the violation of combined \mathcal{C} and \mathcal{P} symmetries, i.e. a simultaneous violation of both charge conjugation and parity symmetries. The \mathcal{CP} symmetry states that if a particle is interchanged with its antiparticle (\mathcal{C} symmetry), and the coordinates are inverted, i.e. mirror image (\mathcal{P} symmetry), the laws of physics should remain the same.

In 1951, Schwinger [11] implicitly introduced the \mathcal{CPT} -theorem, which states that if a local quantum field theory is Lorentz invariant, the combination of \mathcal{C} , \mathcal{P} , and \mathcal{T} transformations in any order is conserved. As a result, one can determine that a violation of the \mathcal{T} symmetry directly results in a violation of the \mathcal{CP} symmetry in order to conserve the \mathcal{CPT} theorem. In 1964, Cronin and Fitch [12] discovered the first instance of a process that violated the \mathcal{CP} while measuring the decay of the K_L^0 kaon. The K_L^0 can decay into two and three pion final states, but not into a two pion final state if the K_L^0 is a \mathcal{CP} eigenstate. To include this effect in Standard Model theory, the CKM matrix (Cabibbo-Kobayashi-Maskawa) [13][14] was proposed, which explains the mixing of the six quarks, where complex phase causes \mathcal{CP} violation. The \mathcal{CP} violation was also observed in the B meson sector [15][16]. Due to the fact that the \mathcal{CP} violation in the CKM matrix alone is insufficient to account for the matter-antimatter asymmetry, other sources of \mathcal{CP} violation are of significant interest. The EDM is one such option, which will be described in further detail.

2.3 Electric Dipole Moment

EDM is a fundamental property of particles, much like spin, charge, and mass. The presence of a permanent EDM in a non-degenerated system might be an additional source of \mathcal{CP} violation and contribute to our understanding of matter dominance in the universe. This chapter provides a short introduction of the theoretical background of EDMs as well as an overview of EDM measurements and their outcomes in general.

2.3.1 Definition Of EDM

The electric dipole moment (EDM) is a term that refers to the permanent separation of two charges inside a system. Thus, EDM (d) for two opposite charged particles (q) placed at a distance (r) is defined classically as follows:

$$\vec{d} = q\vec{r}. \quad (2.4)$$

Due to asymmetry in charge density distribution, $\rho(\vec{x})$ EDM arises in a system, which can be represented as:

$$d = \int_V \rho(x) x d^3x. \quad (2.5)$$

Similarly, the magnetic dipole moment (MDM) is defined as follows:

$$\mu = \frac{1}{2} \int_V [x \times j(x)] d^3x. \quad (2.6)$$

The current density is denoted by $\vec{j}(\vec{x})$. EDM and MDM can be parallel or anti-parallel to the spin direction, as this is the only quantization axis that can be distinguished. The EDM and MDM are spin-dependent, as shown by [17]:

$$\vec{d} = \eta_{EDM} \cdot \frac{q}{2mc} \vec{S} \quad (2.7)$$

$$\vec{\mu} = g \cdot \frac{q}{2m} \vec{S} \quad (2.8)$$

where q denotes the charge of the particle, \vec{S} denotes the spin, m denotes the mass of the particle, c denotes the speed of light, and g denotes the dimensionless scaling parameter known as the g -factor. In the case of EDM, the dimensionless scaling parameter is η_{EDM} , which denotes the EDM magnitude.

2.3.2 EDM Leads To \mathcal{CP} Violation

EDM is oriented in the direction of charge distribution from negative to positive. This section will explain the relationship between \mathcal{CP} violations and EDM.

The Hamiltonian of the particle at rest in electric and magnetic fields is given by the relation (2.9):

$$\hat{H} = -\vec{\mu}\vec{B} - d\vec{E} \quad (2.9)$$

$$\mathcal{P}: \hat{H} = -\vec{\mu}\vec{B} + d\vec{E} \quad (2.10)$$

$$\mathcal{T}: \hat{H} = -\vec{\mu}\vec{B} + d\vec{E} \quad (2.11)$$

When the parity transformation is applied to the Hamiltonian (equation 2.10), the electric field is reversed while the magnetic field and spin remain unchanged, as depicted in figure 2.1. It is concluded that the permanent EDM results in a \mathcal{P} violation, while the MDM does not. Similarly, when a time reversal transformation is applied to the Hamiltonian (equation 2.11), the magnetic field's sign changes, the spin vector's direction is reversed, but the electric field is unaffected, as depicted in figure 2.1. Whereas, EDM and MDM point in the direction of the spin. As a result, the EDM term in equation 2.9 changes sign, indicating that permanent EDM results in \mathcal{T} violation [17]. Thus, a nonzero EDM value violates both the parity and time reversal symmetries. As a result of the \mathcal{CPT} theorem, an EDM violates the \mathcal{CP} since it violates both \mathcal{P} and \mathcal{T} .

2.4 Current EDM Limits

As EDM is a possible source of \mathcal{CP} violation, numerous measurements of elementary particle's EDM are currently ongoing or have been performed.

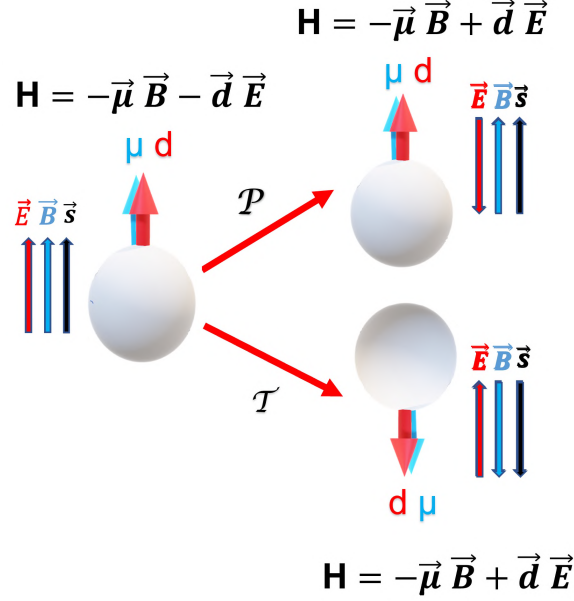


Figure 2.1: In this figure, \mathcal{P} represents parity transformation, and \mathcal{T} represents time reversal. The behaviour of the EDM (d) and MDM (μ) under \mathcal{P} and \mathcal{T} are depicted on the figure. Due to the fact that both the EDM and MDM are aligned with the spin, they behave identically under parity \mathcal{P} and time reversal \mathcal{T} transformations. But, the fields to which they couple (\vec{E} and \vec{B}) do not align. The electric field \vec{E} changes sign during the parity transformation (\mathcal{P}), while the magnetic field \vec{B} and spin direction remain unchanged, and also the EDM and MDM remain unchanged. This results in a change in the Hamiltonian's ($\vec{d}\vec{E}$) sign and a violation of the symmetry. The same holds true for time reversal (\mathcal{T}), in which everything other than the electric field's sign reverses, resulting in the same Hamiltonian as that after \mathcal{P} transformation and a violation of the symmetry.

Particle	Upper EDM limits
Neutron	$d_n \leq 3 \cdot 10^{-26}$ e·cm (90% C.L.) [18]
Electron	$d_e \leq 8.7 \cdot 10^{-29}$ e·cm (90% C.L.) [19]
Proton	$d_p \leq 7.9 \cdot 10^{-25}$ e·cm (95% C.L.) [20]
Muon	$d_\mu \leq 1.9 \cdot 10^{-19}$ e·cm (95% C.L.) [21]

Table 2.1: Measured upper limits for the EDM of different particles. So far, muon is the only one whose EDM limit was determined by a storage ring experiment [21].

For example, the neutron's EDM limit was first measured in 1957 by Smith, Ramsey, and Purcell, and the outcome was [22] $d_n = (0.1 \pm 2.4) \cdot 10^{-20}$ e·cm. A number of theories beyond SM predict non-zero EDMs of other particles. In order to confirm these theories and compare their predictions with experimental data, it is important to measure the EDM of numerous additional particles. Table 2.1 represents the current experimental upper limits for EDM of elementary particles. Jülich Electric Dipole Moment Investigations (JEDI collaboration) aims to investigate EDM for proton and deuteron particles. So far, the upper limit for the proton has only been determined indirectly, and there has been no measurement of the deuteron.

Neutral systems, in particular, neutrons, neutral molecules, or atoms, have been favored in many circumstances due to the relatively easy construction of a trapping system with minimal influence on translational motion from electromagnetic fields. Since the translational motion of charge particle can be effected by applied electromagnetic field, the process of trapping and analysing of charge particles becomes more challenging. As a result, new ways of measurement must be introduced [23]. The advantageous property of storage rings is that they can store and circulate charged particles for very extended beam lifetimes. Proposed methods of storage ring will be discussed in detail in section 3.6.

For charged hadrons, the Standard Model prediction for EDM's order of magnitude is 10^{-32} to 10^{-31} e·cm, which is too small to be measured by the proposed JEDI experiment [24]. But Standard Model extension such as supersymmetry [25, 26] predict a higher order of magnitude of EDM, which may surpass 10^{-29} e·cm, which is anticipated to be in the range of dedicated storage ring investigations.

2.5 JEDI Collaboration

JEDI (Jülich Electric Dipole Moment Investigations) was founded in 2011 with the objective of utilising COSY (Cooler Synchrotron) [27] not only for the development of key technologies for srEDM but also for the first direct EDM measurement of deuterons ("precursor experiment"). Due to the fact that COSY is a conventional storage ring with magnetic bending, it requires a particular insertion ("Radio-frequency (RF) Wien filter") to be sensitive

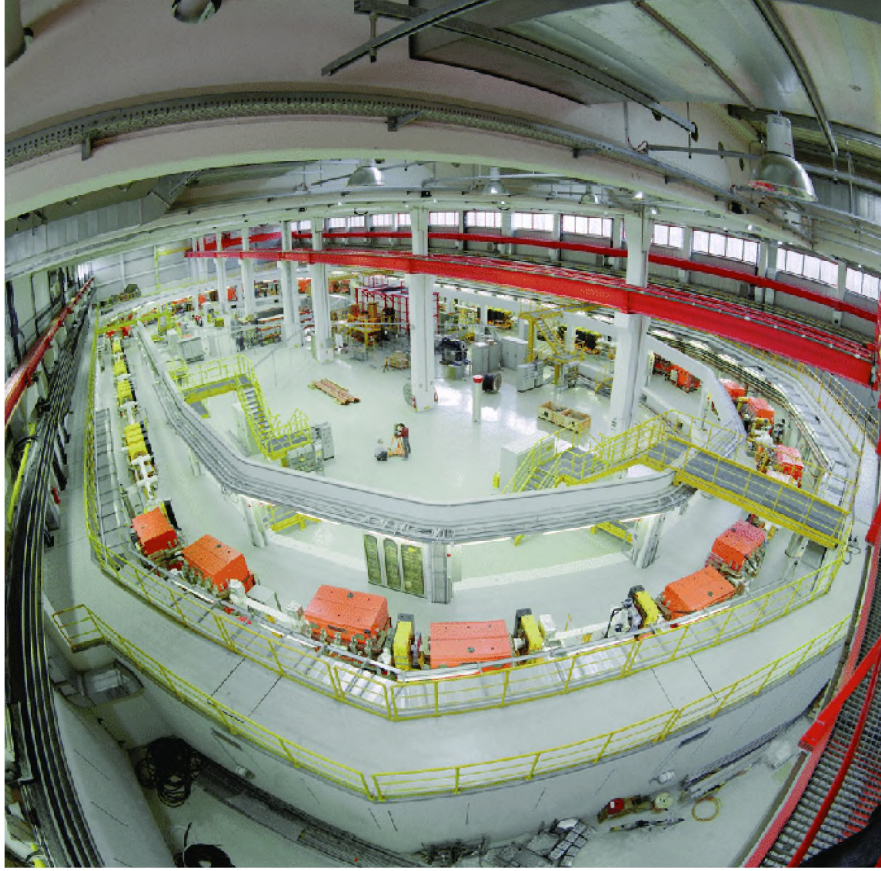


Figure 2.2: The Cooler Synchrotron (COSY) at Forschungszentrum Jülich, Germany.

to EDM. This latter research, which aims to demonstrate the feasibility of srEDM, is funded by an "Advanced Grant" from the "European Research Council" (2016–2021).

The JEDI collaboration has already gathered a lot of information [28–35], further research is ongoing [3, 28–36], and a precursor experiment has been set up. Whereas the statistical accuracy required to achieve a sensitivity of 10^{-21} e·cm for the EDM can be achieved in a short measurement. In order to reach this goal it is necessary to know the systematic uncertainties with sufficiently good precision.

Chapter 3

Beam and Spin Dynamics In Storage Ring

To comprehend the measurement methods of a charged particle's electric dipole moment (EDM) with the use of a storage ring, one must first understand the behavior of a particle beam as well as spin in a storage ring. Electric and magnetic fields have an influence on particle motion and spin precession as well as it keep particles in the storage ring. The evolution of the particle's path is described by beam dynamics. Spin dynamics, on the other hand, describes spin precession in the presence of electromagnetic fields. This chapter also discusses the coordinate system in a storage ring and is followed by an explanation of the interaction of particles with the electromagnetic field of different elements in a storage ring.

3.1 Beam Physics

A beam can be defined as an ensemble of particles. A particle's motion is generally defined by its momentum and position called a state vector, \vec{Z} . The coordinates of state vector \vec{Z} are known as **phase space coordinates** and are denoted as,

$$\vec{Z} = (x, p_x, y, p_y, z, p_z). \quad (3.1)$$

3.1.1 Lorentz Force

In an electromagnetic field, the force on the particle is represented by the Lorentz force,

$$F_L = q(\vec{E} + c\vec{\beta} \times \vec{B}), \quad (3.2)$$

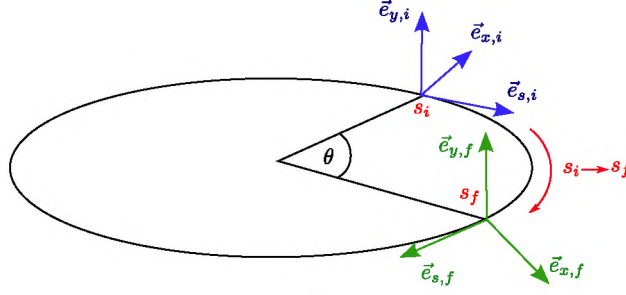
where the charge of the particle is q , magnetic and electric fields are given by \vec{B} and \vec{E} respectively, $c\vec{\beta}$ denotes the velocity of the particle. Both magnetic and electric fields can be used to bend charged particles in the storage ring. Additionally, an electric field can be utilised to accelerate the particles. However, magnetic fields are the most widely utilised for beam guidance. Since it is easier to generate a magnetic field of 1 T in comparison to an electric field of order $3 \cdot 10^9 \text{ V}\cdot\text{cm}^{-1}$ which corresponds to the same force acting on a relativistic particle. Because such large electric fields are technically impossible to make, magnetic bending components have been used almost extensively in the past. Since the transverse magnetic field has no effect on the change in longitudinal momentum, the electric field can be used to accelerate particles in the longitudinal direction.

3.1.2 Coordinate System

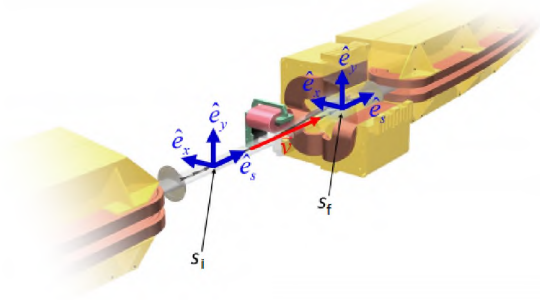
To describe the motion of particles in a storage ring, a predefined coordinate system is necessary. All of the elements in a storage ring have fixed positions and have either a static or variable field. So, it is more convenient to describe the position and other beam parameters as a function of the position s along the reference trajectory $\vec{r}_{ref}(s)$. A reference particle is defined as a particle that follows the reference orbit $\vec{r}_{ref}(s)$ of the beam with the reference momentum \vec{p}_{ref} to describe the motion of any arbitrary particle inside the storage ring.

A co-moving coordinate system $(\vec{e}_x, \vec{e}_y, \vec{e}_s)$ may be used to study the motion of an arbitrary particle with respect to the reference particle. The position of the reference particle acts as the origin of this coordinate system. Figure 3.1 (a) depicts a co-moving coordinate system on the reference orbit from a starting point s_i to a final point s_f . The momentum of the reference particle \vec{p}_{ref} is always aligned with the basis vector \vec{e}_s . A transverse plane is defined

by the basis vectors \vec{e}_x , which is perpendicular to \vec{e}_s and points radially, and $\vec{e}_y = \vec{e}_s \times \vec{e}_x$, which points vertically. Figure 3.1 (b) helps in visualising the coordinates.



(a)



(b)

Figure 3.1: Figure (a) Geometrical view: The Cartesian coordinate system is co-moving with the reference particle and has its origin at the reference particle's position. The s -axis points tangentially to the reference orbit, whereas the z -axis is oriented radially, and y indicates vertical direction. Also, (x, y, s) coordinates are known as curvilinear coordinates. Figure (b) helps in visualising the coordinate system (the illustration is taken from [37]).

The coordinate system transformation from point s_i to another s_f are given by [38]:

$$\vec{e}_{x,f} = \cos \theta \vec{e}_{x,i} + \sin \theta \vec{e}_{s,i}, \quad (3.3)$$

$$\vec{e}_{y,f} = \vec{e}_{y,i}, \quad (3.4)$$

$$\vec{e}_{s,f} = -\sin\theta\vec{e}_{x,i} + \cos\theta\vec{e}_{s,i}, \quad (3.5)$$

with

$$\theta = \int_{s_i}^{s_f} \frac{ds}{\rho(s)} = \int_{s_i}^{s_f} h(s)ds. \quad (3.6)$$

Here, $\rho(s)$ denotes the reference orbit's bending radius, while $h(s)$ denotes the bending radius's inverse. The change of the basis vectors $(\vec{e}_x, \vec{e}_y, \vec{e}_s)$ is defined as follows:

$$\frac{d}{ds}\vec{e}_x = h(s)\vec{e}_s, \quad (3.7)$$

$$\frac{d}{ds}\vec{e}_y = 0, \quad (3.8)$$

$$\frac{d}{ds}\vec{e}_s = -h(s)\vec{e}_x. \quad (3.9)$$

To characterise the trajectory of a particle, $\vec{r}(s)$ in a beam, it is sufficient to know its position relative to the reference particle trajectory, $\vec{r}_0(s)$.

3.2 Beam Dynamics

This section will cover the dynamics of the beam, transverse motion, and longitudinal motion of particles inside the storage ring. Coordinate system used in storage ring is also discussed.

3.2.1 Transverse Motion

Consider the Cartesian coordinate system $(\vec{e}_x, \vec{e}_y, \vec{e}_s)$ for a particle travelling along the s-direction with a velocity of $v = (0, 0, v_s)$ and in the presence of a magnetic field composed entirely of transverse components, $B = (B_x, B_y, 0)$. As a result, particles in the horizontal plane will encounter Lorentz force $F_x = -qv_s B_y$ and centrifugal force $F_r = mv_s^2/R$. Here, m denotes the particle's mass and R denotes the trajectory's radius of curvature. These forces are balanced so that $F_x + F_r = 0$. The momentum of a particle is equal to $p = mv_s$. We then have an equation for the radius of curvature:

$$\frac{1}{R(x, y, s)} = \frac{q}{p} B_y(x, y, s). \quad (3.10)$$

The field expansion may be used to express the magnetic fields of a storage ring:

$$\begin{aligned}
\frac{q}{p}B_y(x) &= \frac{q}{p}B_{y0} + \frac{q}{p}\frac{dB_y}{dx}x + \frac{1}{2!}\frac{q}{p}\frac{d^2B_y}{dx^2}x^2 + \frac{1}{3!}\frac{q}{p}\frac{d^3B_y}{dx^3}x^3 + \mathcal{O}(x^4)\dots\dots \\
&= \underbrace{\frac{1}{\rho}}_{\text{Dipole}} + \underbrace{kx}_{\text{Quadrupole}} + \underbrace{\frac{1}{2!}m_{st}x^2}_{\text{Sextupole}} + \underbrace{\frac{1}{3!}ox^3}_{\text{Octupole}} + \mathcal{O}(x^4)\dots\dots
\end{aligned} \tag{3.11}$$

where k , m_{st} , and o indicate the magnet strength of quadrupoles, sextupoles, and octupoles, respectively. If k is negative, the quadrupole is focusing, and it is defocusing if k is positive.

Equation Of Motion In A Co-Moving Coordinate System

The equations of motion for a particle passing through a storage ring's magnetic structure will be introduced in this section. The general trajectory of a particle in relation to the reference orbit is described as [39]:

$$\vec{r}(s) = \vec{r}_0(s) + x(s)\vec{e}_x(s) + y(s)\vec{e}_y(s). \tag{3.12}$$

The time derivatives of $\vec{r}(s)$ are required for the formulation of the equations of motion using equations from 3.7 to 3.9:

$$\dot{\vec{r}}(s) = \dot{x}\vec{e}_x + \dot{y}\vec{e}_y + \left(1 + \frac{x}{\rho}\right)\dot{s}\vec{e}_s, \tag{3.13}$$

$$\ddot{\vec{r}}(s) = \left[\ddot{x} - \left(1 + \frac{x}{\rho}\right)\frac{\dot{s}^2}{\rho}\right]\vec{e}_x + \ddot{y}\vec{e}_y + \left[\frac{2}{\rho}\dot{x}\dot{s} + \left(1 + \frac{x}{\rho}\right)\ddot{s}\right]\vec{e}_s. \tag{3.14}$$

The position s on the passage through the storage ring is determined at every moment in time and may therefore be utilized as an independent variable. As a result, time derivatives can be converted into derivatives with respect to s , resulting in:

$$\dot{x} = \frac{dx}{ds}\frac{ds}{dt} = x'\dot{s}, \tag{3.15}$$

$$\ddot{x} = \dot{x}'\dot{s} + x'\ddot{s} = x''\dot{s}^2 + x'\ddot{s}. \quad (3.16)$$

Using the above mentioned relations 3.13 and 3.14, and similarly for y' and y'' .

$$\dot{\vec{r}}(s) = x'\dot{s}\vec{e}_x + y'\dot{s}\vec{e}_x + y'\dot{s}\vec{e}_y + \left(1 + \frac{x}{\rho}\right)\dot{s}\vec{e}_s, \quad (3.17)$$

$$\begin{aligned} \ddot{\vec{r}}(s) = \left[x''\dot{s}^2 + x'\ddot{s} - \left(1 + \frac{x}{\rho}\right)\frac{\dot{s}^2}{\rho} \right] \vec{e}_x + (y''\dot{s}^2 + y'\ddot{s})\vec{e}_y + \\ \left[\frac{2}{\rho}x'\dot{s}^2 + \left(1 + \frac{x}{\rho}\right)\ddot{s} \right] \vec{e}_s. \end{aligned} \quad (3.18)$$

Lorentz force equation 3.2 describe particle motion in electromagnetic fields. With a pure magnetic storage ring (substituting $\dot{p} = m\ddot{\vec{r}}(s)$ and also $v = \dot{r}(s)$ in equation 3.2), equation reduces to:

$$\ddot{\vec{r}}(s) = \frac{q(\dot{\vec{r}}(s) \times \vec{B})}{m}. \quad (3.19)$$

Now, the equations of motion for a variety of conditions are:

Case 1:

Assuming that only the transverse components of the magnetic field are non-zero, $B = (B_x, B_y, 0)$. This assumption is often satisfied to a large degree in particle storage ring. Now, equation 3.19 depicts:

$$\ddot{\vec{r}}(s) = \frac{q}{m} \begin{pmatrix} -\left(1 + \frac{x}{\rho}\right)\dot{s}B_y \\ \left(1 + \frac{x}{\rho}\right)\dot{s}B_x \\ x'\dot{s}B_y - y'\dot{s}B_x \end{pmatrix} \quad (3.20)$$

Co-moving coordinate system means that the reference particle's coordinate system is moving at the velocity \dot{s} , while the charged particle under observation is traveling at the velocity v . This velocity does not have to be equal to the reference particle's velocity. It may be dependent on the charged

particle's position relative to the reference particle. As seen in figure 3.2, if the charged particle is in an inner orbit, it has a lower velocity, and if it is in an outer orbit, it has a greater velocity compared to the reference particle.

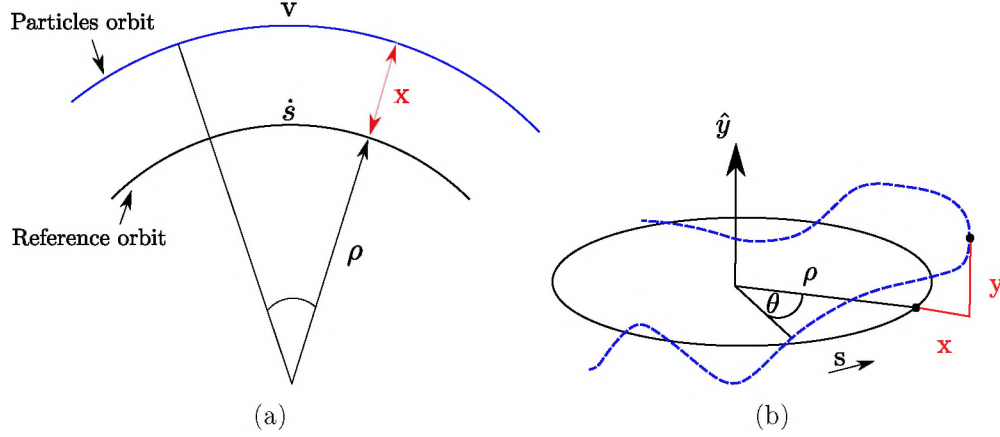


Figure 3.2: Figure (a) The reference particle's velocity is not the same as the random particle's velocity in the beam. If the charged particle is in an inner orbit, it has a lower velocity, and if it is in an outer orbit, it has a greater velocity compared to the reference particle. Figure (b) With respect to the ideal or reference trajectory, this is the trajectory for the random particle in the transverse coordinates of x and y .

Case 2:

The relative change in longitudinal velocity for relativistic particles is negligible in magnetic fields and it can be ignored. The vertical components of equations 3.18 and 3.20 are compared to get the equations of motion.

for horizontal component:

$$x''\dot{s}^2 + x'\ddot{s} - \left(1 + \frac{x}{\rho}\right) \frac{\dot{s}^2}{\rho} = -\frac{q}{m} \left(1 + \frac{x}{\rho}\right) \dot{s}B_y, \quad (3.21)$$

for vertical component:

$$y''\dot{s}^2 + y'\ddot{s} = \frac{q}{m} \left(1 + \frac{x}{\rho}\right) \dot{s}B_x. \quad (3.22)$$

Case 3:

To simplify the equation, suppose the particles' velocity varies very slowly as they pass through the magnetic field, so $\ddot{s} \approx 0$. As seen in figure 3.2 $v \neq \dot{s}$. The velocity of an arbitrary particle in a beam may be described as follows:

$$v = \dot{s} \frac{\rho + x}{\rho} = \dot{s} \left(1 + \frac{x}{\rho} \right). \quad (3.23)$$

Case 4:

Further simplifying the equations 3.21 and 3.22, using $p = mv$ and $\ddot{s} \approx 0$, we get the equation of motion components as:

$$\text{for horizontal component: } x'' - \left(1 + \frac{x}{\rho} \right) \frac{1}{\rho} = -\frac{q}{p} \left(1 + \frac{x}{\rho} \right)^2 B_y, \quad (3.24)$$

$$\text{for vertical component: } y'' = \frac{q}{p} \left(1 + \frac{x}{\rho} \right)^2 B_x. \quad (3.25)$$

Momentum of the particle :

Assuming the particle's momentum is $p = p_0 + \Delta p$, and the momentum deviation is denoted as Δp . The momentum deviation of Δp is quite small when compared to the nominal momentum of p_0 . These variances Δp are often smaller than 1%, at which point the inverse of the momentum may be approximated using a linear approximation. Therefore,

$$\frac{1}{p} = \frac{1}{p_0} \left(1 - \frac{\Delta p}{p_0} \right) + \mathcal{O}(\Delta p^2). \quad (3.26)$$

Case 5:

Assuming the particles are bent in the horizontal plane according to equation 3.11, the magnetic fields in each direction may be stated as follows:

$$\frac{q}{p_0} B_y = \frac{1}{\rho} - kx, \quad (3.27)$$

$$\frac{q}{p_0} B_x = -ky. \quad (3.28)$$

Now, substituting equations 3.24 and 3.25 with 3.27 and 3.28 we get:

for horizontal component:

$$x'' - \left(1 + \frac{x}{\rho}\right) \frac{1}{\rho} = - \left(1 + \frac{x}{\rho}\right)^2 \left(\frac{1}{\rho} - kx\right) \left(1 - \frac{\Delta p}{p_0}\right), \quad (3.29)$$

for vertical component:

$$y'' = - \left(1 + \frac{x}{\rho}\right)^2 ky \left(1 - \frac{\Delta p}{p_0}\right). \quad (3.30)$$

Case 6:

Furthermore, assuming the equation of motion for a particle moving through a magnetic structure in a pure magnetic ring with dipoles and quadrupoles only present with their vertical magnetic fields. Also, the bending radius is substantially larger than the transverse deviations from the reference orbit x and y , ($x \ll \rho$), ($y \ll \rho$), ($(\Delta p/p) \ll 1$), therefore neglecting the terms which contains x, y , and $\Delta p/p_0$ we get:

for horizontal component:

$$\boxed{x''(s) + \left(\frac{1}{\rho^2(s)} - k(s)\right) x(s) = \frac{1}{\rho(s)} \frac{\Delta p}{p_0}}, \quad (3.31)$$

for vertical component:

$$\boxed{y''(s) + k(s)y(s) = 0}. \quad (3.32)$$

These equations are the basis of calculations in linear beam optics.

3.2.2 Beta Function And Betatron Oscillation

The equation of motion 3.31 and 3.32 can be rewritten with assumption that if dispersive effects are neglected, $\Delta p/p = 0$ and $1/\rho = 0$, equation of motion becomes:

$$x''(s) - k(s)x(s) = 0, \quad (3.33)$$

$$y''(s) - k(s)y(s) = 0. \quad (3.34)$$

Equation 3.33 and 3.34 are also known as **Hill's differential equation of motion**. A transverse oscillation across the reference orbit is known as a **betatron oscillation**, and is described by the trajectory function $x(s)$. The Betatron oscillation's amplitude ($\sqrt{\varepsilon}\sqrt{\beta(s)}$) and phase ($\Psi(s)$) are dependent upon the position s along the orbit. As both equations have the same structure and can be solved using the same approach, it is sufficient to investigate only the horizontal solution. The vertical solution is then obtained in a similar manner. The solution to Hill's differential equation above is:

$$x(s) = A \cos[\Psi(s) + \phi], \quad (3.35)$$

where A and ϕ are the integration constants that define an individual particle's trajectory.

Replacing A by $\sqrt{\varepsilon}$ (where ε is emittance, it will be discussed in details in section 3.2.3) and $\beta(s) = u^2(s)$ in equation 3.33 we will get solution to trajectory equation:

$$x(s) = \sqrt{\varepsilon}\sqrt{\beta(s)}\cos[\Psi(s) + \phi], \quad (3.36)$$

$$\text{with } \Psi(s) = \int_0^s \frac{ds}{\beta(s)}, \quad (3.37)$$

where, $\beta(s)$ is Beta function and also commonly known as **amplitude function**, Beta function describes the angle and position of transverse oscillation at a given position s for a particle in a beam. The first derivative of the trajectory function $x(s)$,

$$x'(s) = -\frac{\sqrt{\varepsilon}}{\sqrt{\beta(s)}}[\alpha(s)\cos(\Psi(s) + \phi) + \sin(\Psi(s) + \phi)], \quad (3.38)$$

where, Alpha function is given as:

$$\alpha(s) = -\frac{\beta'(s)}{2}. \quad (3.39)$$

Functions $\beta(s)$, $\alpha(s)$ along with dispersion $D(s)$ and its derivative $D'(s)$ describe the linear beam optics in a plane.

Envelope of the beam: The particles undergo betatron oscillations with a position-dependent amplitude within the magnet structure, which has a net focusing effect. This position-dependent amplitude is also known as the envelope [39] (represented in figure 3.3) and it is stated as,

$$E(s) = \sqrt{\varepsilon\beta(s)}. \quad (3.40)$$

Particles move in a transverse direction around the orbit within the envelope $E(s)$. Since all particle trajectories fall inside this envelope, it determines the beam's transverse size, as shown in figure 3.3. The beam's envelope $E(s)$ is defined by the particle with the highest emittance because the amplitude of the betatron oscillations is provided by the relation 3.40.

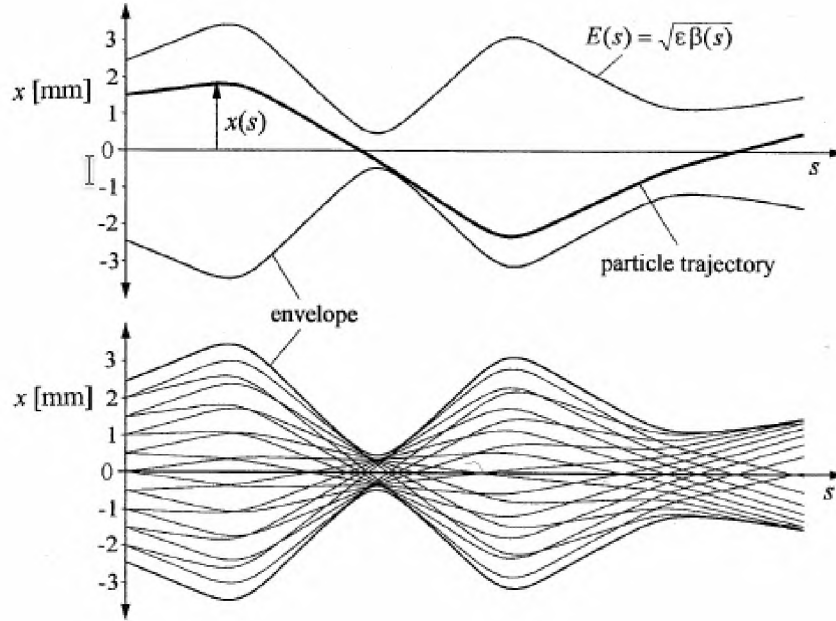


Figure 3.3: Particle trajectories $x(s)$ within the beam's envelope $E(s)$. The upper figure depicts a single trajectory, whereas the lower figure depicts a group of various separate trajectories. All of the separate trajectories together form the beam. The figure is taken from [39].

3.2.3 Beam Emittance And Betatron Tune

To get an equation characterising particle motion in the $x - x'$ phase space plane, we must first remove the phase-dependent Ψ terms from equation 3.36. By rearranging 3.36 we'll obtain:

$$\cos(\Psi(s) + \phi) = \frac{x}{\sqrt{\varepsilon}\sqrt{\beta(s)}}. \quad (3.41)$$

Using this substitution and rearrangement in equation 3.38 leads to:

$$\sin(\Psi(s) + \phi) = \frac{\sqrt{\beta(s)}x'}{\sqrt{\varepsilon}} + \frac{\alpha(s)x}{\sqrt{\varepsilon}\sqrt{\beta(s)}}. \quad (3.42)$$

Using the relation $\sin^2 \Theta + \cos^2 \Theta = 1$ we get,

$$\frac{x^2}{\beta(s)} + \left(\frac{\alpha(s)x}{\sqrt{\beta(s)}} + \sqrt{\beta(s)}x' \right)^2 = \varepsilon. \quad (3.43)$$

New variable called **gamma function** is defined as:

$$\boxed{\gamma(s) = \frac{1 + \alpha^2(s)}{\beta(s)}}. \quad (3.44)$$

Substituting this variable in equation 3.43, we will get **equation of phase ellipse** in the $x - x'$ plane:

$$\boxed{\gamma(s)x^2(s) + 2\alpha(s)x(s)x'(s) + \beta(s)x'^2(s) = \varepsilon}. \quad (3.45)$$

Beam Emittance: Beam emittance (ε) or Courant-Snyder invariant is defined as the area of the phase ellipse (F) within a factor of π , that is $\varepsilon = F\pi$ [37]. Figure 3.4 depicts phase space ellipse with a given emittance ε at a specified position s .

According to Liouville's theorem [40], if the particles satisfy the canonical equations of motion, every element in a volume of phase space is constant with respect to time, which means the area of the phase ellipse is constant and also the beam emittance is invariant of particle motion. The phase space of a linear transverse particle motion is characterised by an ellipse with constant area that depends on the particle's Courant-Snyder invariant. The ellipse rotates in the coordinate system along with the magnetic structure of the ring, but its size and shape remain constant.

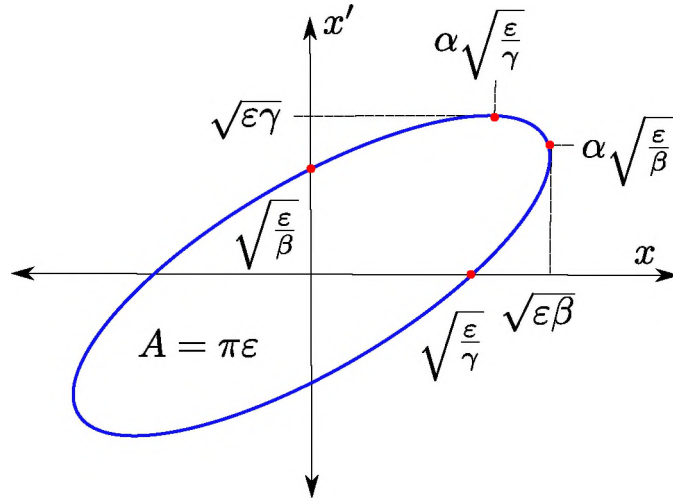


Figure 3.4: Phase space ellipse in the $x - x'$ plane of particle motion. The phase space of a linear transverse particle motion is characterised by an ellipse with constant area that depends on the particle's Courant-Snyder invariant. The ellipse rotates in the coordinate system along with the magnetic structure of the ring, but its size and shape remain constant.

Betatron tune is the number of betatron oscillations per turn, which is transverse oscillation's total phase advance per rotation and is generally defined in units of 2π . It is denoted by Q [41],

$$Q = \frac{1}{2\pi} \int_s^{s+C} \Psi ds = \frac{1}{2\pi} \int_s^{s+C} \frac{ds}{\beta(s)}. \quad (3.46)$$

3.2.4 Longitudinal Motion

So far, only the transverse motion of particles in the storage ring has been considered. Now longitudinal motion will be discussed. The accelerating cavity, or radiofrequency (RF) cavity, generates a longitudinally oscillating electric field which accelerates the particles or bunch of particles. It has the greatest impact on the longitudinal motion. When the reference particle or synchronous particle enters the RF cavity, it has precisely the right momentum as well as the right transit time, so that it gets the exact amount of energy it needs to move in a closed orbit, crossing through the centre of all magnets. However, a particle beam consists of dispersed particles with different momentums and transit times across the RF cavity, which leads to a phase stability issue.

Phase Stability

A synchronous particle (particle which always passes through the RF cavity when the field is at the same phase) with electric charge q passes through the RF cavity, during each revolution of the ring, its energy gain per turn is equal to [42]:

$$\Delta E_s = qV_0 \sin \phi_s, \quad (3.47)$$

where V_0 is the accelerating voltage amplitude and ϕ_s is the RF phase. Reference (synchronised) particles have the same phase ϕ_s as that of the RF cavity. The synchronous particle passes through the centre of magnets in the ring with the same phase, ϕ_s , and gains the same energy with each turn.

Beam particles are likely to deviate from their reference trajectory. Considering a particle with a different momentum p , than the synchronous particle p_0 . If L is the circumference of the ring and v is the velocity of the particle under consideration, the time required to complete one revolution is $\tau = L/v$. The fractional change in τ due to variations in L and v is given as:

$$\frac{\Delta \tau}{\tau} = \frac{\Delta L}{L} - \frac{\Delta v}{v_0}. \quad (3.48)$$

Here, v_0 is the velocity of the reference particle. Equation 3.48 demonstrates how a particle travelling faster than the reference particle takes less time

to complete one revolution. However, if the path length is longer, the time required to reach the RF cavity will be increased. In terms of the fractional momentum deviation, the fractional change in velocity may be written as follows [43]:

$$\frac{\Delta v}{v_0} = \frac{1}{\gamma^2} \left(\frac{\Delta p}{p_0} \right). \quad (3.49)$$

Magnetic rigidity is $B\rho = p/q$ in circular storage rings. Since it is related to momentum, one may anticipate the orbit circumference to be greater for a particle with a momentum somewhat greater than the ideal particle's. The momentum compaction factor, α_c , determines the orbital length fluctuation with momentum, and it is referred to as,

$$\frac{\Delta L}{L} = \alpha_c \frac{\Delta p}{p_0}. \quad (3.50)$$

Substituting equation 3.50 and 3.49 in equation 3.48, we will get,

$$\frac{\Delta \tau}{\tau} = \left(\alpha_c - \frac{1}{\gamma^2} \right) \frac{\Delta p}{p_0} = \eta \frac{\Delta p}{p_0}. \quad (3.51)$$

Here, η is the coefficient called **slip factor**:

$$\eta = \left(\alpha_c - \frac{1}{\gamma^2} \right). \quad (3.52)$$

Transition energy is the energy for which the slip factor is equal to zero for a specific γ_{tr} , which means that the revolution frequency of particles with a small momentum deviation does not vary. γ_{tr} is denoted as,

$$\gamma_{tr} = \frac{1}{\sqrt{\alpha_c}}. \quad (3.53)$$

Equation 3.51 may also be expressed in terms of revolution frequency,

$$\frac{\Delta f}{f_0} = -\frac{\Delta \tau}{\tau} = -\eta \frac{\Delta p}{p_0}. \quad (3.54)$$

Here, f_0 is the revolution frequency of reference particle. From figure 3.5 and equation 3.54, we can understand the phase stability principle.

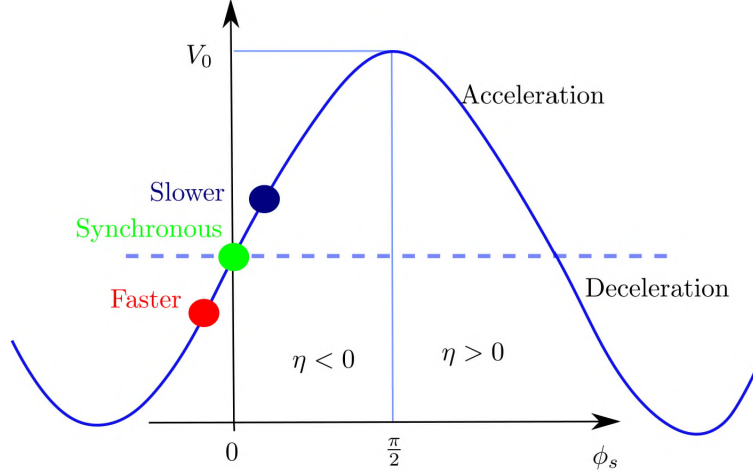


Figure 3.5: RF wave sketch, reference particle in green, other particle with higher energy in red ($\frac{\Delta p}{p_0} > 0$) and lower energy particle in dark blue ($\frac{\Delta p}{p_0} < 0$). For stable synchrotron motion, $\phi_s = 0$ for $\eta < 0$ and $\phi_s = \pi$ for $\eta > 0$ [44].

- For a particle with momentum larger than the reference particle momentum $\frac{\Delta p}{p_0} > 0$ and energy below transition energy, $\gamma < \gamma_{tr}$, the particle will have revolution frequency higher than reference particle frequency $f > f_0$ that is, it will cross RF cavity faster than reference particle. This leads to a negative particle phase, so it acquires less energy than the reference particle and hence decelerates.

This method helps to maintain the phase stability from turn to turn by reducing both the phase change and the energy difference.

3.3 BMAD Software

The simulations in this thesis are carried out with the help of the BMAD [45] software library, which was developed for Elementary Particle Physics at Cornell University. BMAD is an object-oriented, open-source, subroutine library written in FORTRAN 95. The library includes subroutines for simulating relativistic charged particle beams and spin dynamics. It enables single-and multi-particle tracking using a variety of tracking techniques. In terms of spin tracking, BMAD enables the incorporation of a non-vanishing

EDM. Additionally, BMAD allows for the combination of superimposition of elements. Various changes are introduced in BMAD which will be discussed in details in upcoming sections.

3.4 Spin Dynamics

A detailed investigation of the spin dynamics in storage rings is required for the design of a storage ring based EDM experiment. But the first study of spin behaviour is very important, and then how the beam motion is coupled to spin motion. In this thesis, beam and spin behaviour studies have a major role, so basics are discussed first, such as the spin of particles such as deuteron and proton, and then spin motion in an electromagnetic field. Major section regarding spin dynamics is taken from following [46–48].

3.4.1 Polarisation Formalism

The term "polarisation" refers to an ensemble of particles' average spin orientation. A particle's single spin may be represented by an operator \hat{S} in which the spin angular momentum is projected along the specified quantization axis as $S_z = m_s \hbar$. m_s is a spin quantum number that may take $(2s + 1)$ values and ranges from $-s$ to s , where s is the particle's spin number and z -axis is used as the spin quantization axis. Spin $\frac{1}{2}$ and spin 1 will be discussed in detail in the following sections.

3.4.2 Spin $\frac{1}{2}$ Particles

Proton has spin $\frac{1}{2}$ and spin quantum number m_s can only be present in two states, $m_s = \pm\frac{1}{2}$. A single spin $\frac{1}{2}$ particle's state may be described as a normalised Pauli spinor [48] with two components:

$$\Psi = \begin{pmatrix} x \\ y \end{pmatrix}, \quad (3.55)$$

with condition $|x|^2 + |y|^2 = 1$. In the equation, 3.55 two spinor components are $m_s = \pm\frac{1}{2}$. Cartesian coordinate system $(\vec{e}_1, \vec{e}_2, \vec{e}_3)$ is used for following discussion, where \vec{e}_3 is spin quantization axis. Using Pauli spin operator, in the case of spin $\frac{1}{2}$ particles, the operator is defined as:

$$\hat{S} = \frac{\hbar}{2} \vec{\sigma}. \quad (3.56)$$

Where,

$$\sigma_1 = \begin{pmatrix} 0 & 1 \\ 1 & 0 \end{pmatrix}, \sigma_2 = \begin{pmatrix} 0 & -i \\ i & 0 \end{pmatrix}, \sigma_3 = \begin{pmatrix} 1 & 0 \\ 0 & -1 \end{pmatrix}. \quad (3.57)$$

This set of matrices can be extended by the fourth unit matrix.

$$\sigma_0 = \begin{pmatrix} 1 & 0 \\ 0 & 1 \end{pmatrix}. \quad (3.58)$$

These 4 matrices form a complete basis of 2×2 Hermitian matrices. An observable is described as the associated operator \hat{A} 's expectation value, which is defined as:

$$\langle A \rangle = \langle \Psi | \hat{A} | \Psi \rangle = \Psi^\dagger \hat{A} \Psi. \quad (3.59)$$

Now defining the density matrix:

$$\rho = |\Psi\rangle\langle\Psi| = \begin{pmatrix} |x|^2 & xy^* \\ x^*y & |y|^2 \end{pmatrix}. \quad (3.60)$$

The expectation value using the trace of the product of a density matrix and the operator is written as:

$$\langle \hat{A} \rangle = \text{Tr} \rho \hat{A} \quad (3.61)$$

The spin vector \vec{S} represents the spin operator's expected value.

$$\vec{S} = \langle \hat{S} \rangle = \frac{\hbar}{2} \text{Tr} \rho \vec{\sigma} = \frac{\hbar}{2} \begin{pmatrix} 2\text{Re}(xy^*) \\ 2\text{Im}(xy^*) \\ |x|^2 + |y|^2 = 1 \end{pmatrix}. \quad (3.62)$$

When the single particle is replaced by an ensemble of N particles, the quantity of interest becomes the expectation value of the ensemble's spin observables. In this scenario, the density matrix must be expanded to include the following:

$$\rho = \frac{1}{N} \begin{pmatrix} \sum_{i=1}^N |x^{(i)}|^2 & \sum_{i=1}^N x^{(i)} y^{(i)*} \\ \sum_{i=1}^N x^{(i)*} y^{(i)} & \sum_{i=1}^N |y^{(i)}|^2 \end{pmatrix}. \quad (3.63)$$

In terms of Pauli spin operators:

$$\rho = \frac{1}{2} (\sigma_0 + \vec{P} \vec{\sigma}) \quad (3.64)$$

\vec{P} signifies the polarisation vector, which is the average of all the spin operators' expectation values in the ensemble:

$$\vec{P} = \frac{1}{N} \sum_{i=1}^N \vec{S}_i. \quad (3.65)$$

Let us consider that the beam is composed of $N^{m_s=\frac{1}{2}}$ and $N^{m_s=-\frac{1}{2}}$ particles in quantum states, such as $m_s = +\frac{1}{2}$ and $m_s = -\frac{1}{2}$ respectively. Vector polarisation P_v is defined as [46]:

$$P_v = \frac{N^{m_s=\frac{1}{2}} - N^{m_s=-\frac{1}{2}}}{N^{m_s=\frac{1}{2}} + N^{m_s=-\frac{1}{2}}}. \quad (3.66)$$

From the vector polarisation, we can say that the beam is fully polarised if $P_v = \pm 1$ and unpolarised if $P_v = 0$.

3.4.3 Spin 1 Particles

Spin 1 particles (like deuteron) may exist in one of three states: $m_s = 1, m_s = 0$, or $m_s = -1$. As a result, it is represented by a three-dimensional spinor [48]:

$$\Psi = \begin{pmatrix} a_1 \\ a_2 \\ a_3 \end{pmatrix}. \quad (3.67)$$

Spin operators are defined as follows:

$$\hat{S}_1 = \frac{\hbar}{\sqrt{2}} \begin{pmatrix} 0 & 1 & 0 \\ 1 & 0 & 1 \\ 0 & 1 & 0 \end{pmatrix}, \quad \hat{S}_2 = \frac{\hbar}{\sqrt{2}} \begin{pmatrix} 0 & -i & 0 \\ i & 0 & -i \\ 0 & i & 0 \end{pmatrix}, \quad \hat{S}_3 = \hbar \begin{pmatrix} 1 & 0 & 0 \\ 0 & 0 & 0 \\ 0 & 0 & -1 \end{pmatrix}. \quad (3.68)$$

Nine independent hermitian matrices are required to characterise a spin 1 system. And they are the basis for 3×3 hermitian operators. In the Cartesian coordinate system, using the identity matrix (I), these operators are:

$$\hat{S}_{ij} = \frac{3}{2} \left(\hat{S}_i \hat{S}_j + \hat{S}_j \hat{S}_i \right) - 2I\delta_{ij} \quad i, j \in 1, 2, 3 \quad (3.69)$$

The density matrix of a spin 1 particle ensemble may be represented as [47]:

$$\rho = \frac{1}{3} \left[I + \frac{3}{2} \sum_{i=1}^3 P_i S_i + \frac{1}{2} \sum_{i=1}^3 \sum_{j=1}^3 P_{ij} S_{ij} \right], \quad \text{with } P_{ij} = P_{ji} \quad (3.70)$$

where, P_i and P_{ij} are the polarisation states of spin-1 particle.

Considering the three states $m_s = -1, 0, 1$ for $N^{m_s=-1}, N^{m_s=0}, N^{m_s=1}$ particles of beam, along the quantization axis the vector polarisation P_V and tensor polarisation P_T is given by[46]:

$$P_V = \frac{N^{m_s=1} - N^{m_s=-1}}{N^{m_s=1} + N^{m_s=0} + N^{m_s=-1}}, \quad (3.71)$$

$$P_T = \frac{N^{m_s=1} + N^{m_s=-1} - 2N^{m_s=0}}{N^{m_s=1} + N^{m_s=0} + N^{m_s=-1}}. \quad (3.72)$$

3.5 Spin Motion In Storage Ring

This section will discuss how spin behaves in electric and magnetic fields. Following that, the spin equation of motion in electromagnetic fields in the rest frame of reference will be studied. Finally, several EDM experiment approaches are discussed.

3.5.1 Spin Evolution In Electric And Magnetic Field

Equation 2.9 gives the Hamiltonian, which describes the particle's EDM and MDM interactions with electromagnetic fields in its rest frame. The non-relativistic spin equation of motion for the spin vector \vec{S} in electric and magnetic fields is as follows:

$$\frac{d\vec{S}}{dt} = \vec{\Omega} \times \vec{S} = \vec{\mu} \times \vec{B} + \vec{d} \times \vec{E}. \quad (3.73)$$

where $\vec{\mu}$ is the magnetic dipole moment (MDM), \vec{d} is the electric dipole moment (EDM), and $\vec{\Omega}$ is the angular frequency that represents the rate of change of the polarisation due to the magnetic (MDM) and electric (EDM) dipole interactions. Equations 2.7 and 2.8, relate electric dipole moment \vec{d} and magnetic dipole moment $\vec{\mu}$ with spin, respectively. According to the equation 3.73, there is a spin precession in the plane perpendicular to $\vec{\Omega}$ with an angular frequency of $|\vec{\Omega}|$. Experimental measurements are used to determine the MDM of different particles. Nuclear magnetons are commonly used to describe MDM values for hadronic systems [49] :

$$\mu_N = 3.1524512550(15) \cdot 10^{-8} \text{ eV/T}. \quad (3.74)$$

An anomalous magnetic moment or gyromagnetic anomaly is denoted by G as:

$$G = \frac{g - 2}{2}, \quad (3.75)$$

where, g is the g -factor. The values of the proton and deuteron gyromagnetic anomaly G are 1.792847 (proton) and -0.142987 (deuteron).

3.5.2 Spin Precession – TBMT Equation

In the storage ring physics setup, the laboratory reference frame is more often used to describe the fields than the particle rest frame as used in equation 3.73. As a result, the equation must be recalculated in terms of the laboratory reference frame. The spin equation of motion may be represented

in a laboratory system using magnetic and electric fields, while the spin is still specified in the particle's rest frame of reference. The resulting equation is the so-called Thomas-Bargmann-Michel-Telegdi (TBMT) equation, which can be extended in order to include the EDM effect and read as follows [50–52]:

$$\frac{d\vec{S}}{dt} = \vec{\Omega} \times \vec{S} = (\vec{\Omega}_{MDM} + \vec{\Omega}_{EDM}) \times \vec{S}, \quad (3.76)$$

$$\vec{\Omega}_{MDM} = -\frac{q}{m} \left[\left(G + \frac{1}{\gamma} \right) \vec{B} - \frac{\gamma G}{\gamma + 1} \vec{\beta} (\vec{\beta} \cdot \vec{B}) - \left(G + \frac{1}{\gamma + 1} \right) \vec{\beta} \times \frac{\vec{E}}{c} \right], \quad (3.77)$$

$$\vec{\Omega}_{EDM} = -\frac{q}{mc} \frac{\eta_{EDM}}{2} \left[\vec{E} - \frac{\gamma}{\gamma + 1} \vec{\beta} (\vec{\beta} \cdot \vec{E}) + c \vec{\beta} \times \vec{B} \right]. \quad (3.78)$$

Here, $\vec{\Omega}_{EDM}$ and $\vec{\Omega}_{MDM}$ are the spin precession frequencies due to interaction of EDM and MDM with an electromagnetic field, and $\eta_{EDM} = 2\vec{d}mc/q\hbar\vec{S}$ is a dimensionless EDM parameter. This is still the fundamental equation of spin precession since the interaction of field gradients with the electric quadrupole and magnetic dipole moment is not included, but this will be described in the section 4.2.2, which is the primary basis of my thesis.

Additionally, one may also represent the rotation caused by the MDM in terms of parallel and perpendicular field components relative to the momentum vector:

$$\vec{\Omega}_{MDM} = \vec{\Omega}_{B\perp} + \vec{\Omega}_{B\parallel} + \vec{\Omega}_{E\perp} + \vec{\Omega}_{E\parallel}, \quad (3.79)$$

$$= -\frac{q}{\gamma m} \left[(1 + G\gamma) \vec{B}_{\perp} + (1 + G) \vec{B}_{\parallel} - \left(G\gamma + \frac{\gamma}{\gamma + 1} \right) \vec{\beta} \times \frac{\vec{E}_{\perp}}{c} \right], \quad (3.80)$$

where, $\vec{\Omega}_{E\parallel} = 0$ since $\vec{\beta} \times \vec{E}_{\parallel} = 0$. The momentum also precesses with the angular frequency $\vec{\Omega}_{cyc}$ under the influence of electromagnetic fields, which is given as:

$$\vec{\Omega}_{cyc} = -\frac{q}{\gamma m} \left(\vec{B}_{\perp} - \frac{\vec{\beta} \times \vec{E}_{\perp}}{\beta^2 c} \right). \quad (3.81)$$

The corresponding equation of motion is given as:

$$\frac{d\vec{p}}{dt} = \vec{\Omega}_{cyc} \times \vec{p}. \quad (3.82)$$

The crossing point of frequencies at which the cyclotron frequency and spin precession frequency due to MDM are comparable can be easily estimated using:

$$\Delta\vec{\Omega}_{cyc,S} = \vec{\Omega}_{MDM} - \vec{\Omega}_{cyc}. \quad (3.83)$$

Substituting the equations 3.80 and 3.81 in equation 3.83 we get the following equation:

$$\Delta\vec{\Omega}_{cyc,S} = -\frac{q}{\gamma m} \left[G\gamma\vec{B}_\perp + (1+G)\vec{B}_\parallel - \left(G\gamma - \frac{\gamma}{\gamma^2-1} \right) \vec{\beta} \times \frac{\vec{E}_\perp}{c} \right]. \quad (3.84)$$

Now, assuming that the storage ring contains only vertical magnetic fields and ignoring EDM, the spin precession may be computed as:

$$\frac{d\vec{S}}{dt} = -\frac{q}{\gamma m} (1+G\gamma)\vec{B}_y \times \vec{S}. \quad (3.85)$$

In this scenario, unlike many other spin orientations, an initial spin parallel or anti-parallel to the vertical axis does not precess and remains stable throughout time. The axis in which the orientation of spin is preserved is known as **spin closed orbit or invariant spin axis** \vec{n}_c . The number of spin oscillations per revolution is known as spin tune (ν_S), and it is given as:

$$\nu_S = \frac{-\frac{q}{\gamma m}(1+G\gamma)}{-\frac{q}{\gamma m}} - 1 = \gamma G. \quad (3.86)$$

Here, one revolution was subtracted to account for the rotation of the co-moving coordinate system.

3.6 Methods Proposed For EDM Measurement In Storage Ring

Various methods for measuring EDM will be discussed in this section. First, the basic concept of EDM measurement will be discussed, followed by methods namely the Frozen Spin method, the Quasi Frozen Spin method, and the RF Wien filter method.

3.6.1 Basic Idea Of EDM Measurement

The primary objective of such a measurement is to monitor the build-up of vertical polarisation caused by an EDM using a horizontally polarised beam initially. The spin precession of a charged particle in a rest frame due to EDM interaction with an electric field E^* and MDM interaction with a magnetic field B^* is given as [24]:

$$\frac{d\vec{S}}{dt} = \vec{\mu} \times \vec{B}^* + \vec{d} \times \vec{E}^*. \quad (3.87)$$

Equation 3.76, 3.77, 3.78 can be simplified and used to explain spin motion when the magnetic and electric fields are assumed to be perpendicular to the momentum of the particle. After simplification, the spin precession equation is [51, 52]:

$$\frac{d\vec{S}}{dt} = \vec{S} \times \vec{\Omega} = \vec{S} \times (\vec{\Omega}_{MDM} + \vec{\Omega}_{EDM}), \quad (3.88)$$

$$\vec{\Omega}_{MDM} = -\frac{q}{m} \left[G\vec{B} - \left(G - \frac{1}{\gamma^2 - 1} \right) \vec{\beta} \times \frac{\vec{E}}{c} \right], \quad (3.89)$$

$$\vec{\Omega}_{EDM} = -\frac{q}{mc} \frac{\eta_{EDM}}{2} \left[\vec{E} + c\vec{\beta} \times \vec{B} \right]. \quad (3.90)$$

Spin precession in an ideal storage ring takes place horizontally, and the spin-closed orbit \vec{n}_c is aligned vertically with the vanishing EDM ($\vec{\Omega}_{EDM} = 0$). Since $\vec{\Omega}_{EDM} \perp \vec{\Omega}_{MDM}$, a non-vanishing EDM tilts this precession plane, as seen in figure 3.6. The tilt angle is defined as the ratio of the contributions of $\vec{\Omega}_{EDM}$ and $\vec{\Omega}_{MDM}$.

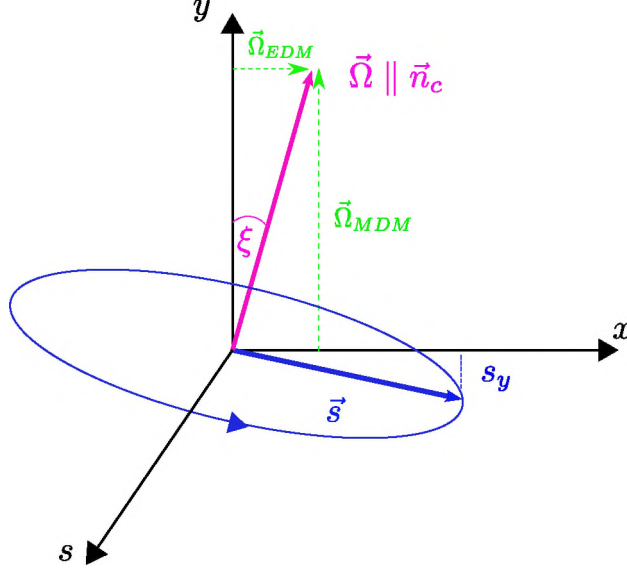


Figure 3.6: The tilt ξ of the invariant spin axis \vec{n}_c [53], due to spin interaction in the guiding fields of a magnetic storage ring. Contribution of MDM and EDM are perpendicular to each other. The vertical spin component oscillates as a result of the tilt ξ .

$$\tan \xi = \frac{\eta_{EDM}\beta}{2G}. \quad (3.91)$$

EDM measurements with use of storage ring are feasible if the experimental configuration results in a macroscopic buildup of vertical polarisation. The above stated idea was used to measure EDM of muons [54]. The protons and deuteron' anomalous magnetic moments are two and three order of magnitude larger respectively than muons. As a consequence, the resultant tilt angle ξ would be substantially less in case of similar beam energy and EDM value. Different measurements methods have been proposed to overcome this problem and to carry out EDM measurements of protons and deuterons such as frozen spin method, quasi frozen spin method and RF Wien filter method. They will be discussed in details in upcoming sections. The main idea for measuring EDM in the storage ring is to keep the spin frozen in the momentum direction in order to eliminate the MDM contribution and maximise the EDM signal buildup, which is the frozen spin method 3.6.2.

3.6.2 Frozen Spin Method

The prerequisite for this approach is that the spin is "frozen," which implies that the particle's spin is always parallel to beam momentum vector. That means the spin precession frequency must be equal to the momentum precession frequency in order to ensure this condition. Then vertical polarisation buildup over time is directly proportional to the tilt angle ξ . And by eliminating the Ω_{MDM} , the tilt angle may be increased. However, this is feasible for protons with the "magic" momentum in a pure electric storage ring. This approach is only applicable to deuterons when a superposition of magnetic and electric bending fields is used. Now, in order to achieve the frozen spin condition, $\vec{\Omega}_{MDM} = 0$, using eq. 3.89:

$$G\vec{B} - \left(G - \frac{1}{\gamma^2 - 1}\right)\vec{\beta} \times \frac{\vec{E}}{c} = 0. \quad (3.92)$$

To satisfy this condition, different combinations of electric and magnetic fields must be utilised, depending on the particle and its anomalous magnetic moment G . When a particle's spin is initially aligned with the momentum direction, the EDM's interaction with the storage ring's guiding fields results in the gradual vertical polarisation buildup, which serves as an indicator of a non-zero EDM.

Pure electric storage ring

This method can be used for those particles with $G > 0$, using only electric fields, the spin can be frozen. To satisfy this criterion, particles must possess a magic momentum:

$$p_{magic} = \gamma\beta mc = \sqrt{\gamma^2 - 1}mc = \frac{mc}{\sqrt{G}}. \quad (3.93)$$

This method is only applicable to particles with a $G > 0$; the proton has a $G = 1.79$, implying that its magical momentum is $p \approx 0.701$ GeV/c. The anomalous magnetic moment G for deuteron is negative. Thus, this method is invalid for deuteron.

Combined magnetic and electric ring:

In order to freeze particles with a negative anomalous magnetic moment a combination of radial electric and vertical magnetic fields is required. Equation of frozen spin condition 3.92 can be used to calculate the ratio between the vertical magnetic field and radial electric field strengths:

$$\frac{|\vec{B}|}{|\vec{E}|} = \left(1 - \frac{1}{G(\gamma^2 - 1)}\right) \frac{\beta}{c}. \quad (3.94)$$

Both lattice configurations presented are investigated at JEDI collaboration [53] [55]. First MDM has no contribution to spin motion if the frozen spin condition is satisfied. Second, the interaction of EDM with electromagnetic fields causes a buildup of vertical polarisation. Thirdly, the EDM may be determined directly by measuring Ω_{EDM} the spin rotation frequency. Although suggestions for frozen spin storage rings have been developed, none have reached the operating level.

The spin precession frequency could be on the order of 0.1 mHz for a pure electric ring with electric fields of 10 MVm^{-1} and an EDM $\approx 10^{-24} \text{ e}\cdot\text{cm}$. Because the polarisation lifetime at a typical storage ring is up to 1000 s, the polarimeter detects this low frequency, leading in a linear rise in the vertical polarisation P_y that is proportional to the EDM, $P_y(t) = P_0 \cdot \sin(\Omega_{EDM}t) \approx P_0 \cdot \Omega_{EDM}t$.

Along with the EDM signal, systematic effects may also contribute to the development of vertical polarisation. Magnet misalignments and field imperfections such as radial magnetic fields produced by misaligned quadrupoles may significantly affect the measured signal [38, 56]. These effects may be eliminated using beams rotating in clockwise and counter-clockwise directions inside the same storage ring [57, 58].

3.6.3 Quasi Frozen Spin Method

As described in last section 3.6.2 the concept of a "frozen spin" (FS) where reference particle's spin is always oriented parallel to the momentum. Implementing the FS idea in any current storage ring would need a full upgrade.

So the QFS method [59] was proposed, in which the spin is not frozen with respect to the momentum vector but continually oscillates around it with a few degrees of amplitude.

To explain the oscillation of spin around momentum vector, let us consider separately the spin equations in an electric deflector and in a bending magnet. The MDM spin precession part of the TBMT equation in the horizontal driving electric field is determined in the laboratory coordinate system as:

$$\vec{\Omega}_G^E = -\frac{q}{m} \left[\left(G + \frac{1}{\gamma + 1} \right) \vec{\beta} \times \frac{\vec{E}}{c} \right]. \quad (3.95)$$

Also, the frequency of particle momentum precession in the laboratory coordinate system with E field is given by:

$$\vec{\Omega}_P^E = -\frac{q}{mc} \left[\frac{\vec{E} \times \vec{\beta}}{\gamma \beta^2} \right], \quad (3.96)$$

by subtracting equation 3.96 from 3.95 and normalising it by 3.95. The spin tune in the electrical deflector related to the momentum is obtained by:

$$\nu_S^E = \left(-G + \frac{1}{\gamma^2 - 1} \right) \beta^2 \gamma. \quad (3.97)$$

We may apply the same logic to the magnetic field. The frequency of MDM spin precession in the laboratory coordinate system in the bending magnet is:

$$\vec{\Omega}_G^B = \frac{q}{mc} \left(G + \frac{1}{\gamma} \right) cB, \quad (3.98)$$

and momentum precession frequency in the field B is given by:

$$\vec{\Omega}_P^B = \frac{q}{mc} \frac{cB}{\gamma}. \quad (3.99)$$

Similarly, by subtracting equation 3.99 from 3.98 and normalizing it by 3.98 the spin tune in the magnetic field related to the momentum is obtained:

$$\nu_S^B = \gamma G. \quad (3.100)$$

The ratio between spin tune in electrical (3.97) and magnetic field (3.100) in *Yu. Senichev et. al.* [59] asserts that there is an energy region where the MDM spin oscillation is several times faster in an electric field than in a magnetic field. As a result, the concept of a quasi-frozen structure may be achieved on the basis of two lattice structure options. The first option is using two kinds of arcs: magnetostatic and electrostatic, with the latter having an inverse curvature, which is discussed in more detail in the reference [59]. This approach, however, inherits one disadvantage of cylindrical electrodes, namely the whole collection of high-order nonlinearities.

In the second choice of lattice, we employ the straight elements arranged on the straight sections with Wien filter fields to restore MDM spin rotation in the magnetic arcs. The lattice consists of two magnetic arcs and two straight sections with the Wien filters, where Lorentz force is equal to zero. The total length and field strengths of these elements are specified by the needed spin recovery condition.

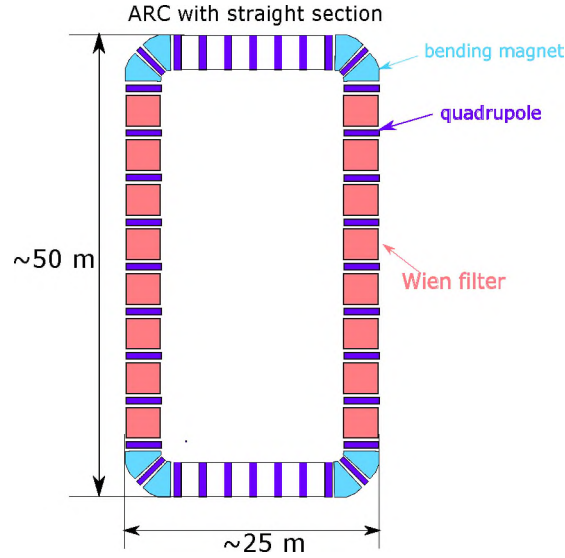


Figure 3.7: Quasi Frozen Spin lattice: The color-coded sections are shown in the figure above, with pink representing a static Wien filter with magnetic and electric fields perpendicular to each other, blue at arcs representing bending magnets, and violet representing focusing and defocusing quadrupoles. The lattice has two straight sections and two arcs.

Figure 3.7 shows the second option of the ring for the deuteron energy of 270 MeV based on this concept [60]. The lattice of this ring contains the dispersion-free straight sections in the arcs (figure 3.7) for the polarimeter, beam extraction and injection systems, and the RF cavity. Thus, the particles' momentum is rotated by the angle Φ_{arc}^B in the magnetic arc, while the spin is simultaneously rotated in the horizontal plane relative to the momentum by the angle $\Phi_s^{arc} = \gamma G \cdot \Phi_{arc}^B$. Straight elements with Wien filter fields on the straight section give MDM spin rotation in the horizontal plane in the opposite direction relative to the momentum in the electric field by an angle $\Phi_s^E = -\left(\gamma G + \frac{\gamma}{\gamma+1}\right) \beta^2 \cdot \Phi_{ss}^E$, Where Φ_{ss}^E is rotation of momentum vector in electric field E. And rotation of spin vector in horizontal plane relative to momentum in magnetic field B by an angle $\Phi_s^B = (\gamma G + 1) \Phi_{ss}^B$, where Φ_{ss}^B is rotation of momentum vector in magnetic field B. Because the Lorenz force is zero, the momentum vector rotation angles $\Phi_{ss}^B = \Phi_{ss}^E$ are equal. Therefore, the momentum rotation can be defined by any of the two above. The momentum rotation in the presence of a magnetic field is given by:

$$\Phi_{ss}^B = \frac{eB_{ss}}{m\gamma\nu} \cdot L_{ss}. \quad (3.101)$$

where B_{ss} and L_{ss} are the magnetic field and length of the straight element, respectively. To implement the idea of quasi-frozen spin, we must satisfy the following condition: $\Phi_s^B + \Phi_s^E = \Phi_{arc}^B$, which mean:

$$(\gamma G + 1) \cdot \Phi_{ss}^B - \left(\gamma G + \frac{\gamma}{\gamma+1}\right) \beta^2 \cdot \Phi_{ss}^E = \gamma G \cdot \pi. \quad (3.102)$$

The fundamental relation for the straight element parameters by performing simple transformations:

$$L_{\Sigma} E_{ss} = \frac{G}{G+1} \cdot \frac{mc^2}{q} \cdot \pi \beta^2 \gamma^3, \quad (3.103)$$

$$B_{ss} = -\frac{E_{ss}}{c\beta}. \quad (3.104)$$

where L_{Σ} denotes the total length of all straight components inside a single straight section.

Thus, to achieve a maximum electric field of 120 kV/cm, a magnetic field of less than 80 mT is required. The QFS lattice is used to do the numerical

simulation of three-dimensional spin-orbital motion using BMAD software, which will be discussed in detail in chapter 4.

3.6.4 RF Wien Filter Method (Partially Frozen Spin)

This method includes substantially updating an existing storage ring's lattice by adding an RF Wien filter in order to measure the particle EDM with an accuracy of at least 10^{-25} e-cm [61]. The aim of the method is to measure EDM by using a combination of radial electric and vertical magnetic, RF fields in a standard Wien filter configuration, where $\vec{E} = \vec{B} \times \vec{v}/c$ [62], which oscillates at the resonance frequency. This configuration cancels the Lorentz force in the Wien filter, hence eliminating the cause of the method's systematic uncertainties. Thus, particle movement within the RF Wien Filter should be unaffected. Unfortunately, this configuration also eliminates the Rabi-type resonance [63] between the EDM Ω_{EDM} and the horizontal spin component, since the oscillating part of the Lorentz force is equal to zero, so does the oscillating component of EDM, according to Eq. (3.78). Also, the RF Wien filter set to one of the spin-tuned resonances, $(1 + G\gamma)$, seems to be quite successful for measuring the particle EDM. This RF Wien filter is also referred to as a magic Wien filter or mWF.

This phenomenon can be described qualitatively. Without an mWF, the spin's planar components oscillate in the standard $g - 2$ mode. However, in the presence of the mWF's resonant fields, each planar component gets a zero-frequency mode, among other new modes. This implies that each spin's planar component now has a time-constant ("frozen") component. The mWF doesn't effect Ω_{EDM} , since $\Omega_{EDM} \propto \vec{B}_L \times \vec{B}_V$, where \vec{B}_V denotes dominant and constant part of magnetic field. As a consequence, the constant EDM torque $[(e\eta/2mc)(\vec{B}_L \times \vec{B}_V) \times (\vec{s}_L)_{frozen}]$ rotate the spin around the radial axis, where \vec{s}_L is the amplitude of longitudinal spin component. The parasitic resonance rotation of the spin caused by the particle magnetic moment does not occur concurrently, since the planned mWF fields regulate only the magnitude of the $g - 2$ frequency vector, not its direction, which should be perpendicular to the ring plane.

The obvious issue is how such a zero-frequency spin mode might arise. This can be answered by the following reasoning. Due to the fact that the modulation frequency of the $g - 2$ frequency [61] is equal to the $g - 2$ frequency

itself, the obtained spin $g - 2$ oscillations are clearly a superposition of an infinite number of integer $g - 2$ modes, $N\omega_{a0}$'s, and only of such modes. Where $N = 1$ is the first $g - 2$ dominant mode. $N = 0$ is the next biggest mode. This zero $g - 2$ frequency mode is the frozen spin mode, the emergence of which enables the observation of EDM. According to the original frozen spin concept (described in section 3.6.2), the $g - 2$ spectrum comprises just the $N = 0$ mode. Here, we have various modes available and used one of them to measure the EDM. Thus, the mWF approach can be referred to as the "partially frozen" spin method. For more details, please refer to [63].

Without a Wien filter and initial polarisation in the horizontal plane, a longitudinal component of the spin points equally in the direction of the momentum as in the opposite direction in a purely magnetic storage ring. As a result, the vertical polarisation caused by an EDM oscillates at about zero and the average value over time vanishes. Once the Wien filter is introduced into the storage ring the Wien filter rotates the spin along the vertical axis, so that the longitudinal component of the spin is not often parallel to the momentum direction, as it is anti-parallel to it. Therefore, a fraction of the vertical polarisation buildup of polarisation over time can be observed. COSY already had an RF Wien filter installed in it in order to conduct the precursor experiment for the first direct deuteron EDM measurement [64].

Chapter 4

Method To Control Systematics And Its Effects On Spin Precession

This chapter will discuss one of the methods for controlling systematic uncertainty in the search for EDM using the storage ring at a required sensitivity of 10^{-29} e·cm for proton and deuteron. To achieve such high level sensitivity, an unprecedented level of precision is necessary, and various factors are important to be considered. One of the major factors are the interaction of *electric quadrupole moment* (EQM) and *magnetic dipole moment* (MDM) with electromagnetic field gradients which can produce an effect of a similar order of magnitude as that expected for EDM. Therefore, spin tracking is done by introducing realistic fields and defining their gradients, as well as by extending the TBMT equation to evaluate the effect of MDM and EQM interactions with field gradients using BMAD software for Quasi Frozen Spin lattice (QFS lattice) 3.6.3. For this, first a two-dimensional magnetic field is defined in order to benchmark the tracking codes and later modify them with realistic three-dimensional equations along with their gradients. It has been demonstrated that although the effects of field gradients do not affect the determination of EDM, they do allow for precise determination of the magnitude of systematic uncertainty [65].

4.1 QFS Lattice

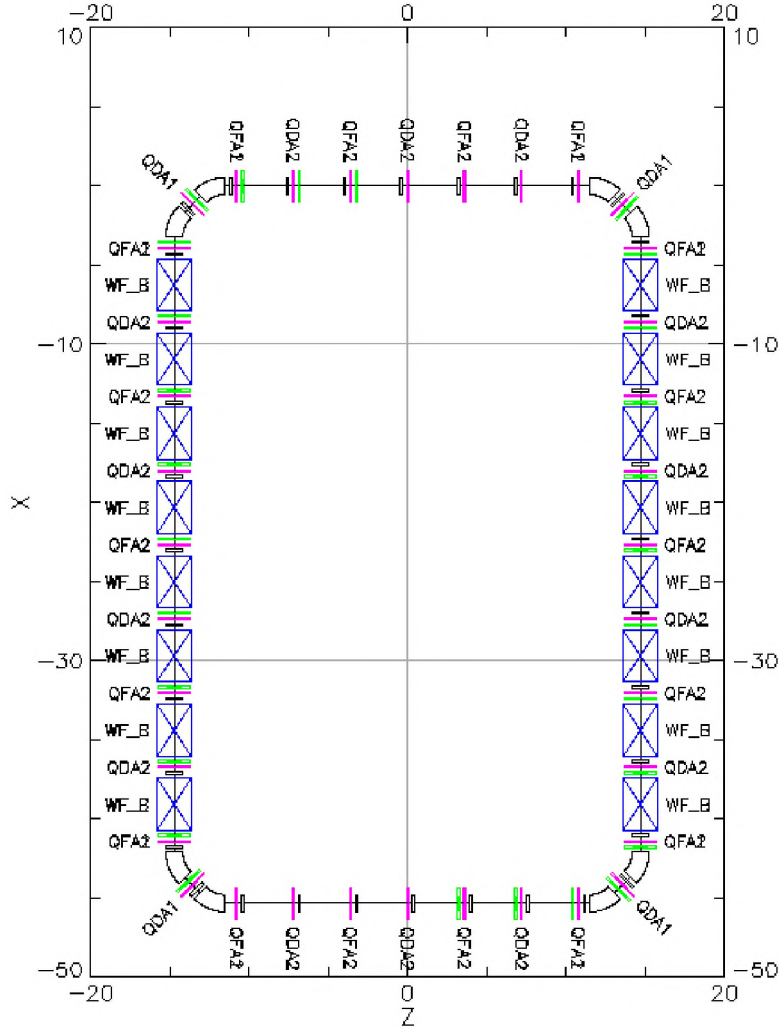


Figure 4.1: The QFS ring's floor plan. The color-coded sections are shown in the figure, with blue boxes representing a static Wien filter with magnetic and electric fields perpendicular to each other, black boxes at arcs representing bending magnets, magenta lines representing focusing and defocusing quadrupole configurations, and the green lines representing sextupoles.

Multipole type	l_{eff} [m]	Multipole strength [m^{-1}]
Dipole	1.820	0.431
Quadrupole (QFA1)	0.05	3.849
Quadrupole (QDA1)	0.05	-3.368
Quadrupole (QFA2)	0.05	2.908
Quadrupole (QDA2)	0.05	-2.963
Sextupole (SFP)	0.15	0.797
Sextupole (SDP)	0.15	-0.977
Sextupole (SFN)	0.15	-0.603
Sextupole (SDN)	0.15	1.091

Table 4.1: QFS elements’ effective length l_{eff} and their strengths. There are four families of quadrupoles and sextupoles.

In the section 3.6.3, we discussed the quasi frozen spin method and spin precession in the lattice. The QFS lattice floor plan is illustrated in figure 4.1 which depicts the schematic overview of the QFS lattice in the X-Z plane, as well as the configuration of each component. Numerical simulations are performed using BMAD software [45] for a single particle using the fourth-order Runge-Kutte integration algorithm, which is used for tracking. Here the step size is fixed for all elements 0.1 mm.

QFS lattice is dedicated for deuterons with 1042.24 MeV/c momentum (energy 270 MeV). Lattice consists of two straight sections and two arc sections. Four bending magnets are contained within each arc section, and each magnet has a magnetic field of 1.5 Tesla, a radius of curvature of 2.318 m, and deflects the beam by 45 degrees. In between the two arcs, there are two straight sections that consist of Wien filters, quadrupole and sextupole magnets. Quadrupoles are present in four families with different field strengths (table 4.1). The sextupoles are introduced into the storage ring’s lattice to correct chromaticity caused by the focusing elements in the lattice. A charged particle travelling off-center gets a kick equivalent to the square of its displacement from the centre in a sextupole, i.e. a sextupole operates as a quadrupole, with a focusing strength proportional to the closed orbit’s displacement from the sextupole centre. This allows for the correction of chromaticity since the closed orbit of off-momentum particles is shifted relative to the reference orbit. In QFS, lattice sextupoles are also present in a group of four with different field strengths for suppressing non-linear de-

coherence. Along with that, two straight section also contains eight Wien filters. There are a total of 72 quadrupoles and 25 sextupoles used in the lattice. The effective length l_{eff} and strength of QFS lattice magnets are listed in the table 4.1. The total circumference of the storage ring is 149.243 m.

Wien Filter In QFS Lattice

One of the important element of the QFS lattice (detailed discussion in section 3.6.3) is the Wien filter. The electric field used in our calculations is the maximum value reachable in the lattice given by [66], i.e., $E = 12 \text{ MV/m}$.

4.1.1 Optical Functions

Optical functions of the QFS model are depicted in figure 4.2. In the figure, the abscissa axis denotes the position along the ring, and the starting point for this is the point where the particle is injected. The particle's closed orbit motion, dispersion, and beta functions are plotted along with their position s on the ordinate axis after each element. In straight sections, dispersion is near zero, and dispersive effects are most noticeable in arcs. The dispersion function produced by dipoles propagates across these following elements and may also have negative values. For periodic machines, all of these sections between dipoles must be designed appropriately to ensure that the ultimate dispersion function equals zero at the machine's end. Only in this circumstance is it possible for the beam to circulate inside the ring. However, in the QFS lattice, the dispersion function is zero for the half ring. In the orbit plot, we can see that the particle's x-coordinate is in the order of 10^{-8} mm and the y-coordinate is zero. Visible deviations in figure 4.2 are due to numerical limitations. At the bottom of figure 4.2, the QFS lattice elements are shown in the same order as they are placed in the lattice. In a storage ring, the most important condition is that the dispersion should be zero at the end of the machine; otherwise, the particles will be lost in the storage ring.

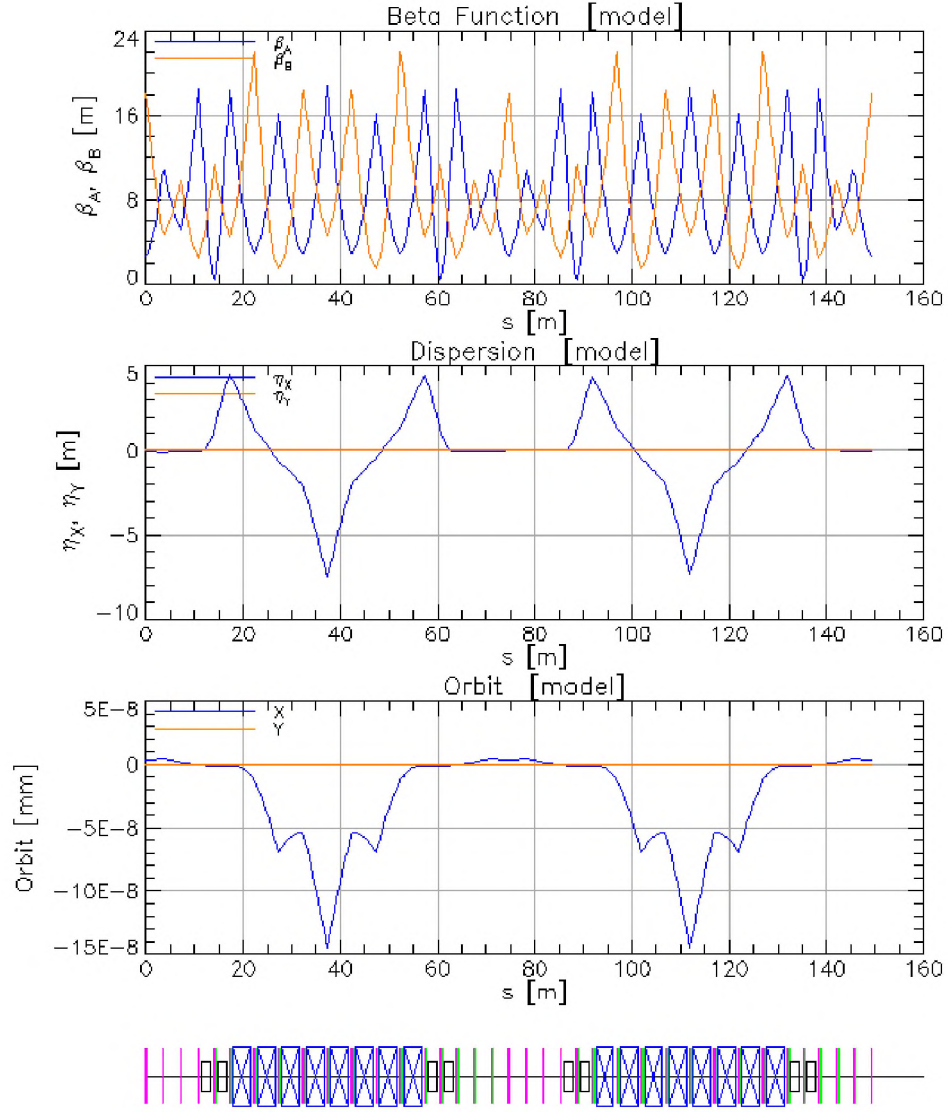


Figure 4.2: The beta functions β_A, β_B , dispersion η_x, η_y , and particle vertical coordinates (X and Y) in closed orbit in the QFS ring. At the bottom of the figure, the QFS lattice elements are shown. Where the blue boxes are Wien filter elements, the black boxes are bending magnets, the pink lines represent focusing and defocusing quadrupoles, and the green line represents sextupoles.

4.2 BMAD Simulations For Quasi-Frozen Spin Method

In this section a new method for dealing with systematic uncertainty will be discussed. To use this approach, one must extend the TBMT equation in BMAD software, which is discussed in the section 4.2.2. Because this approach uses EQM and MDM to interact with field gradients, fringe field definition in BMAD is required. In the end of this section we will compare between rectangular and fringe field.

4.2.1 New Method For Controlling Systematics

Electromagnetic field gradients are present in every storage ring that might be utilised for EDM measurement. When a particle with a magnetic dipole moment (MDM) and/or an electric quadrupole moment (EQM) interacts with field gradients, additional spin precession occurs. MDM values for proton and deuteron are known with a precision of 10^{-8} [67], and EQM values for deuteron with a precision of 10^{-3} [68, 69]. This precision is adequate to use the interaction of the MDM and EQM with field gradients to control systematic uncertainties in the EDM measurement to a level significantly less than that required to achieve the 10^{-29} e-cm sensitivity. Reproducing the known MDM and EQM results in the storage ring measurement would verify that all systematics are properly controlled.

4.2.2 Extending TBMT Equation

Analytical calculations are done for controlling systematics uncertainties for EDM measurement in a storage ring by measuring EQM [70], but this cannot account for all the effects in a storage ring. However, these calculations are used as a benchmark for further simulations. Using existing tracking codes, the spin precession equation may be numerically solved in combination with the equation of motion. However, none of the currently available tracking codes provides information on spin precession in the presence of field gradients. In the BMAD tracking code, the TBMT [51] equation has been extended to include MDM and EQM interaction with electromagnetic field derivatives in order to use the MDM and EQM interaction with field gradients to control systematic uncertainties in the EDM measurement to

a much lower level than necessary to reach the 10^{-29} e-cm sensitivity. A custom field equation for magnets has been added in the BMAD to perform a simulation with realistic three-dimensional fields with their field gradients. The extended TBMT equation is given as:

$$\begin{aligned}
\frac{d\vec{s}}{dt} = & \frac{q}{mc} \vec{s} \times \left[\left(\frac{g}{2} - 1 + \frac{1}{\gamma} \right) c\vec{B} - \left(\frac{g}{2} - 1 \right) \frac{\gamma c}{\gamma + 1} (\vec{\beta} \cdot \vec{B}) \vec{\beta} - \left(\frac{g}{2} - \frac{\gamma}{\gamma + 1} \right) \vec{\beta} \times \vec{E} \right] \\
& + \frac{D}{\hbar} \vec{s} \times \left[\vec{E} - \frac{\gamma}{\gamma + 1} (\vec{\beta} \cdot \vec{E}) \vec{\beta} + c\vec{\beta} \times \vec{B} \right] \\
& + \frac{gqI\hbar}{2m^2c^2} \frac{\gamma}{\gamma + 1} \left[\vec{s} \times (\vec{\beta} \times \vec{\nabla}) \right] \left\{ \vec{s} \cdot \left[c\vec{B} - \frac{\gamma c}{(\gamma + 1)} (\vec{\beta} \cdot \vec{B}) \vec{\beta} - \vec{\beta} \times \vec{E} \right] \right\} \\
& + \frac{Q\gamma}{\hbar(2I - 1)} \left\{ \vec{s} \cdot \left[\vec{\nabla} + \frac{\gamma}{\gamma + 1} \vec{\beta} \times (\vec{\beta} \times \vec{\nabla}) + \vec{\beta} \frac{\partial}{c\partial t} \right] \right\} \\
& \left\{ \vec{s} \times \left[\vec{E} - \frac{\gamma}{\gamma + 1} (\vec{\beta} \cdot \vec{E}) \vec{\beta} + c\vec{\beta} \times \vec{B} \right] \right\},
\end{aligned} \tag{4.1}$$

where D is the value of the electric dipole moment, Q is the value of the electric quadrupole moment, q is the charge of the particle, \vec{s} is the spin vector, m is the mass of the charged particle, I is the particle spin value, g is the g -factor, and \vec{E} and \vec{B} are electric and magnetic fields, respectively. Gradients of fields arise in this equation as a result of the $\vec{\nabla}$ operator acting on the B and E fields.

In equation 4.1, the first term is the standard BMT equation, the second term represents the EDM effect, the third term depicts the interaction between MDM and field gradients, whereas the fourth term is related to the interaction between EQM and field gradients. Since a particle with spin 1/2 has zero electric quadrupole moment (e.g. for a proton), the spin precession equation is reduced to the first three components of the TBMT equation. For proton (last term in equation 4.1 is zero) and deuteron, the coefficients in the last three terms of equation 4.1 are of the same order of magnitude. Additionally, for realistic experimental conditions, the term with time derivative $\partial/\partial t$ is much smaller than terms with field gradients, and therefore this particular term with $\partial/\partial t$ can be neglected. The other terms are 15–16 orders

less than the first term of the equation, which corresponds to the standard BMT equation.

4.2.3 Realistic Electromagnetic Field Definition

Before modification of the BMAD code, it is important to check the numerical limitations of the code.

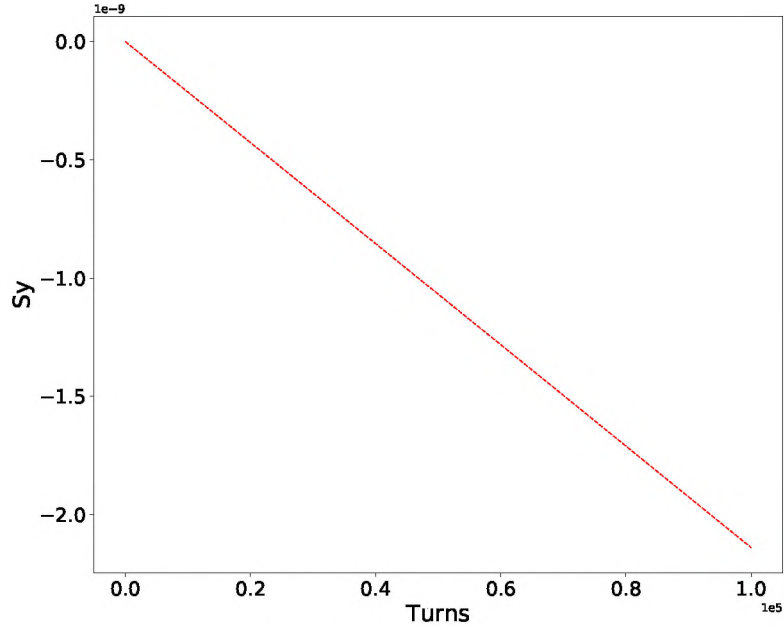


Figure 4.3: Background plot: vertical spin component accumulation for a reference particle (deuteron) without EDM, EQM, or MDM for 100,000 turns for defined lattice in section 4.1

Numerical Limitation

The tracking simulation model has some numerical restrictions, such as the vertical spin component for deuteron shows some vertical polarisation, which is of the order of 10^{-9} in the absence of EDM, EQM, and MDM (without

the 2nd, 3rd, and 4th parts of equation 4.1). This vertical spin component polarisation is referred as background and shown in the figure 4.3 for 100,000 turns.

Fringe Field

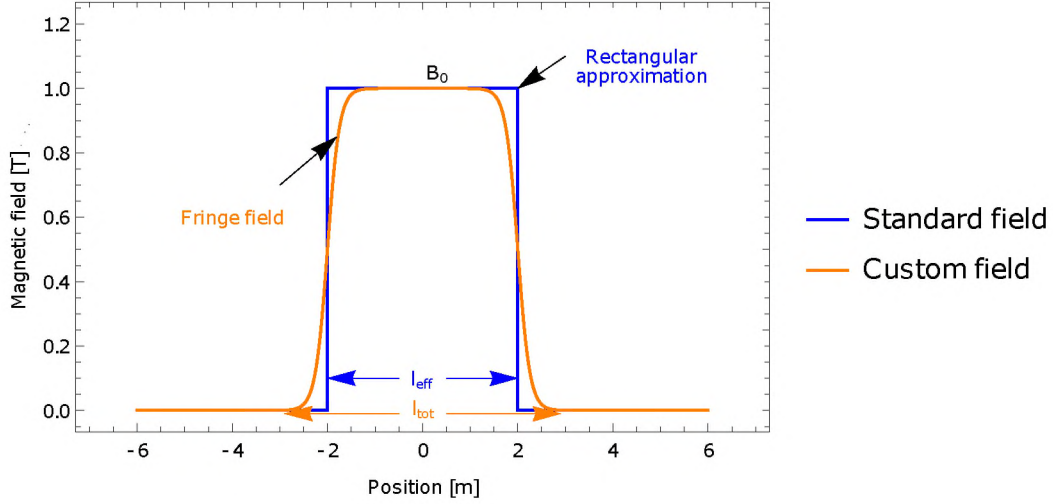


Figure 4.4: A comparison between the standard default field as defined in BMAD (denoted by the blue colour) and a custom field for dipole magnets, which was implemented in BMAD (denoted by the orange colour) with its fringe fields. Where l_{eff} is the actual physical length of the ideal dipole magnet. B_0 is the maximum field magnitude.

Ideal Magnets produce only transverse magnetic field components that stay constant inside the magnet and rapidly decay to zero once the magnet is over. However, in realistic magnet there are fringe fields at the magnets' ends that also include longitudinal component, where both transverse and longitudinal component of the field gradually diminishes to zero. As shown in figure 4.4, the fringe field is the region that lies at the edges of the magnets where there is a transition from maximum field to zero fields. In the figure 4.4, one can see the standard (ideal) dipole magnetic field used in BMAD. The customised or realistic magnetic field of the dipole along with its rectangular approximation is depicted. The rectangular approximation is the field

behaviour that is expected from an ideal dipole magnet (in which fields are maximum within the magnet and cut off as soon as the magnet is over). l_{eff} is the actual physical length of the dipole magnet. The rectangular approximation cuts off the fringe field at half its maximum.

In BMAD, new elements with custom magnetic fields are defined. Initially a simple two-dimensional (2D) magnetic field equation is implemented. Later on, a three-dimensional magnetic field using the Enge function [71] is introduced in BMAD. These new elements are referred to as **customized elements**. We will discuss this in further detail in subsequent sections.

4.3 2D Analytical Field Equations

As discussed earlier in section 4.2.2 realistic field definition is required for implementation of extended TBMT equation. All multipole magnets should have fringe fields their respective field gradients defined. By default, BMAD uses ideal magnet's field, which leads to an infinite field gradient. Therefore it was necessary to define custom fields for magnets in order to use the complete TBMT equation for spin precession.

The custom dipole's field was defined using an equation in which the field is approximated by the standard analytic mid-plane field profile for a soft-edged 2D dipole:

$$B_y(z) = \frac{B_0}{2} \left[\tanh \frac{\pi}{2a}(z + L) - \tanh \frac{\pi}{2a}(z - L) \right], \quad (4.2)$$

where $2L$ is the dipole magnet length, $2a$ is the gap between the poles, and B_0 is the magnetic field applied. This equation is applicable to particles in reference orbit.

The respective field gradient for the dipole is:

$$\frac{\partial B_y(z)}{\partial z} = \frac{B_0 \pi}{4a} \left(-\operatorname{sech}^2 \left(\frac{\pi(z - L)}{2a} \right) + \operatorname{sech}^2 \left(\frac{\pi(z + L)}{2a} \right) \right). \quad (4.3)$$

Other derivative components are equal to zero. When magnets with fringe fields are introduced in the lattice, it is important to adjust the length of the magnets and elements around it, otherwise total length of magnet increases,

which will increase the total length of the lattice. To solve this problem, every-time when some length is added to magnet due to fringe field implementation same length is subtracted from drifts around it. Modified field and its gradient are plotted as shown in figure 4.5.

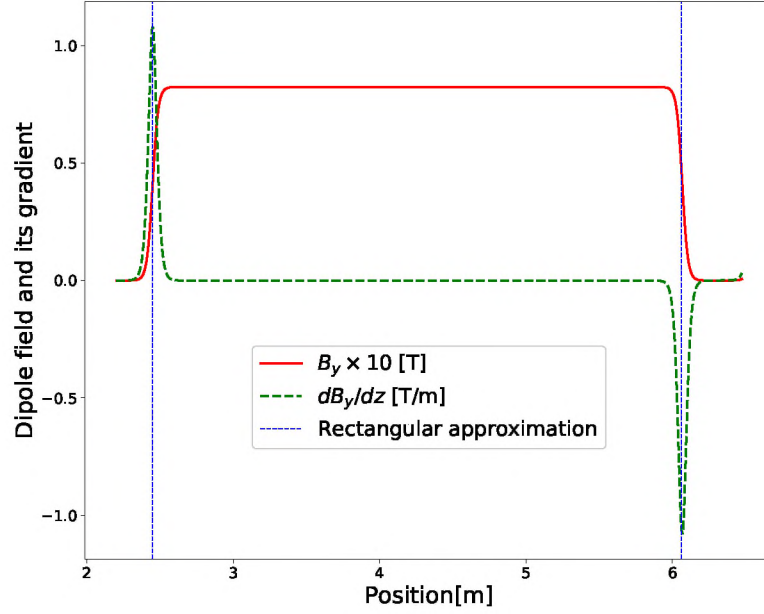


Figure 4.5: The dipole field (red solid line) as a function of z and its field gradient (green dashed line) are plotted as a function of position s . The magnet limits for the dipole's rectangular approximation, are shown by the blue dashed line. Magnetic field $B_y(z)$ is scaled up by a factor of 10.

The custom field equation for the Wien filter is also implemented in the BMAD. The Wien filter magnetic field $B_y(z)$ and electric field $E_x(z)$ is defined as a function of z using equation 4.2. Where B_w and E_w are the magnetic and electric field magnitudes. Knowing magnitude of one field (magnetic or electric) the magnitude of other field can be calculated using the Lorentz force equation.

Magnetic field gradient for the Wien filter ($\frac{\partial B_y(z)}{\partial z}$) is defined using 4.3, similarly electric field is defined as follows:

$$\frac{\partial E_x(z)}{\partial z} = \frac{E_w \pi}{4a} \left(-\text{sech}^2 \left(\frac{\pi(z-L)}{2a} \right) + \text{sech}^2 \left(\frac{\pi(z+L)}{2a} \right) \right). \quad (4.4)$$

Using standard fields for magnets in a Quasi Frozen Spin ring, the QFS condition (which states that spin oscillates around some average fixed direction coinciding with the momentum direction) is fulfilled with a precision of 10^{-9} and using customised magnetic fields, it is fulfilled with a precision of 10^{-6} .

After the implementation of simple two-dimensional customised field elements in BMAD, spin tracking simulations were performed. The vertical spin (per unit time) for EDM and EQM values is compared using both analytical and numerical methods. They are shown in table 4.2.

Method	S_y^{EDM}/t [s^{-1}]	S_y^{EQM}/t [s^{-1}]
Analytical	$3.2 \cdot 10^{-09}$	$4.7 \cdot 10^{-10}$
Numerical	$3.2 \cdot 10^{-09}$	$3.9 \cdot 10^{-10}$

Table 4.2: Comparison between the vertical spin component of spin obtained with analytical and numerical calculations for EDM and EQM per unit time, respectively.

After using customised magnetic field elements for symmetric Wien filter field setting (discussed in detail in section 4.5), the EDM signal S_y^{EDM}/t is $3.2 \cdot 10^{-9}$ e·m/sec, which agrees with the analytical calculations. Whereas for an EQM signal, S_y^{EQM}/t is $3.9 \cdot 10^{-10}$, which agrees with the analytical calculation for an asymmetric Wien filter setting by 84.6%. The ratio between the strengths of the EDM and EQM signals is 8.16, which implies that EDM is by order of magnitude larger than EQM. These results are used to benchmark tracking code with implemented complex three-dimensional fields using the Enge function and its field gradient effects.

4.4 3D Analytical Field Equations

The fringe field in multipole magnets has various effects on the linear and nonlinear dynamics of particles moving along an accelerator beam line [71]. In this section, analytical expressions for multipole complex fringe fields are presented. Using these analytical expressions, fringe field effects can be included in beam and spin dynamics simulations.

As discussed in 4.3, a realistic field definition is required for the TBMT equation to be implemented with electromagnetic field gradients. Three-dimensional realistic fields for dipole, Wien filter, and quadrupole are introduced into BMAD for spin tracking simulation to obtain these electromagnetic field gradients. The three-dimensional functions used to define these electromagnetic fields will be discussed in the following sections. Any mathematical function can be used to define the realistic electromagnetic field, but it must satisfy the Maxwell equations.

4.4.1 Dipole Field

The objective is to define multipole realistic magnetic field function that satisfy Maxwell's equations. In this section, analytical formulas [71] for realistic fields for dipoles are briefly discussed. The Enge function type falloff along the z -axis is used to define the dipole fringe field. B_y is dependent on the y and z coordinates. Similarly, B_z is dependent on the y and z coordinates, and their relation is as follows:

$$B_x = 0, \quad (4.5)$$

$$B_y = \frac{B_0}{2} \left(\frac{1}{(1 + e^{E(z+iy)})} + \frac{1}{(1 + e^{E(z-iy)})} \right), \quad (4.6)$$

$$B_z = \frac{B_0}{2} \left(\frac{-i}{(1 + e^{E(z+iy)})} + \frac{i}{(1 + e^{E(z-iy)})} \right). \quad (4.7)$$

where,

$$E(z + iy) = \sum_{n=0}^{N-1} A_n \left(\frac{z + iy}{2a} \right)^n. \quad (4.8)$$

For the set of N coefficients A_n , $2a$ is the aperture of the dipole. Taking B_x component zero [71]. The following components of dipole field gradients are implemented in BMAD:

$$\frac{\partial B(x, y, z)}{\partial(x, y, z)} = \begin{pmatrix} 0 & 0 & 0 \\ 0 & \frac{\partial B_y}{\partial y} & \frac{\partial B_y}{\partial z} \\ 0 & \frac{\partial B_z}{\partial y} & \frac{\partial B_z}{\partial z} \end{pmatrix} \quad (4.9)$$

Components of dipole field derivatives are expanded as follows:

$$\frac{\partial B_y}{\partial y} = \frac{B_0}{2} \left(\frac{e^{E(z-iy)} \partial E(z-iy) / \partial y}{(1 + e^{E(z-iy)})^2} - \frac{e^{E(z+iy)} \partial E(z+iy) / \partial y}{(1 + e^{E(z+iy)})^2} \right), \quad (4.10)$$

$$\frac{\partial B_y}{\partial z} = -\frac{B_0}{2} \left(\frac{e^{E(z-iy)} \partial E(z-iy) / \partial z}{(1 + e^{E(z-iy)})^2} - \frac{e^{E(z+iy)} \partial E(z+iy) / \partial z}{(1 + e^{E(z+iy)})^2} \right), \quad (4.11)$$

$$\frac{\partial B_z}{\partial y} = -\frac{B_0 i}{2} \left(\frac{e^{E(z-iy)} \partial E(z-iy) / \partial y}{(1 + e^{E(z-iy)})^2} - \frac{e^{E(z+iy)} \partial E(z+iy) / \partial y}{(1 + e^{E(z+iy)})^2} \right), \quad (4.12)$$

$$\frac{\partial B_z}{\partial z} = -\frac{B_0 i}{2} \left(\frac{e^{E(z-iy)} \partial E(z-iy) / \partial z}{(1 + e^{E(z-iy)})^2} + \frac{e^{E(z+iy)} \partial E(z+iy) / \partial z}{(1 + e^{E(z+iy)})^2} \right). \quad (4.13)$$

A three-dimensional plot for a complex three-dimensional dipole field can be seen in figure 4.6.

4.4.2 Quadrupole Field

Analytical field expressions used for defining quadrupole custom field equations in BMAD in terms of Cartesian coordinates are as follows:

$$B_x = B_0 \left(y + \frac{b}{2\sqrt{2}(1-b^2)} [\ln(1 + \exp^{\sqrt{2}z+ih}) - \ln(1 + \exp^{\sqrt{2}z-ih}) + \ln(1 + \exp^{\sqrt{2}z-i\bar{h}}) - \ln(1 + \exp^{\sqrt{2}z+i\bar{h}})] \right), \quad (4.14)$$

$$B_y = B_0 \left(x + \frac{ib}{2\sqrt{2}(1+b^2)} [\ln(1 + \exp^{\sqrt{2}z+ih}) - \ln(1 + \exp^{\sqrt{2}z-ih}) - \ln(1 + \exp^{\sqrt{2}z-i\bar{h}}) + \ln(1 + \exp^{\sqrt{2}z+i\bar{h}})] \right), \quad (4.15)$$

$$B_z = B_0 \left(\frac{ib^2}{\sqrt{2}(1-b^4)} [\ln(1 + \exp^{\sqrt{2}z+ih}) + \ln(1 + \exp^{\sqrt{2}z-ih}) \right.$$

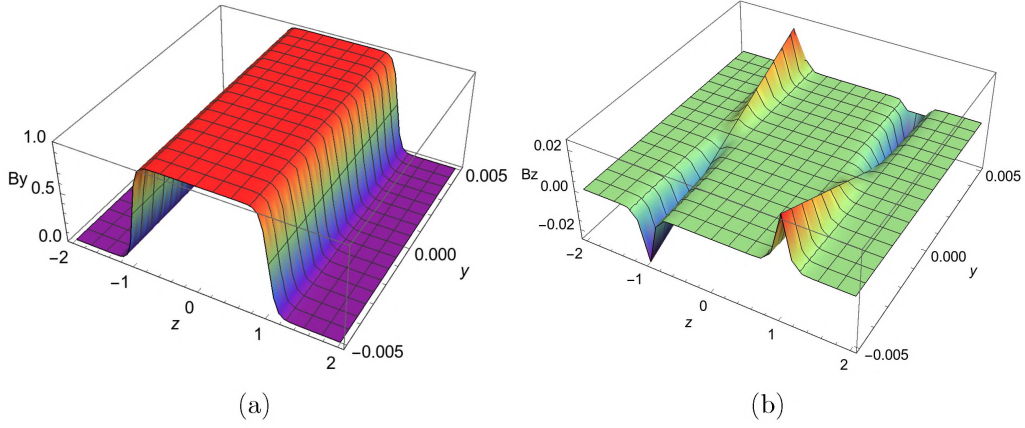


Figure 4.6: Dipole fields - (a) B_y component of a three-dimensional complex magnetic field as a function of y and z . (b) B_z component of three dimensional complex magnetic field as a function of y and z .

$$-\ln(1 + \exp^{\sqrt{2}z - i\bar{h}}) - \ln(1 + \exp^{\sqrt{2}z + i\bar{h}})] \Big). \quad (4.16)$$

Where b is the free parameter, and

$$\bar{h} = \frac{1}{\sqrt{2}} \left(\frac{1}{b} + b \right) x - \frac{i}{\sqrt{2}} \left(\frac{1}{b} - b \right) y, \quad (4.17)$$

$$h = \frac{1}{\sqrt{2}} \left(\frac{1}{b} + b \right) x + \frac{i}{\sqrt{2}} \left(\frac{1}{b} - b \right) y. \quad (4.18)$$

If b is real number, then \bar{h} is the complex conjugate of h . Dependency of B_x component on b is different from B_y component dependency on b as shown in equations 4.14 and 4.15. So if B_x and B_y is plotted as a function of z along $x = 0$, $y = r_0$ we will see different field variation along z , where r_0 is an arbitrary point. It implies that quadrupole field shows asymmetry, which is unexpected from a quadrupole magnet with fourfold rotational symmetry. Symmetry can be achieved if we add the same expressions as shown in equation 4.14, 4.15, and 4.16 to B_x , B_y , B_z respectively, by interchanging x and y , and dividing the equation by 2. For full symmetric solution, the value of parameter $b = 0.1$ is selected to define half symmetric field of quadrupole:

$$B_{x(sym)}(x, y, z) = \frac{B_x(x, y, z) + B_y(y, x, z)}{2}, \quad (4.19)$$

$$B_{y(sym)}(x, y, z) = \frac{B_y(x, y, z) + B_x(y, x, z)}{2}, \quad (4.20)$$

$$B_{z(sym)}(x, y, z) = \frac{B_z(x, y, z) + B_z(y, x, z)}{2}. \quad (4.21)$$

A half-symmetric field is shown in figure.

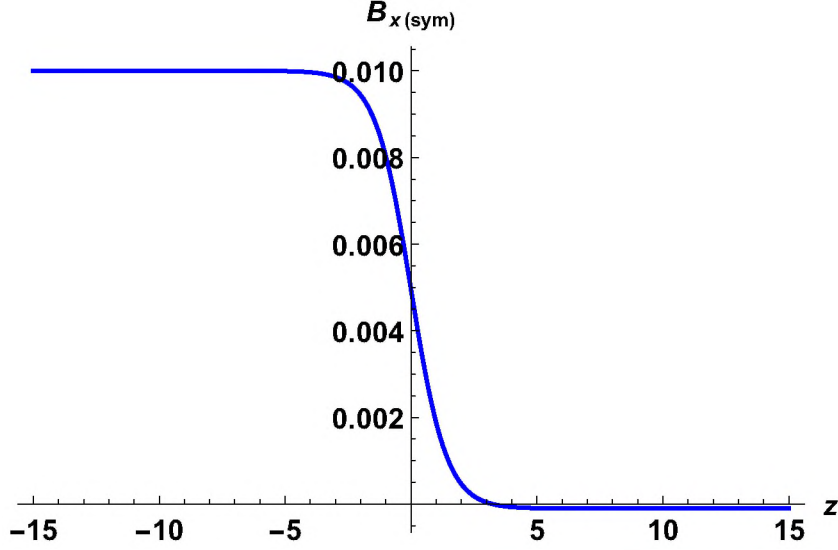


Figure 4.7: Half-symmetric fringe field $B_{x(sym)}(x, y, z)$ for quadrupoles using the Enge function (equation 4.19). This plot is for $x = 0.01, y = 0$.

In order to get full symmetric field equation of quadrupole, $B_{i(sym)}(x, y, z)$ with $(z = z + l_{eff}/2)$ is subtracted from $B_{i(sym)}(x, y, z)$ with $z = (z - l_{eff}/2)$, where $i = x, y, z$. Obtained equation are shown below:

$$B_{x(full)}(x, y, z) = B_{x(sym)}(x, y, (z - l_{eff}/2)) - B_{x(sym)}(x, y, (z + l_{eff}/2)), \quad (4.22)$$

$$B_{y(full)}(x, y, z) = B_{y(sym)}(x, y, (z - l_{eff}/2)) - B_{y(sym)}(x, y, (z + l_{eff}/2)), \quad (4.23)$$

$$B_{z(full)}(x, y, z) = B_{z(sym)}(x, y, (z - l_{eff}/2)) - B_{z(sym)}(x, y, (z + l_{eff}/2)). \quad (4.24)$$

Quadrupole three-dimensional field plots for the above equations are shown on figure 4.8.

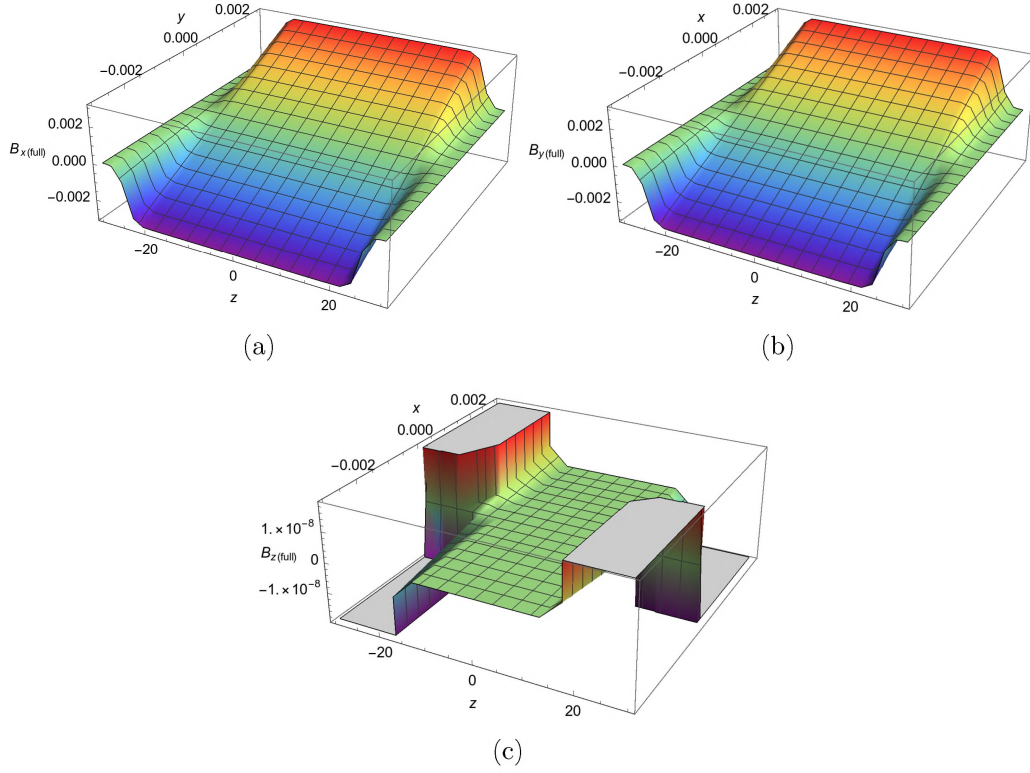


Figure 4.8: Field components of quadrupole (a), $B_{x(\text{full})}(x, y, z)$ where $x = 0$. (b), $B_{y(\text{full})}(x, y, z)$ where $y = 0$. (c), $B_{z(\text{full})}(x, y, z)$ where $y = 0.1$.

The following components of quadrupole field gradients are implemented in BMAD:

$$\frac{\partial B(x, y, z)}{\partial(x, y, z)} = \begin{pmatrix} \frac{\partial B_x}{\partial x} & \frac{\partial B_x}{\partial y} & \frac{\partial B_x}{\partial z} \\ \frac{\partial B_y}{\partial x} & \frac{\partial B_y}{\partial y} & \frac{\partial B_y}{\partial z} \\ \frac{\partial B_z}{\partial x} & \frac{\partial B_z}{\partial y} & \frac{\partial B_z}{\partial z} \end{pmatrix} \quad (4.25)$$

The expansion of equation 4.25 of derivatives for quadrupole for the full half-symmetric function is given in Appendix A.

Focusing And Defocusing In Quadrupole

The magnetic field at the quadrupole magnet's centre is zero, and Lorentz force $F_L = 0$. As a result, the particle travelling through the quadrupole's

centre remains unaffected. However, if the particle has an initial offset and does not pass through the centre, particle encounter magnetic field and therefore Lorentz force is nonzero, which results in focusing in one plane and defocusing in another plane.

4.4.3 Field For Wien Filter

The custom field equation for the Wien filter is also implemented in the BMAD. The magnetic field components of the Wien filter $B_y(z)$ and $B_z(z)$ are functions of y and z . Similarly, electric field components $E_x(z)$, $E_z(z)$ are also function of y and z as well. Field components $B_y(z)$ and $E_x(z)$ are defined using equations 4.6 and $B_z(z)$ and $E_z(z)$ are defined using equation 4.7 respectively. Also, in the Wien filter, magnetic and electric field magnitudes are $B_0 = B_w$ and $E_0 = E_w$. B_w magnitude can be calculated for respective E_w using Lorentz equation.

The following components of Wien filter electric field gradients are implemented in BMAD (magnetic field gradients are the same as a dipole in 4.9):

$$\frac{\partial E(x, y, z)}{\partial(x, y, z)} = \begin{pmatrix} 0 & \frac{\partial E_x}{\partial y} & \frac{\partial E_x}{\partial z} \\ 0 & 0 & 0 \\ 0 & \frac{\partial E_z}{\partial y} & \frac{\partial E_z}{\partial z} \end{pmatrix} \quad (4.26)$$

Components of the field derivative are the same as in equations 4.10 - 4.13.

Custom fields for dipole, quadrupoles, and Wien filters are implemented for the whole lattice using the above equations. The dipole and Wien filter is illustrated in figure 4.9. In lattice Sextupoles are still defined using standard BMAD fields.

4.4.4 Realistic Field For Two Quadrupoles (Superimposition Of Quadrupoles)

There are a few locations in the lattice where there are two quadrupoles that are placed together. When two adjacent quadrupole magnetic fields are defined without superimposing, then the two quadrupole fields have a gap in

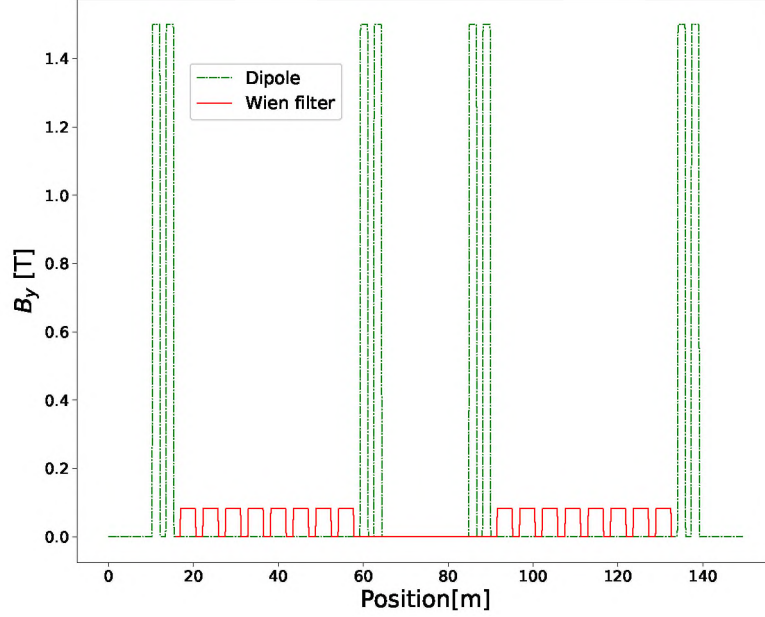


Figure 4.9: The vertical component of the magnetic field of the whole lattice after the introduction of complex magnetic fields for multipoles.

between them, which is not true in the real case. In reality, the fields of one quadrupole merge with those of another. They can have the same or different fields of strength. Since quadrupoles are placed close together, their fields overlap. Such a definition of quadrupoles is difficult to achieve using custom fields. To get an overlapped field, the superimposition of two quadrupole fields is done to get the resultant field. To accomplish this, the length of the drift before and after the first and second quadrupoles is reduced by half the length of the fringe field ($l_{tot} - l_{eff}$). To determine if the definition of overlapping quadrupoles with customised fields is correct in comparison to standard field quadrupoles, phase-space coordinates of the beam are compared before and after entering the superimposed quadrupole. For this purpose, the phase space coordinate of the beam is given an initial offset, $p_y = 0.0005$ (p_y is the phase space momenta which is normalised by the reference momentum p_0). Then, particle tracking simulations are performed to compare phase space

coordinates for superimposed quadrupoles for custom and standard magnetic field. The reason for giving an initial offset to the beam is to check if the quadrupoles with custom fields are working properly. The above procedure is applied when both the same quadrupoles (QDA2) are placed together, as well as when two different strengths of quadrupoles (QFA1 and QFA2) are placed together. A comparison of the obtained results from the simulation is shown in table 4.3. After implementing superimposed quadrupoles in the lattice, particle tracking is performed for the whole lattice to ensure that the particles do not get lost in the storage ring. The figure 4.10 compares the field defined for superimposed quadrupoles with a standard field and a customised field.

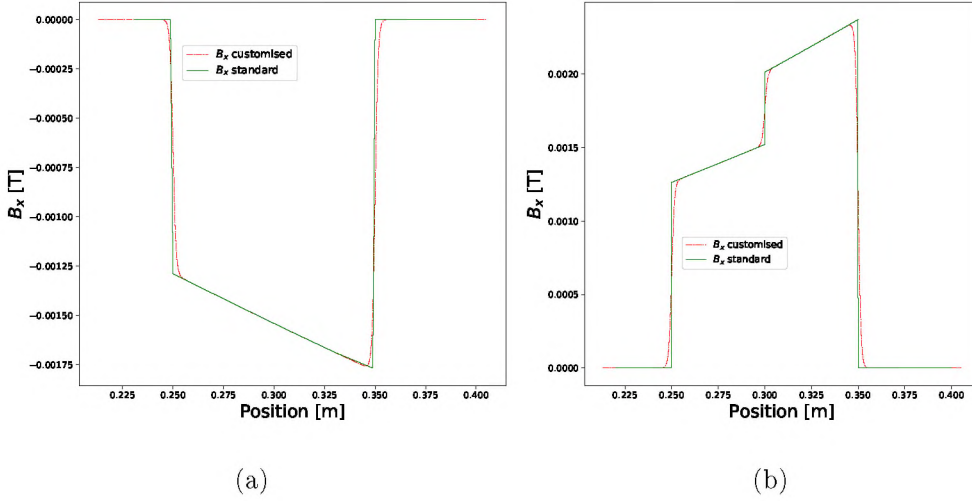


Figure 4.10: Quadrupole magnetic field (a) for identical quadrupoles QDA2, QDA2, (b) for different quadrupoles QFA1, QFA2. The initial phase space offset given to the beam is $p_y = 0.0005$. The customised (red dashed line) and standard field (green solid line) experienced by particle passing through superimposed quadrupoles.

Quadrupole setup	y	p_y
QDA1,QDA1 (Standard)	2.868E-004	4.558E-004
QDA1,QDA1 (Customised)	2.868E-004	4.558E-004
Ratio (Custom/Stand)	1.000	1.000
QFA1,QFA2 (Standard)	3.151E-004	5.503E-004
QFA1,QFA2 (Customised)	3.151E-004	5.503E-004
Ratio (Custom/Stand)	1.000	1.000

Table 4.3: Particle tracking after superimposed quadrupoles allows the comparison of standard and customised for quadrupole field definitions.

4.5 Spin Tracking

After implementing fringe fields for customised multipoles and also after the extension of the TBMT equation to include the interaction of EQM and MDM with field gradients, the QFS lattice spin tracking simulation is performed.

For EDM measurement, a symmetric field setting ($E_w = 12$ MV and its corresponding magnetic field) was used for Wien filters in both straight sections of the QFS lattice. For a symmetric field, spin oscillates horizontally about longitudinal direction as shown in figure 4.11 (a). These horizontal oscillations of the spin components (s_z, s_x) about the momentum direction are caused by the influence of bending magnets. Whereas, the Wien filter has such a field that it turns the spin back to the starting value. The vertical polarisation build-up of spin component s_y is generally due to both EDM and EQM. For EDM measurement in BMAD, a symmetric field is given to Wien filters, EQM is kept at 0 and EDM = 10^{-31} e·m, then the vertical polarisation buildup is due to EDM only for the initially horizontally polarised beam.

For EQM measurement, in BMAD, asymmetric field settings are used for the Wien filter, along with that EDM is kept at 0 and EQM = $0.2859 \cdot 10^{-30}$ e·m² [68, 69]. In the first straight section, the Wien filter has an $E_w = -12$ MV and in the other straight section, an $E_w = -37.6$ MV. For this lattice, spin evolution for four turns is shown in figure 4.11(b). In this case, both the spin components, such as s_x and s_z , vary very rapidly within their limits but do not recover their initial value after beam rotations in the lattice. And this

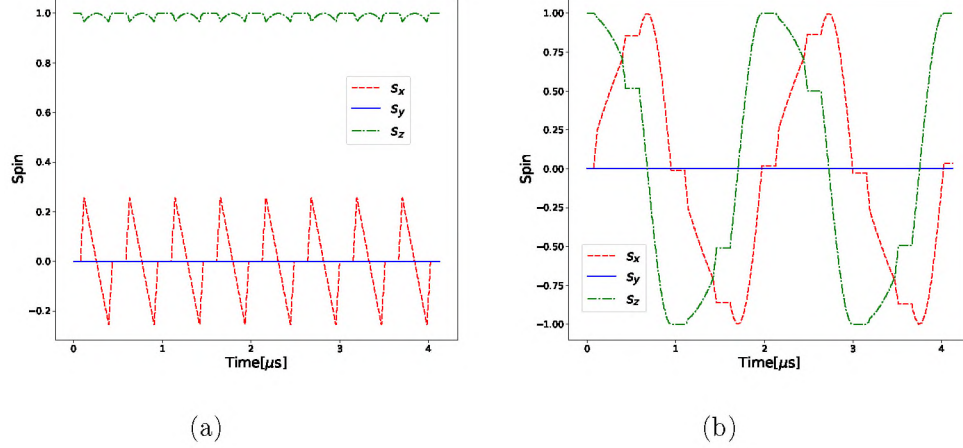


Figure 4.11: Spin evolution of particles along with four turns in the QFS lattice where s_x is denoted with a dashed red color, s_y with a solid blue line, and s_z is denoted with a green dashed dot line. Figure (a): Shows spin components for symmetric field configuration for Wien filters, (b) shows spin components for the asymmetric field setup of Wien filters.

asymmetric field definition for the Wien filter was done to see the EQM effect.

In the symmetric case, it was observed that when EDM is greater than zero, vertical polarisation increases linearly with time (see figure 4.12), but the impact of EQM interaction with field gradients averages to zero. Also in the same figure, the situation is inverted for asymmetric Wien filter settings. For non-zero EQM values, the s_y spin component increases linearly with time, but the EDM has no impact on vertical spin buildup.

The steps in the vertical polarisation of EDM and EQM values are visible in figure 4.12 because when particle with EDM experience the field of magnets, vertical polarisation builds up. When particles pass through a drift or non-magnetic area, non varying vertical polarisation is seen, resulting in a flat step and so on. As a result, step-like behaviour emerges. Similarly, when an EQM interacts with electromagnetic field gradients, it also exhibits step behavior.

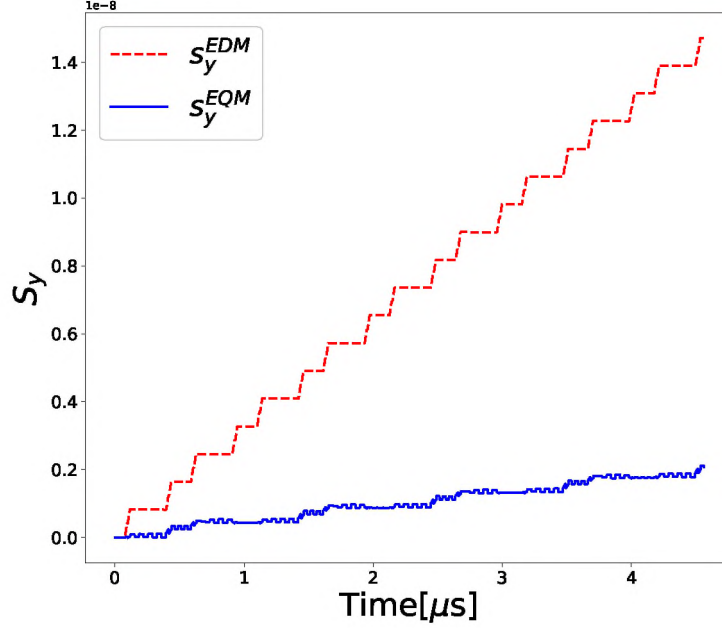


Figure 4.12: Comparison of vertical spin component for EDM effect for the symmetric field, denoted by a red dashed line, and for EQM effect using asymmetric field, denoted by the blue solid line for three-dimensional field equations.

4.6 Results And Discussion

In this chapter, we discussed the method for reducing systematic uncertainty in the search for EDM using QFS lattice at a required sensitivity of 10^{-31} e-m for protons and deuterons. The analytical model for this method is already discussed in [70]. In the above sections, we already described steps for the preparation of the BMAD simulation. Defining QFS lattice for BMAD software. Extension of the TBMT equation in the BMAD software was done for EQM and MDM interaction with electromagnetic field gradients. The gradients and 3-dimensional field equations for dipole, quadrupole, and Wien filters are defined. After these modifications, the influence of EQM and MDM interaction with electromagnetic field gradients on spin precession was analyzed [65].

The comparison of vertical spin component per unit time for EDM and EQM obtained after BMAD simulations using three-dimensional realistic field equations for magnets are:

$$S_y^{EDM}/t = 3.2 \cdot 10^{-09} s^{-1} \quad \text{EDM signal value ,} \quad (4.27)$$

$$S_y^{EQM}/t = 4.4 \cdot 10^{-10} s^{-1} \quad \text{EQM signal value.} \quad (4.28)$$

The ratio of the vertical spin component for the EDM and EQM is 7.2. which implies that the EDM and EQM signals had comparable orders of magnitudes (in the case of the QFS lattice examined) in both two-dimensional as well as three-dimensional field equations. It implies that EQM gradient interaction can be used to control systematic uncertainty in EDM measurement.

The conclusions of [70] and the current investigation suggest that when analysing the impacts of very small EDM values, the interaction of MDM and EQM with field gradients should be considered. It was shown that these additional effects are quite valuable for investigating the systematic uncertainties in high precision EDM measurements. At slightly different Wien filter settings, the EDM impact is 7.2 times greater than the EQM effect for an EDM value of 10^{-31} e.m. In the storage ring planned to achieve a precision of 10^{-31} e.m for EDM, reproducing the known deuteron EQM value with a precision of 10^{-3} should control systematic uncertainty to 10^{-34} e.m. This would enable us to reach the Standard Model prediction for the EDM value.

The current research [65] demonstrates that measuring the MDM and EQM interactions with field gradients can be very valuable for investigating the systematics of high-precision EDM measurements. This study evaluated the effects of one specific method of EDM measurement, but it is applicable to any proposed method for EDM measurement.

Chapter 5

Method For Evaluating Systematic Uncertainties Due To Magnet Misalignment In EDM Measurements Using A Storage Ring

In this chapter, we are going to introduce a method to evaluate the systematic uncertainties due to magnet misalignment in EDM measurement using a storage ring. This result has already been published in [72]. Magnet misalignment is a very common systematic uncertainty that can mimic the EDM effect. Additional uncertainties arise as a result of the positioning of the beam monitors used to control the beam orbit. As a result, a method that allows for the separation of these two effects is required for determining the sensitivity of EDM measurement. Therefore, a new novel method (first presented in [3]) for evaluating systematic uncertainty is proposed, which enables us to simultaneously evaluate the magnet misalignment and EDM induced effects. This method is possible only if two polarimeters are available in the storage ring, but they should be located at half the length of the storage ring. This proposed method can be applied to EDM measurement at COSY. In this chapter, first, a brief introduction to the COSY accelerator complex is given in section 5.1, followed by a description of the COSY lattice in section 5.2. Then a simple analytical calculation using Mathematica software of the proposed method was described in sections 5.3. A detailed description of nu-

merical calculations using BMAD software is presented in section 5.5. The final result and conclusion are presented in the section 5.8.

5.1 The Cooler Synchrotron COSY Accelerator Facility

The COSY accelerator facility is located at Forschungszentrum Jülich, Germany. Accelerator facility comprises of the ion source (polarised and unpolarised), the injector cyclotron Jülich, and the COSY (Cooler Synchrotron storage ring).

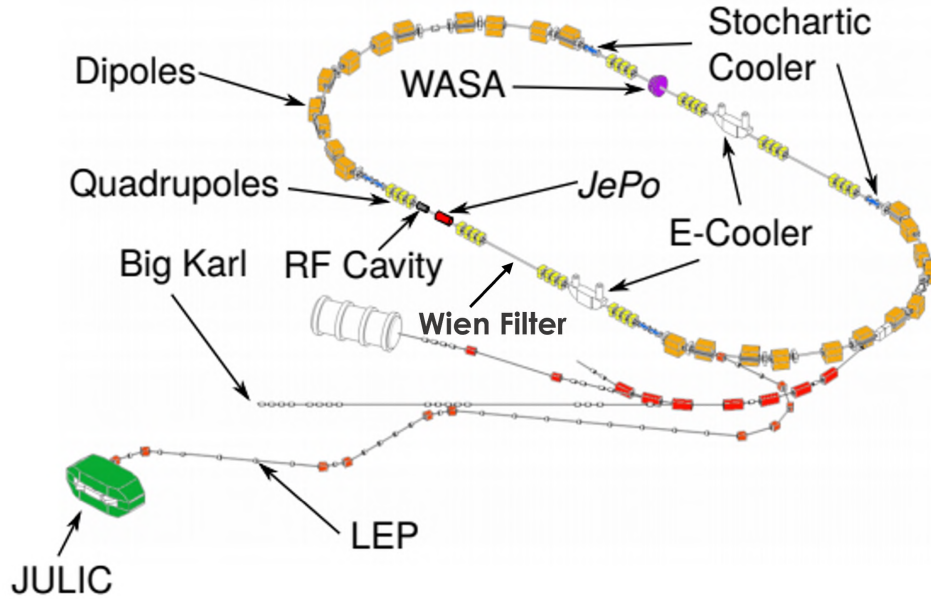


Figure 5.1: Schematic diagram of the COSY accelerator facility located in Jülich. Adapted from [73].

In figure 5.1 the schematic diagram of the COSY accelerator facility is shown. The COSY storage ring consists of multipole magnets, electron and stochastic cooling sections for reducing the emittance of beam, and two polarimeters (WASA and JePo), which are within half the length of the storage ring. So far, there has been a WASA forward detector present [74] in one straight

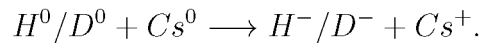
section for measuring beam polarisation in COSY, but recently a new polarimeter JePo (JEDI polarimeter) was installed [75, 76] in the straight section opposite to the WASA polarimeter.

Polarimeter Installment

In COSY, two polarimeters were installed: WASA (Wide Angle Shower Apparatus) and JePo [75, 76]. The target is installed in front of WASA just above the beam orbit. The target can also move within the beam pipe. After the beam achieves its final energy, the beam is excited, which leads to beam broadening. Some part of the beam is able to hit the target, and it scatters into the detector installed in front of it. Slowly, the full beam is extracted on target; the feedback loop between excitation and detector rate assures that. In another straight section, we have a JePo polarimeter. It is installed for better precision for measuring vertical polarisation required for EDM measurement.

Ion Source And Magnets Installation

COSY accelerator facility also comprises the ion source that provides the negatively charged hydrogen ions H^- or deuterium ions D^- . They can be unpolarized or polarised. The polarisation process occurs when ground state nuclear polarised [77] hydrogen or deuterium collides with an intense neutralised cesium beam:



Afterwards, particles can be accelerated by pre-accelerator JULIC (Jülich Isochronous Cyclotron) up to 45 MeV for H^- as well as up to 76 MeV for D^- beams. Subsequently, they are injected into the main synchrotron storage ring of COSY through the injection beamline. A small polarimeter, the LEP (low energy polarimeter), is installed on the injection beamline that can measure the beam polarisation [78]. Consequently, a deuteron or a proton beam electrons are removed using thin carbon foil from the ions by stripping reaction at the injection. The beam can be accelerated up to 3.7 GeV/c [79] in COSY, with the acceleration taking place in an RF cavity in the centre of one of the straight portions. The storage ring circumference is 183.4 m. It is made up of two straight sections of 40 m each and two arcs of 52 m each

[80]. Bending of the beam or keeping the beam in orbit is done by using 24 water-cooled dipoles with a magnetic field of up to 1.58 T. As well as the 56 magnetic quadrupoles being mounted to focus the beam, they are categorised based on dimensions and power supply in four families. COSY storage ring also comprises of 17 sextupoles, where 7 are located in straight sections and 10 in arcs for changing chromaticity. Orbit measurements are done by BPM (30) and 22 corrector magnets.

In the COSY ring, two methods are used for reducing beam emittances, such as cooling beams using a 2 electron cooler and a stochastic cooler. They significantly reduce the emittance of the beam. These cooling systems are:

Electron Cooling

There are two electron coolers in COSY, one present in each straight section. In the electron cooling method, electrons are accelerated with the same longitudinal velocity as the ion beam, whereas with a smaller transverse momentum spread. Electrons are guided by the magnets to a section joint in the main storage ring, where the ion beam interacts with electrons. The electron cooler was designed to cool protons with momenta up to 0.6 GeV/c. But later in 2013, a second COSY electron cooler was installed to deal with the entire energy range [81, 82]. When electrons and ion beam are in a joint section, the momentum distribution of the beam is effectively reduced due to Coulomb interaction. After the momentum distribution is reduced, the electrons are guided out of the beam pipe [83].

Stochastic Cooling

The stochastic cooler has two parts. The first is the "pickup detector", and the second is the "kicker". Stochastic cooling is intended for energy ranges greater than 1.5 GeV/c, according to [83, 84]. Stochastic cooling is done in such a way that first the particle beam crosses the "pickup detector". There, it measures the deviation of the particle beam from the closed orbit. Subsequently, when the particle reaches the "kicker" location present diagonally, the bump is applied according to the deviation measured.

Furthermore, many devices (RF solenoid, and Siberian snake) are installed in the ring to manipulate and detect the polarisation [85–87] of the bunched

beam, making COSY an ideal machine for studying the systematic influence on electric dipole moment experiment.

5.2 Lattice Of COSY

The spin tracking simulations for COSY ring are also performed using BMAD software. Spin tracking is done using the Runge-Kutta integration algorithm with an adjustable step size. COSY consists of various sets of magnets such as dipoles, quadrupoles, and sextupoles as shown in figure 5.2. The lengths of various magnets are listed in table 5.1.

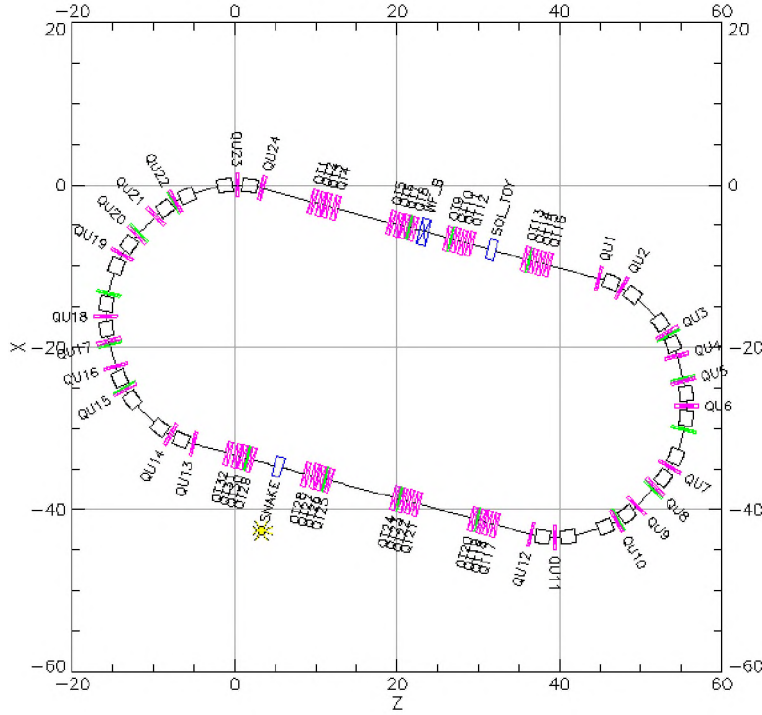


Figure 5.2: The COSY ring floor plan plotted using BMAD software. The color-coded sections are shown in the figure, with a blue-crossed box representing an RF Wien filter, black boxes at arcs representing bending magnets, magenta lines representing focusing and defocusing quadrupole configurations, the green lines representing sextupoles, and solenoids are represented by blue boxes.

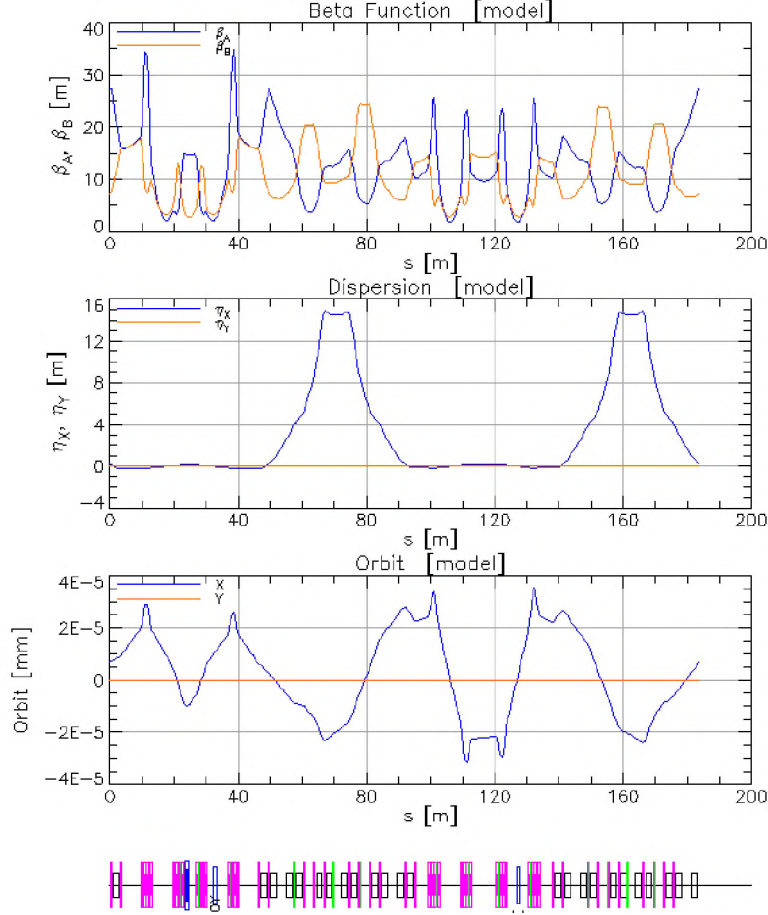


Figure 5.3: The beta functions β_A, β_B , dispersion η_x, η_y , and particle vertical coordinates in closed orbit in the COSY ring are shown in the figure. At the bottom of the figure, the QFS lattice elements are shown in the same order as they are placed in the lattice. The blue crossed box is the RF Wien filter, the black boxes are bending magnets, the magenta lines represent focusing and defocusing quadrupoles, and the green line represents sextupoles.

In the COSY lattice, an RF cavity is also shown, which is used for phase focusing. An RF Wien filter is also introduced in one of the straight sections. BPM's beam position monitors are inserted for determining beam position. The magnet misalignments taken from Wagner et. al. [88] are also introduced into the simulation.

Multipole type	l_{eff} in meters
Dipole	1.832
Quadrupole (arc)	0.372
Quadrupole (straight)	0.620
Sextupoles ("G")	0.328
Sextupoles ("L")	0.243
Sextupoles ("S")	0.140
Wien filter	1.10

Table 5.1: COSY element's effective length l_{eff} .

The optical functions of the COSY lattice are shown in figure 5.3. In this figure, the location of lattice elements along beam direction (in figure as position s) is also shown, Where the initial position 0 is assigned to the injection point. In second subplot of the figure, the dispersion in the straight sections is nearly zero because of the specified magnet settings. As a consequence, dispersive effects are primarily generated in the arc sections. In the closed orbit plot (in figure 5.3 depicted as orbit [model]), we can see that the closed orbit's X coordinate is in the order of 10^{-5} mm and Y coordinate is zero. Visible deviations of closed orbit's X coordinate from zero value are due to numerical limitations.

5.3 Analytical Calculation Using Mathematica

A simplified analytical model for evaluating systematic uncertainties due to magnet misalignment is discussed in this section. This model made it possible to develop a method that allows one to directly determine the effect of magnet misalignment on the vertical spin component. Mathematica software is used to do analytical calculations of the vertical spin component's time dependence $S_y(t)$ using similar reasoning as that followed in [70]. In this method, it was assumed that there are drift spaces and magnetic dipoles with bending radius ρ are present. It was assumed that a particle has fixed energy and is moving all the time in a fixed closed orbit. The Fourier series represents the form of the vertical ($B_V(t)$) and horizontal ($B_H(t)$) magnetic field components (in the time domain) along the particle trajectory, which are given by the following equations:

$$B_H(t) = \frac{H_0^c}{2} + \sum_{j=1}^{\infty} H_j^c \cos j\omega_o t + \sum_{j=1}^{\infty} H_j^s \sin j\omega_o t, \quad (5.1)$$

$$B_V(t) = \frac{V_0^c}{2} + \sum_{j=1}^{\infty} V_j^c \cos j\omega_o t + \sum_{j=1}^{\infty} V_j^s \sin j\omega_o t. \quad (5.2)$$

Here, $\omega_o = \beta c V_0^c / (2\rho)$ is the orbital frequency of a particle that is moving in a closed orbit. Particle velocity is given by βc and Fourier coefficients such as H_i^c, H_i^s, V_i^c , and V_i^s describe horizontal and vertical magnetic field distribution.

BMT equation [50] was solved by neglecting small effects due to the EDM and horizontal magnetic fields induced by magnets misalignments. The solution for horizontal spin component $S_z(t)$ along with the particle momentum is given by:

$$S_z(t) = \sum_{k=0}^{\infty} \cos\left(\omega_s t + k\frac{\pi}{2}\right) \frac{\Phi^k}{k!}, \quad (5.3)$$

$$\Phi = \frac{2\omega_s}{\omega_o V_0^c} \sum_{n=1}^{\infty} \frac{1}{n} (V_n^s - V_n^s \cos n\omega_o t + V_n^c \sin n\omega_o t). \quad (5.4)$$

Where ω_s is the spin precession frequency in the main vertical field for guiding and g is the g factor of the particle. Also, the relation between spin precession frequency and orbital frequency is given by:

$$\omega_s = \gamma \omega_o \left| \frac{(g-2)}{2} \right|. \quad (5.5)$$

Using this solution, time dependence of vertical spin component $S_y(t)$ [70] is calculated for misalignment $S_y^m(t)$ and EDM effects $S_y^e(t)$ such omega as:

$$S_y^m(t) = \omega_s \int_0^t B_H(t') s_z(t') dt', \quad (5.6)$$

$$S_y^e(t) = \omega_e \int_0^t B_V(t') s_z(t') dt'. \quad (5.7)$$

here, $\omega_e = D\beta c B_0/\hbar$ and D is the EDM value.

Substituting $k = 0$ in equation 5.3, the leading order vertical spin component $S_y^m(t)$ (magnet misalignment) and $S_y^e(t)$ (EDM effects) is obtained and their time dependence is:

$$S_y^m(t) = \frac{\sin \omega_s t}{2} H_0^c + \frac{\omega_s}{2} \sum_{i=1}^{\infty} \left[\left(\frac{\sin(i\omega_o - \omega_s)t}{i\omega_o - \omega_s} + \frac{\sin(i\omega_o + \omega_s)t}{i\omega_o + \omega_s} \right) H_i^c - \left(\frac{\cos(i\omega_o - \omega_s)t}{i\omega_o - \omega_s} + \frac{\cos(i\omega_o + \omega_s)t}{i\omega_o + \omega_s} \right) H_i^s \right], \quad (5.8)$$

$$S_y^e(t) = \frac{\omega_e \sin \omega_s t}{2\omega_s} V_0^c + \frac{\omega_e}{2} \sum_{i=1}^{\infty} \left[\left(\frac{\sin(i\omega_o - \omega_s)t}{i\omega_o - \omega_s} + \frac{\sin(i\omega_o + \omega_s)t}{i\omega_o + \omega_s} \right) V_i^c - \left(\frac{\cos(i\omega_o - \omega_s)t}{i\omega_o - \omega_s} + \frac{\cos(i\omega_o + \omega_s)t}{i\omega_o + \omega_s} \right) V_i^s \right]. \quad (5.9)$$

Next-to-leading order terms for $S_y^m(t)$ and $S_y^e(t)$ are obtained for $k = 1$ in equation 5.3, and their time dependence is:

$$\begin{aligned} S_y^m(t) = & \frac{\omega_s^2}{2\omega_o V_0^c} \sum_{i=1}^{\infty} H_0^c \left[\left(\frac{2 \cos \omega_s t}{\omega_s} + \frac{\cos(i\omega_o - \omega_s)t}{i\omega_o - \omega_s} - \frac{\cos(i\omega_o + \omega_s)t}{i\omega_o + \omega_s} \right) \frac{V_i^s}{i} \right. \\ & - \left. \left(\frac{\sin(i\omega_o - \omega_s)t}{i\omega_o - \omega_s} - \frac{\sin(i\omega_o + \omega_s)t}{i\omega_o + \omega_s} \right) \frac{V_i^c}{i} \right] \\ & + \sum_{j=-\infty, j \neq 0}^{\infty} \left[\left(\frac{\cos((i+j)\omega_o - \omega_s)t}{(i+j)\omega_o - \omega_s} - \frac{\cos((i+j)\omega_o + \omega_s)t}{(i+j)\omega_o + \omega_s} \right) \frac{H_i^s V_{|j|}^c}{j} \right. \\ & - \left(\frac{\sin((i+j)\omega_o - \omega_s)t}{(i+j)\omega_o - \omega_s} - \frac{\sin((i+j)\omega_o + \omega_s)t}{(i+j)\omega_o + \omega_s} \right) \frac{H_i^c V_{|j|}^c}{j} \\ & + \left(\frac{\sin((i+j)\omega_o - \omega_s)t}{(i+j)\omega_o - \omega_s} - \frac{\sin((i+j)\omega_o + \omega_s)t}{(i+j)\omega_o + \omega_s} - \frac{\sin(i\omega_o - \omega_s)t}{i\omega_o - \omega_s} \right. \\ & + \left. \frac{\sin(i\omega_o + \omega_s)t}{i\omega_o + \omega_s} \right) \frac{H_i^s V_{|j|}^s}{j} + \left(\frac{\cos((i+j)\omega_o - \omega_s)t}{(i+j)\omega_o - \omega_s} \right. \\ & - \left. \frac{\cos((i+j)\omega_o + \omega_s)t}{(i+j)\omega_o + \omega_s} - \frac{\cos(i\omega_o - \omega_s)t}{i\omega_o - \omega_s} + \frac{\cos(i\omega_o + \omega_s)t}{i\omega_o + \omega_s} \right) \frac{H_i^c V_{|j|}^c}{j} \left. \right] \quad (5.10) \end{aligned}$$

$$\begin{aligned}
S_y^e(t) = & \frac{\omega_e \omega_s}{2\omega_o V_0^c} \sum_{i=1}^{\infty} V_0^c \left[\left(\frac{2 \cos \omega_s t}{\omega_s} + \frac{\cos(i\omega_o - \omega_s)t}{i\omega_o - \omega_s} - \frac{\cos(i\omega_o + \omega_s)t}{i\omega_o + \omega_s} \right) \frac{V_i^s}{i} \right. \\
& - \left. \left(\frac{\sin(i\omega_o - \omega_s)t}{i\omega_o - \omega_s} - \frac{\sin(i\omega_o + \omega_s)t}{i\omega_o + \omega_s} \right) \frac{V_i^c}{i} \right] \\
& + \sum_{j=-\infty, j \neq 0}^{\infty} \left[\left(\frac{\cos((i+j)\omega_o - \omega_s)t}{(i+j)\omega_o - \omega_s} - \frac{\cos((i+j)\omega_o + \omega_s)t}{(i+j)\omega_o + \omega_s} \right) \frac{V_i^s V_{|j|}^c}{j} \right. \\
& - \left(\frac{\sin((i+j)\omega_o - \omega_s)t}{(i+j)\omega_o - \omega_s} - \frac{\sin((i+j)\omega_o + \omega_s)t}{(i+j)\omega_o + \omega_s} \right) \frac{V_i^c V_{|j|}^s}{j} \\
& + \left(\frac{\sin((i+j)\omega_o - \omega_s)t}{(i+j)\omega_o - \omega_s} - \frac{\sin((i+j)\omega_o + \omega_s)t}{(i+j)\omega_o + \omega_s} - \frac{\sin(i\omega_o - \omega_s)t}{i\omega_o - \omega_s} \right. \\
& + \left. \frac{\sin(i\omega_o + \omega_s)t}{i\omega_o + \omega_s} \right) \frac{V_i^s V_{|j|}^s}{j} + \left(\frac{\cos((i+j)\omega_o - \omega_s)t}{(i+j)\omega_o - \omega_s} \right. \\
& - \left. \frac{\cos((i+j)\omega_o + \omega_s)t}{(i+j)\omega_o + \omega_s} - \frac{\cos(i\omega_o - \omega_s)t}{i\omega_o - \omega_s} + \frac{\cos(i\omega_o + \omega_s)t}{i\omega_o + \omega_s} \right) \frac{V_i^c V_{|j|}^c}{j} \Big] \quad (5.11)
\end{aligned}$$

In fact, the formulas for misalignment and EDM-induced vertical polarisation are very similar and differ only in the normalising factor and Fourier coefficients describing the horizontal and vertical magnetic fields. Therefore, the misalignment and EDM effects are indistinguishable, and the contributions of both effects will add up coherently, leading to a common vertical spin component. Then the only chance to distinguish between these effects is to perform a Fourier analysis of the vertical spin component and examine the Fourier amplitudes, which depend on the field Fourier coefficients.

5.4 Fourier Analysis Of Vertical Spin Component

From the model presented in section 5.3 it is easy to deduce that the Fourier analysis of the harmonic time dependence of the vertical spin components $S_y^e(t)$ and $S_y^m(t)$ should give maxima of the Fourier amplitudes $F(\omega_s)$ at a frequency of $\omega = \omega_s$ and $F(\omega_o \pm \omega_s)$ at a frequency of $\omega = \omega_o \pm \omega_s$ (and at higher frequencies $\omega = 2\omega_o \pm \omega_s$, etc.). The Fourier amplitudes $F(\omega_s)$ and $F(\omega_o \pm \omega_s)$ are proportional to the Fourier coefficients which describe the

horizontal and vertical components of the magnetic field.

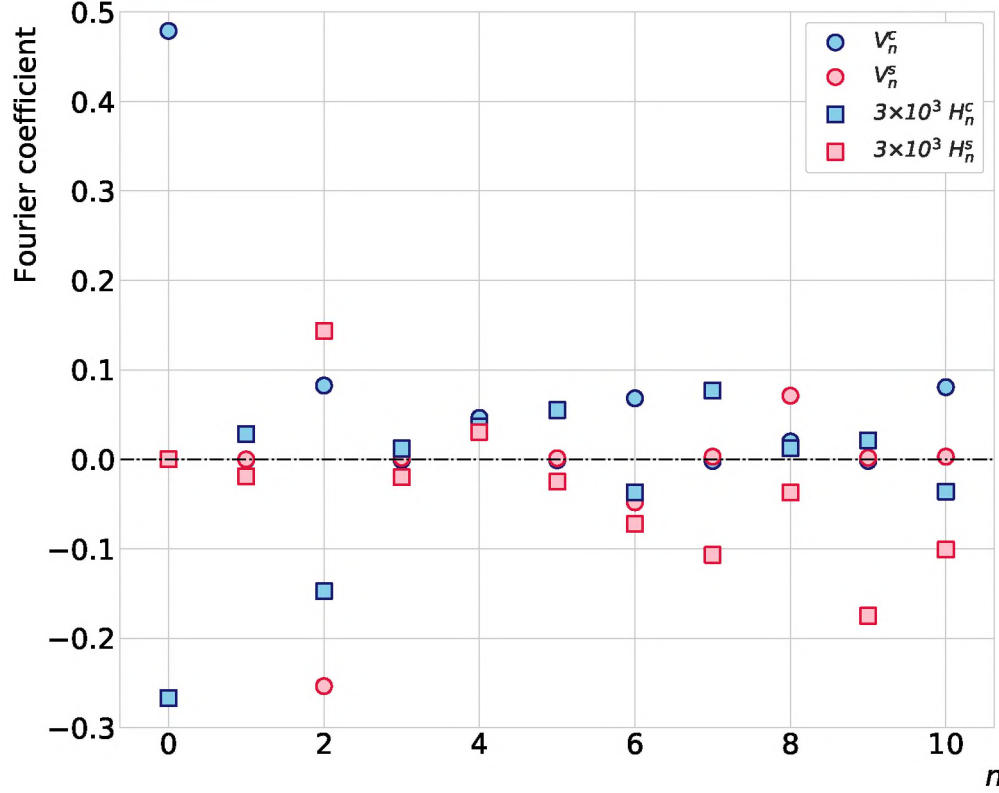


Figure 5.4: We can see the Fourier cosine coefficients, i.e., vertical V_n^c (blue full circles) and horizontal H_n^c (blue full square). As well as Fourier sine coefficients are vertical V_n^s (crimson full circle) and horizontal H_n^s (crimson full squares). Only dipole magnets field was considered. Dipole magnets are randomly rotated (Gaussian distribution with a mean value equal to zero and a standard deviation $\sigma = 5$ mrad) around the beam axis.

To compare the effects caused by magnet misalignments and the EDM, it is instructive to check the first terms in equations 5.8 and 5.9 together as well as the values of Fourier coefficients describing horizontal and vertical fields. Since the storage ring usually has rotational symmetry (at least of order 2), the odd Fourier coefficients are equal zero for undistributed vertical fields. COSY consists of two identical bending sections and two identical straight

sections, so COSY also has rotational symmetry. There are 24 COSY dipole magnets randomly rotated (Gaussian distribution with a mean value equal to zero and a standard deviation $\sigma = 5\text{mrad}$) around the beam axis for which the Fourier coefficient is calculated.

The obtained Fourier coefficients are shown in figure 5.4. The horizontal and vertical dipole magnetic field for small-angle δ_m scale with δ_m^2 and $1 - \delta_m^2/2$ respectively. This implies that vertical field Fourier coefficients are slightly affected by magnet rotations, so only even coefficients are large, but odd coefficients are 100-1000 factors small. In the case of horizontal fields, the Fourier coefficients take random values being a factor of about 3000 smaller than the vertical coefficients.

The general behavior of Fourier coefficients describing vertical and horizontal magnetic fields determines the time dependence of the vertical spin component induced by EDM and misalignment effects shown in figure 5.5. It can be seen that the term that contains the coefficient V_o^c completely dominates $S_y^e(t)$ and is mainly described by the function $\sin \omega_s t$. Harmonic functions of higher frequencies, on the other hand, contribute significantly to the time dependence of $S_y^m(t)$. Therefore, the Fourier analysis of a vertical spin component should provide information on the effect of magnet misalignment on a vertical spin component. Experimentally, this information could be extracted by sampling vertical spins with a frequency of at least $2\omega_o$. Such a sampling is also indicated in figure 5.5.

The Fourier analysis for the signal calculated using the sum of equations 5.8 and 5.10 for misalignment effect and for EDM effect (with $D = 10^{-21}$ e-cm) i.e. the sum of equations 5.9 and 5.11 has been performed. The signals were sampled at a frequency of $2\omega_o$, which corresponds to vertical polarisation measurements at two positions in the storage ring. Figure 5.6 shows the resulting Fourier amplitudes for both the effects. There is only one maximum for the EDM effect at frequency ω_s and two maxima for the frequency ω_s and $\omega_o - \omega_s$ are seen for the misalignment effect. This characteristic feature enables us to determine the contribution of the misalignment effect, which is visible in the Fourier amplitude $F(\omega_s)$ of the EDM signal.

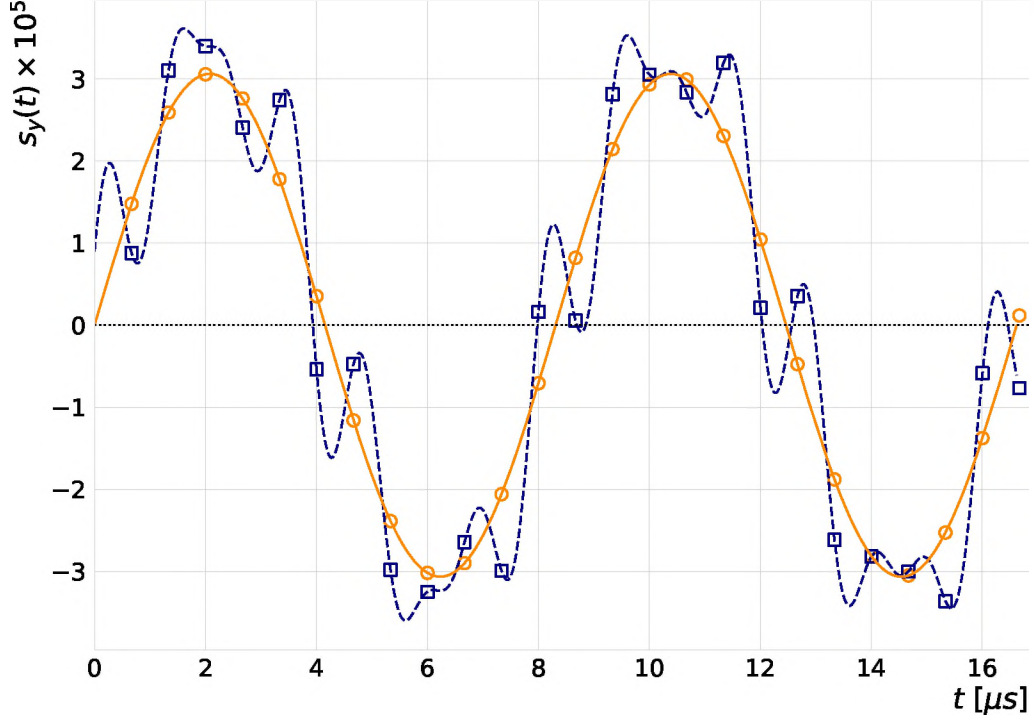


Figure 5.5: $S_y^m(t)$ is the vertical spin component due to magnet misalignment (represented by a dashed navy blue line) and $S_y^e(t)$ is the vertical spin component due to EDM of $D = 10^{-21}$ e-cm (represented by a solid orange line). Symbols denote the sampling results of vertical spin component with a frequency set to $2\omega_e$, for misalignment (navy blue square) and EDM effects (orange circle). In order to compare the amplitude of the misalignment effect with the EDM effect, the amplitude of the misalignment effect is artificially scaled in the figure.

5.5 BMAD Simulations For EDM And Misalignment Effects

In the last section, a method that can distinguish between EDM and magnet misalignment effects was developed using a simple analytical model. This model is, however, confined only to the closed orbit. The closed orbit is

also distorted by quadruple fields, which cannot be easily perceived in the analytical model. Consequently, with the BMAD software library, a further detailed analysis of spin evolution was performed.

5.5.1 Magnets Misalignment Introduction

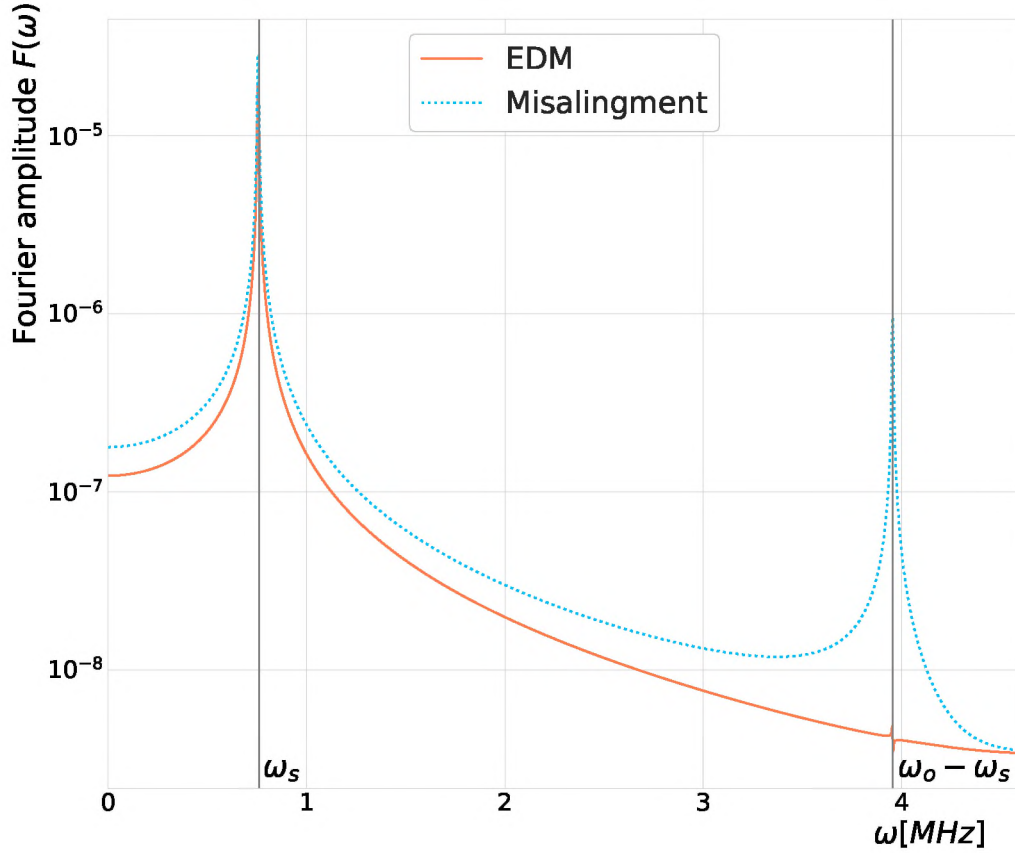


Figure 5.6: We can see the $F(\omega)$ i.e., Fourier amplitude for misalignment effect is denoted by (dotted sky blue line) and for EDM effect (solid orange color line) for $D = 10^{-21}$ e·cm for sampling frequency of $2\omega_o$. Two vertical lines mark the Fourier amplitude maxima at frequency ω_s and $\omega_o - \omega_s$.

The misalignment, which has a significant effect on the vertical spin component, had to be checked first. BMAD simulations were performed with

translations and rotations of dipole and quadrupole magnets individually. The position of the magnets (separately in x , y , and z directions) was altered randomly with a Gaussian distribution with a mean value equal to zero and a standard deviation of $\sigma = 1$ mm in all cases. Similarly, using a Gaussian distribution, magnets rotations (separately around x , y , and z axes) with a mean value of zero and a standard deviation of $\sigma_r = 1$ mrad are randomly changed. In addition, translation and rotational combinations have been separately analysed for dipole and quadrupole magnets, as well as for all magnets. The Fourier analysis of the induced vertical spin component $S_y(t)$ for each setting was performed. The Fourier amplitude spectra for each case show the pattern depicted in Figure 5.6. The Fourier amplitude spectrum for nonzero EDM only (without magnet misalignment) is also shown in this figure for comparison. The Fourier amplitude for magnet misalignments peaks at ω_s spin precession frequency and at $\omega_o - \omega_s$ frequency (ω_o is beam revolution frequency). The Fourier amplitude exhibits only one peak at ω_s frequency in the case of nonzero EDM without magnet misalignments.

Misalignment	Fourier Amplitudes			
	Dipole		Quadrupole	
	$F(\omega_s)$	$F(\omega_o - \omega_s)$	$F(\omega_s)$	$F(\omega_o - \omega_s)$
Translation x	$5 \cdot 10^{-14}$	$5 \cdot 10^{-15}$	$3 \cdot 10^{-14}$	$5 \cdot 10^{-15}$
Translation y	$2 \cdot 10^{-14}$	$2 \cdot 10^{-15}$	$2 \cdot 10^{-3}$	$4 \cdot 10^{-4}$
Translation z	$5 \cdot 10^{-14}$	$4 \cdot 10^{-15}$	$2 \cdot 10^{-14}$	$4 \cdot 10^{-16}$
Rotation x	$3 \cdot 10^{-14}$	$2 \cdot 10^{-15}$	$5 \cdot 10^{-14}$	$2 \cdot 10^{-15}$
Rotation y	$2 \cdot 10^{-4}$	$5 \cdot 10^{-5}$	$1 \cdot 10^{-5}$	$4 \cdot 10^{-6}$
Rotation z	$3 \cdot 10^{-5}$	$1 \cdot 10^{-5}$	$5 \cdot 10^{-14}$	$2 \cdot 10^{-16}$
All	$2 \cdot 10^{-4}$	$5 \cdot 10^{-5}$	$2 \cdot 10^{-3}$	$4 \cdot 10^{-4}$

Table 5.2: Fourier amplitudes for ω_s and $\omega_o - \omega_s$ frequencies and misalignments of different magnets. The results for every misalignment are the median values for 100 randomly distributed deviations.

The resulting Fourier amplitudes are presented in table 5.2 for frequencies ω_s and $\omega_o - \omega_s$. Quadrupole magnet misalignments clearly play the largest role because all misalignments at a time have the same total effect as those caused by quadrupole magnets alone. For dipole magnets, rotations around the y axis make the largest contribution to $S_y(t)$, while translations along the

y axis are the most important part of quadrupole magnet misalignments. All misalignments contribute coherently to $S_y(t)$, as they are not distinguishable, so $S_y(t)$ cannot be deconvolved and the information about every misalignment type and element cannot be obtained. In addition, misalignment and EDM effects are also indistinguishable, therefore only their coherent sum could be measured.

5.5.2 Effect Of Emittance On Vertical Spin Component

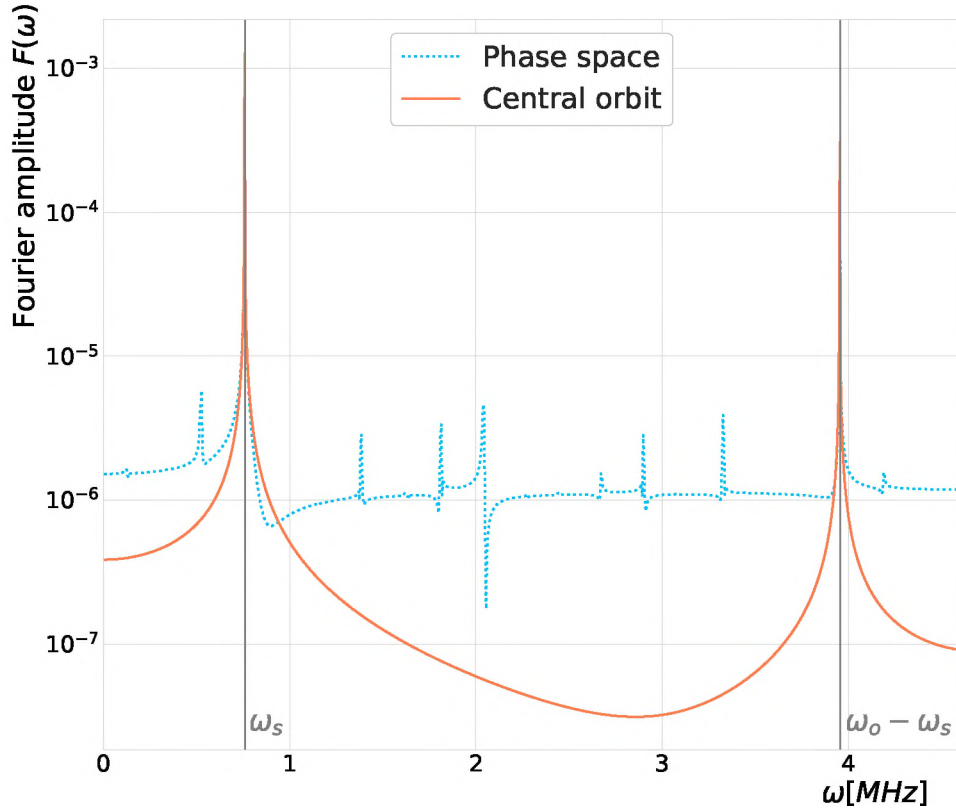


Figure 5.7: The comparison of the Fourier amplitude spectrum (denoted by a solid orange colour line) for a central trajectory and the summation of 81 points for the grid in the phase space (denoted by a sky blue dotted line).

Every particle is moving on their individual phase space ellipses. Particles that occupy the entire six-dimensional space, therefore, move along different trajectories and thus experience different magnetic fields. Therefore, if misalignments are present, it is mandatory to monitor the effect of emittance on $S_y(t)$. Calculations were performed for a initial transverse phase space (shown in figure 3.4) for a grid with $x = (0, \pm 1 \text{ mm})$, $x' = (0, \pm 1 \text{ mrad})$, $y = (0, \pm 1 \text{ mm})$, $y' = (0, \pm 1 \text{ mrad})$. An additional peaks appears in the Fourier amplitude spectrum for each nonzero phase space parameter. They are because of betatron oscillations of the particles which do not move on the central trajectory. Non-zero y' gives the largest side peaks, however, when comparing the Fourier amplitudes for the central trajectory, $F(\omega_s)$ and $F(\omega_o - \omega_s)$ change by 1%. The total of all the phase space points in the grid reduces the amplitude of the side peaks. The Fourier amplitudes $F(\omega_s)$ and $F(\omega_o - \omega_s)$ are very similar to those shown in figure 5.7 for the central trajectory.

5.5.3 Orbit Correction By Replacing Kickers With Dipole Magnets

Due to magnet misalignment, the close orbit deviates from its trajectory through all magnet centers. A correction system is thus necessary to ensure that the orbit is as close to the central (design) orbit as possible. This system consists of additional dipole magnets (steering magnets called steerers), which are used to direct the beam vertically and horizontally. To measure the position of the beam, beam position monitors (BPMs) in many different locations are necessary. The beam correction relies on minimizing the RMS (root mean square error) of the closed orbit by varying the steerer magnet strengths. The beam correction system works with a certain precision because steerers and BPMs are positioned with a certain precision and large portions of the orbit are not monitored. However, using this orbit correction method, the orbit deviations from the central orbit are reduced.

The BMAD simulations for COSY are described in detail in [89] using the orbit correction process [90, 91]. The orbit correction system of COSY in the horizontal plane consists of 22 steerers and 30 BPMs, while in the vertical plane there are 19 steerers and 29 BPMs. The orbit response due to steerer perturbations is linked to the magnetic field strength of the steerer

and can be summed up in the so-called orbit matrix. The matrix contains information on how the closed orbit is modified by a single steerer and can be used to determine the set of steerer strengths that result in an improved orbit.

A beam-based alignment procedure [88] has recently performed at COSY enabling to align all 56 magnetic centres of the quadrupole magnets with the use of 31 BPM. The beam was aligned with an accuracy of $40\text{ }\mu\text{m}$ with the centre of the quadrupole magnets, while the quadrupole magnets were precisely aligned to the design beam axis of precision $200\text{ }\mu\text{m}$ with this process.

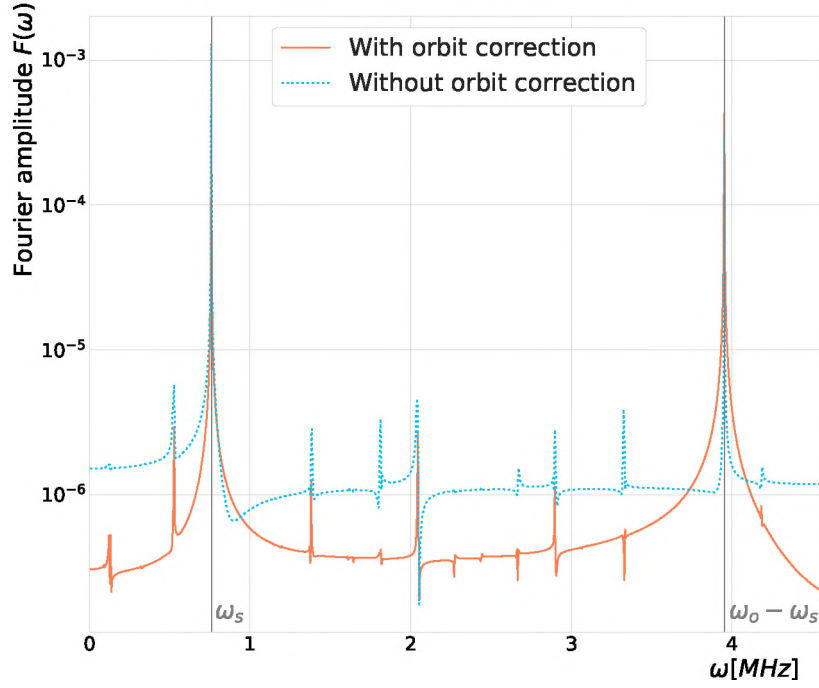


Figure 5.8: The comparison of the Fourier amplitude spectrum with (denoted by a orange coloured solid line) and without (denoted by a sky blue coloured dotted line) orbit correction applied for misalignment effect and for full phase space.

The effect of the orbit correction on the Fourier amplitudes has been examined using dipole magnets (kicker elements). Therefore, kickers affect not only the particle orbit but also influence the spin precession as well. The

orbit becomes more central as a result, and is less influenced by magnet misalignments. However, kickers introduce additional vertical and horizontal dipole fields which have an impact on the spin rotation. Dipole kickers were found to also exhibit undesired spin rotation as a result of misalignments. In 5.8, Fourier amplitudes are compared to evaluate the influence of the orbit correction on the spin $S_y(t)$ induced by misalignments. When applying orbit correction the Fourier amplitude $F(\omega_s)$ is reduced by a factor of about six, while the Fourier amplitude $F(\omega_o - \omega_s)$ remains unchanged after the orbit correction. Thus, orbit correction enhances the precision of the determination of EDM effect limits as the EDM effect contributes to the Fourier amplitude $F(\omega_s)$ only, whereas the misalignment effect can be deduced from the Fourier amplitude $F(\omega_o - \omega_s)$.

5.6 EDM Limit Determination Using Fourier Analysis

BMAD simulations were used to investigate the sensitivity of the proposed method of determining the experimental limit of the EDM value. For 10^4 randomly selected COSY magnet misalignment sets, calculations were performed. All misalignments of x , y , and z offsets and tilts about the x , y , and z -axis were considered for each quadrupole and dipole magnet. Using a Gaussian distribution, random values for magnet misalignments were generated with a mean equal to zero and standard deviations of $\sigma_x = \sigma_y = \sigma_z = 0.2$ mm for offset and for rotations, $\sigma_{x'} = \sigma_{y'} = \sigma_{z'} = 0.2$ mrad. Fourier amplitudes were shown to be unaffected by the phase space of the beam, as shown in section 5.5.2. Thus, only on the closed orbit, calculations were carried out. The orbit correction described in section 5.5.3 has been applied in each case. A Fourier analysis of the calculated vertical spin $S_y(t)$ time dependence was carried out for each set of misalignments. For each misalignment setting, calculations were carried out for EDM $D = 0, 10^{-20}, 10^{-19}, 5 \cdot 10^{-19}, 10^{-18}$ e-cm values. Similar calculations were also performed for quadrupole magnet misalignments (only translation in all directions), these misalignments were recently measured by the Vermessungsbüro Stollenwerk & Burghof [88]. In Table 5.3, for only a few EDM values, the results for the Fourier amplitudes are presented.

EDM value [e·cm]	$10^4 \cdot F(\omega_s)$	$10^4 \cdot F(\omega_o - \omega_s)$
0	0.65	1.73
10^{-20}	0.84	1.73
$5 \cdot 10^{-20}$	1.92	1.73
10^{-19}	3.14	1.73
$5 \cdot 10^{-19}$	15.58	1.73
10^{-18}	30.83	1.73
$5 \cdot 10^{-18}$	152.88	1.72
10^{-17}	305.45	1.71

Table 5.3: Fourier amplitudes for ω_s and $\omega_o - \omega_s$ frequencies and for some selected EDM values. The measured misalignments[88] of COSY quadrupole magnets were used, and an orbit correction was also applied.

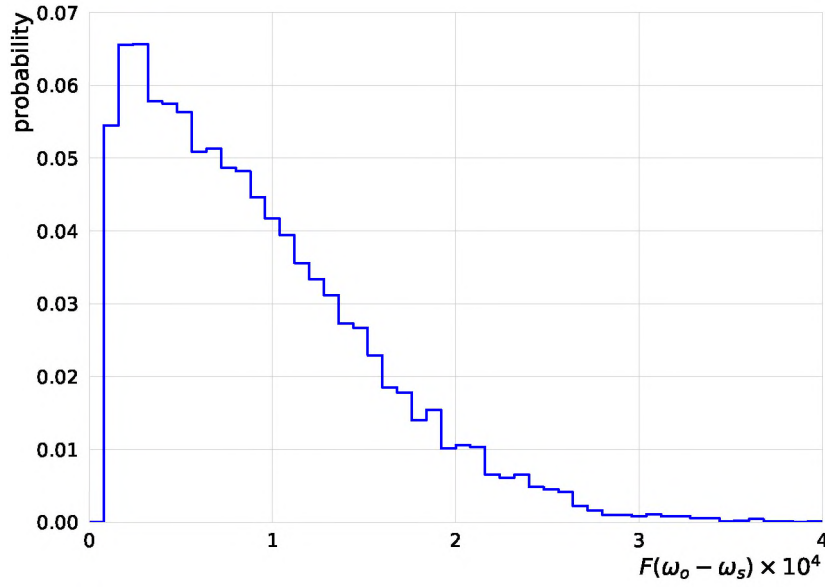


Figure 5.9: The probability distribution of Fourier amplitude $F(\omega_o - \omega_s)$, this Fourier amplitude is independent of EDM values.

As mentioned earlier, the $F(\omega_o - \omega_s)$ Fourier amplitude delivers information about the misalignment effect only. The data in Table 5.3 confirms the prediction made by the model. Figure 5.9 shows the probability distribution for Fourier amplitude $F(\omega_o - \omega_s)$ obtained using BMAD calculations for 10^4

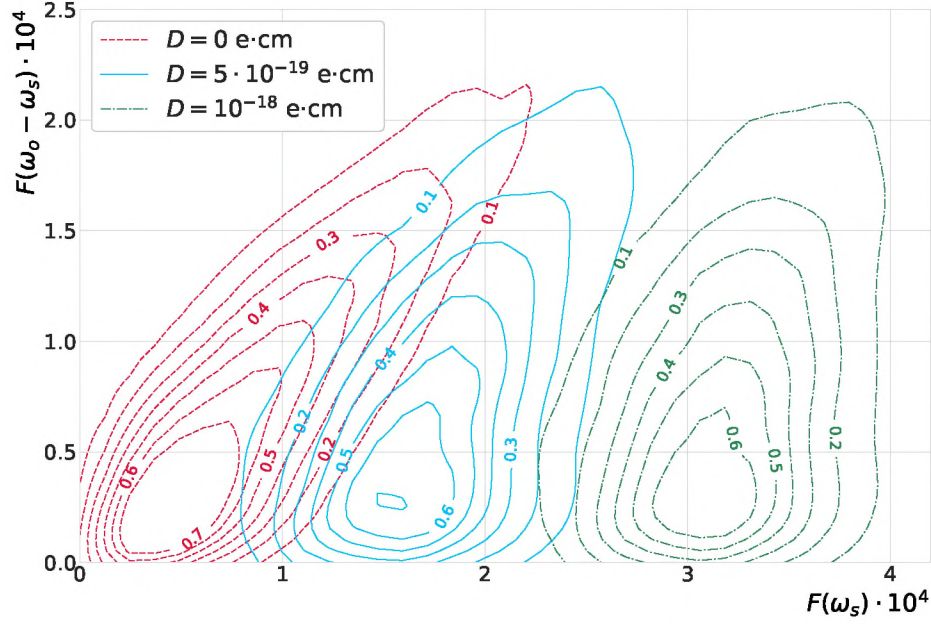


Figure 5.10: We can see the correlation of Fourier amplitudes $F(\omega_s)$ and $F(\omega_o - \omega_s)$ for different sets of EDM values, such as $D = 0$ e.cm (denoted by magenta dashed lines), $D = 5 \cdot 10^{-19}$ e.cm (blue solid lines) and $D = 10^{-18}$ e.cm (denoted by green dot-dashed lines.)

magnet misalignments. There is only one distribution visible, as it is independent of EDM, thus providing information on the misalignment effect that contributes also to Fourier amplitude $F(\omega_s)$.

Fourier amplitude $F(\omega_s)$ is the coherent sum of misalignment and EDM effects because they are indistinguishable. The method used to determine the EDM value limit is therefore based on the correlation of the Fourier amplitudes $F(\omega_s)$ and $F(\omega_o - \omega_s)$. In figure 5.10 one can see the correlation between Fourier amplitudes for various EDM values, such as $D = 0, 5 \cdot 10^{-19}, 10^{-18}$ e.cm. In the figure, we cannot see the results for $D = 10^{-20}, 10^{-19}$ e.cm as they overlap the distribution for $D = 0$ e.cm.

There is clear separation of Fourier amplitudes $F(\omega_s)$ for several EDM values, but it depends on the magnitude of Fourier amplitude $F(\omega_o - \omega_s)$. The distributions of $F(\omega_s)$ Fourier amplitude must therefore be checked for various

values of $F(\omega_o - \omega_s)$ amplitude. For selected ranges of $F(\omega_o - \omega_s)$ amplitude, probability distributions are shown in figure 5.11 for $F(\omega_s)$ amplitude. For small $F(\omega_o - \omega_s)$ amplitude values, it is observed that all probability distributions can be distinguished for EDM values such as $D = 0$, $5 \cdot 10^{-19}$, 10^{-18} e·cm. But for larger values of $F(\omega_o - \omega_s)$ amplitude, the separation becomes worse for $F(\omega_s)$ for different EDM values.

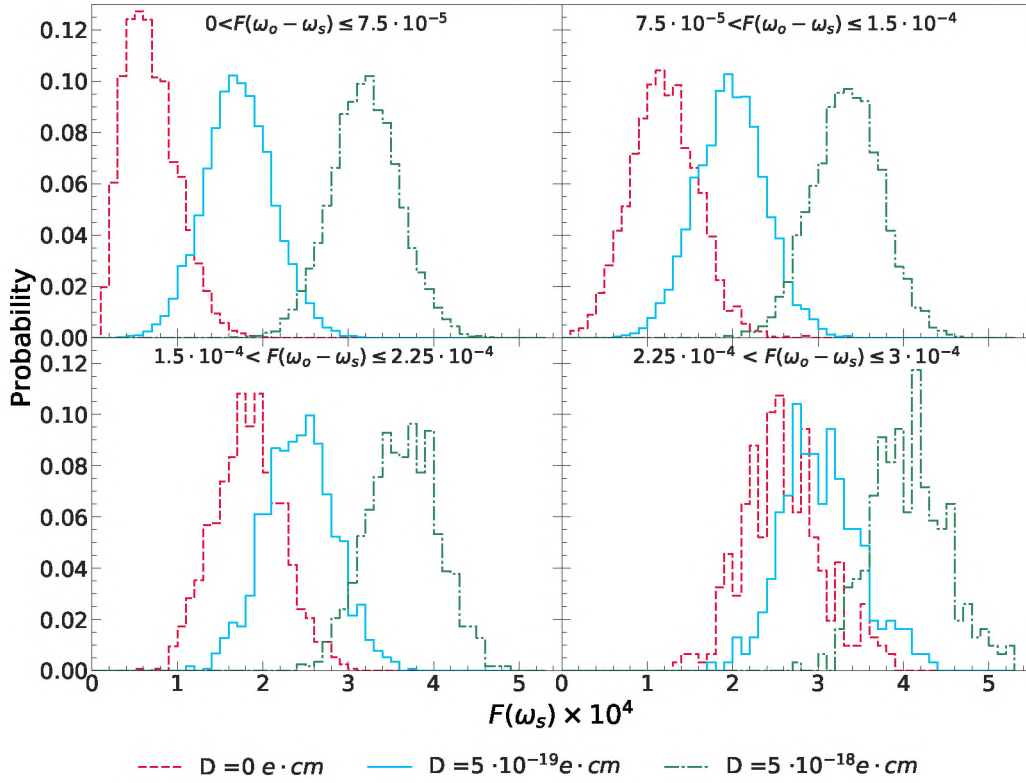


Figure 5.11: Probability distribution of Fourier amplitudes $F(\omega_s)$, for some selected intervals of $F(\omega_o - \omega_s)$ for different sets of EDM values $D = 0$ e·cm (denoted by magenta dashed lines), $D = 5 \cdot 10^{-19}$ e·cm (blue solid lines), and $D = 10^{-18}$ e·cm (denoted by green dot-dashed lines).

In the case of magnet misalignment, the experimental limit for EDM value could be determined well using the method discussed. For known misalign-

ments, their accuracy, and the different EDM values, the BMAD calculations must be performed with large statistics. The probability distributions for $F(\omega_s)$ amplitude could be obtained for the measured $F(\omega_o - \omega_s)$ amplitude within its exactness limit, similar to what is shown in figure 5.11. The upper limit of the EDM measured value can be determined by using these distributions for measured amplitude $F(\omega_s)$.

5.7 EDM Limit Determination Using Fourier Analysis And Slope Induced By Wien Filter

Furthermore, using the same distribution of 10^4 randomly selected COSY magnet misalignment described in section 5.6 for dipoles and quadrupoles the closed orbit calculation was carried out. The orbit correction described in section 5.5.3 has been applied in each case. Additionally, RF Wien Filter is used which is described in detail in [91], from where following equation is used to define the RF Wien filter field:

$$B_y = B_w \sin(2\pi f_{rev}|k + G\gamma| + \phi), \quad (5.12)$$

$$E_x = E_w \sin(2\pi f_{rev}|k + G\gamma| + \phi). \quad (5.13)$$

where B_y is RF Wien filter magnetic field, B_w is the magnitude of the magnetic field, k is the harmonic number, G is anomalous magnetic moment of deuteron, f_{rev} is the revolution frequency, ϕ is initial phase angle and γ is Lorentz factor. In calculation $\phi = \pi/2$, $k = 0$ and $B_w = 0.000024$ T was taken. The electric field magnitude was calculated using $E_w = B_w\beta c$, where β is beam relativistic speed. The buildup of the average vertical spin component can be seen as it is expected due to the RF fields of the Wien filter and slope of time dependence of vertical spin component $S_y(t)$ was calculated for each misalignment set. A Fourier analysis of the calculated time dependence of vertical spin component $S_y(t)$ was carried out for each set of misalignments.

The calculations were carried out for EDM $D = 0, 10^{-19}, 5 \cdot 10^{-19}, 10^{-18}$ e-cm values for each magnet misalignment setting. The correlation between slope and Fourier amplitude $F(\omega_s)$ for EDM values $D = 0, 5 \cdot 10^{-19}, 10^{-18}$

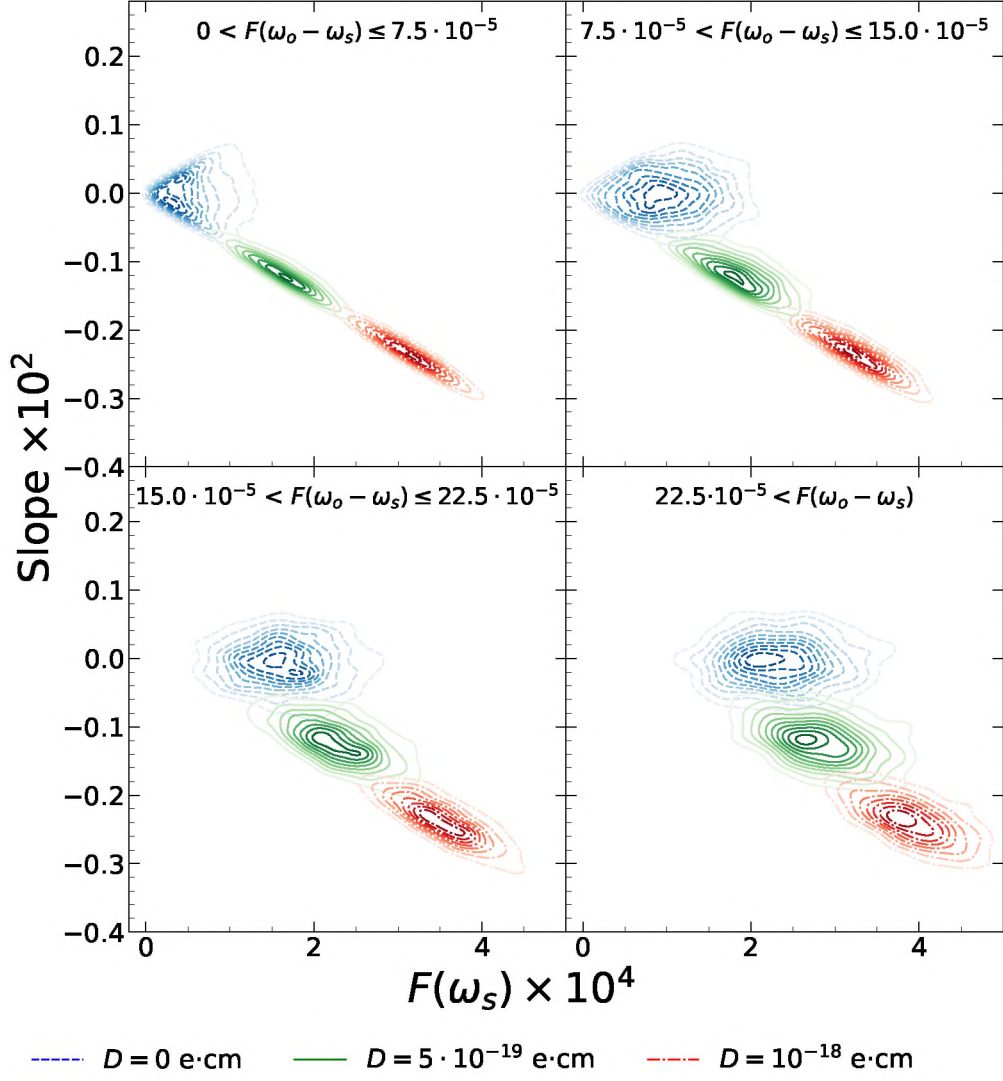


Figure 5.12: The correlation of slope and $F(\omega_s)$ Fourier amplitude for four ranges of $F(\omega_o - \omega_s)$ Fourier amplitude. In each plot the results for EDM values $D = 0 \text{ e}\cdot\text{cm}$ (blue dashed line), $D = 5 \cdot 10^{-19} \text{ e}\cdot\text{cm}$ (green solid line), and $D = 10^{-18} \text{ e}\cdot\text{cm}$ (red dash dotted line) are shown.

and four ranges of $F(\omega_o - \omega_s)$ Fourier amplitude is shown in the figure 5.12. In the figure, we cannot see the results for $D = 10^{-19} \text{ e}\cdot\text{cm}$ as it overlap with

the distribution of $D = 0$ e·cm. The further separation of EDM values as compared to that seen in figure 5.11 can be achieved using correlations of slope of time dependence of vertical spin and $F(\omega_s)$. It can be observed that for range $0 < F(\omega_o - \omega_s) \leq 7.5 \cdot 10^{-5}$ of Fourier amplitude, only a negative slope for EDM values $D = 5 \cdot 10^{-19}, 10^{-18}$ e·cm is seen. Further increasing $F(\omega_o - \omega_s)$ Fourier amplitude, the separation between distributions for EDM values $D = 0, 5 \cdot 10^{-19}, 10^{-18}$ e·cm becomes worse but it is better than shown in figure 5.11. For $D = 10^{-19}$ e·cm the results almost completely coincide with results for $D = 0$ e·cm. Therefore the sensitivity of the whole method allows to determine EDM limit to $D = 10^{-19}$ e·cm. This analysis using RF Wien filter further improve the method to determine upper limit of the EDM measurement. The EDM measured value can be determined by using this distribution of the measured slope of time dependence of vertical spin component and Fourier amplitude $F(\omega_s)$ for four ranges of $F(\omega_o - \omega_s)$.

5.8 Result And Conclusion

Measurement of the vertical polarisation for the initially horizontally polarised beam is used to measure the EDM of the charged particle using a storage ring. Since the expected EDM value is very small, all systematic uncertainties should be controlled and brought down to the minimum level possible. Unavoidable horizontal magnetic fields can lead to dominating systematic uncertainty. The misalignment of storage ring magnets generate these fields. These effects can be simulated with appropriate tracking codes for particles.

Through this thesis, we tried to develop a simple model that allows us to analytically determine how the horizontal magnetic field can contribute to vertical polarisation. The model is applicable to any field distribution described by Fourier series coefficients. The analytical formulae are given up to first order. Thus, it was possible to calculate the time dependence of the vertical spin component for a initially horizontally polarised beam moving within the magnetic field. Using the observation from analytical model (from section 5.4), we developed a method that allows us to control systematic uncertainties due to magnets misalignments and determine the limit of EDM value.

More detailed calculations were made using the BMAD software library, including dipole and quadrupole fields and their misalignments. The Fourier analysis of the obtained time dependence of the vertical spin component was performed and Fourier amplitudes for frequencies ω_s and $(\omega_o - \omega_s)$ were obtained. Due to EDM the Fourier amplitudes only have one peak at frequency ω_s . An additional peak was observed for misalignment at $(\omega_o - \omega_s)$ frequency. Further analysis are done on the basis of the correlation of these two Fourier amplitudes. The effects of all possible translations and rotations of dipole and quadrupole magnets were investigated. It was observed that the main misalignment effect was caused by quadrupole magnets shifts in the vertical direction, but the next important effect was due to dipole magnet rotation around the vertical axis which is one order of magnitude smaller. The impact of the phase space on the Fourier amplitudes was then investigated. It has been observed that extra peaks in the Fourier amplitude arise with particles not moving in the closed orbit. However, these side peaks are very significantly decreased for full phase space and the average amplitudes at ω_s and $(\omega_o - \omega_s)$ frequencies are equivalent to the closed orbit results. There was a discussion on the orbit correction approach, and this method was used to carry out calculations. Fourier amplitudes are compared to evaluate the influence of the orbit correction on the spin $S_y(t)$ induced by misalignments. It has been demonstrated that the orbit correction decreases the Fourier amplitude at ω_s but does not modify the Fourier amplitude at $(\omega_o - \omega_s)$. The EDM effect determination is improved since the EDM effect only contributes to the Fourier amplitude at the ω_s .

In the end, calculations were conducted for many randomly distributed dipole and quadrupole magnet misalignments for a few EDM values. It has been shown that a lower limit of $D < 10^{-19}$ e.cm for deuteron EDM value can be achieved with the present magnet positioning accuracy at COSY. The Fourier analysis allows us to differentiate between the EDM and the misalignment effect and show the strength of the suggested approach. The analysis using RF Wien filter further improve the method to determine upper limit of the EDM measurement. The upper limit of the EDM measured value can be determined using the correlation between slope and Fourier amplitude $F(\omega_s)$ for various EDM values. At present, this approach is the only one that permits the experimental verification of most important systematic uncertainties in EDM measurement with a storage ring.

Chapter 6

Summary

To explain the universe's asymmetry of matter and anti-matter asymmetry, the Sakharov conditions needed to be fulfilled. One of the important conditions is \mathcal{CP} symmetry violation. In chapter 2, it is explained how permanent EDM can lead to \mathcal{CP} violation and physics beyond the Standard Model. Various efforts are made in search of EDM for particle like muons, protons, etc. However, particles' upper limits are only known. JEDI collaboration is involved in one of such experiment to detect a permanent EDM of the proton with a sensitivity 10^{-29} e-cm. To achieve this level of sensitivity, it is very important to develop tools that consider dominant systematic uncertainties that can influence the vertical component. So it is essential to control them so that systematic uncertainties can be eventually pinned down to the smallest level possible. Two methods are introduced in this thesis for doing so. Both are devoted to finding a method through which we can control systematic uncertainties in EDM measurement, and which can be applicable to any lattice.

In the first method, Quasi Frozen Spin lattice is used. The numerical calculation for this method was performed using the BMAD tracking software. These calculation was done after implementing modifications in the tracking code, such as the TBMT equation extension to include the effect of MDM and EQM interactions with field gradient. Introduction of complex three-dimensional realistic electromagnetic fields, which satisfy Maxwell equations in the BMAD software. These realistic magnetic fields for multipoles and electromagnetic field for Wien Filter are introduced for interaction of MDM and EQM with field gradients. Particle and spin tracking are done after those modifications in the model and their influence on spin precession are

studied. In this method, the impact on the vertical spin component due to EQM interaction with field gradients was studied. Different sets of field values for the Wien filter allowed us to differentiate between impacts due to EDM and EQM interacting with field gradients on vertical spin polarisation. At slightly different Wien filter settings, the EDM impact is 7.2 times greater than the EQM effect for an EDM value of 10^{-29} e·cm. Therefore, the interaction between EQM and gradients may be used to understand the sources of the systematic uncertainties in EDM measurement. The deuteron EQM value is known with a precision of 10^{-3} , Therefore, reproducing the EQM value with the same precision level (10^{-3}) should control the systematic uncertainty in EDM measurement to 10^{-31} e·cm.

The second method is to evaluate the systematic uncertainties due to magnet misalignment in EDM measurement using a storage ring. Magnet misalignment is one of the major systematic uncertainty in EDM measurement experiments. To evaluate these magnet misalignment effects, analytical calculations using Mathematica software and numerical calculations using BMAD tracking software are presented in this thesis. The observation of Fourier analysis implies that the Fourier amplitude due to EDM has only one maximum at a frequency ω_s and maximum due to misalignment at frequency $\omega_o - \omega_s$. This Fourier analysis result made it possible to develop a method for determining the limits of the measured EDM value. Furthermore, a more detailed numerical calculation was performed using the BMAD software library for the COSY ring. The comparison of Fourier amplitude for frequency ω_s and $\omega_o - \omega_s$ was obtained. Which implies that the major misalignment effect is due to quadrupole magnet displacement in the vertical direction followed by dipole magnet rotation around the vertical axis.

Final calculations are performed with randomly distributed misalignments for quadrupoles and dipoles for EDM values $D = 0, 10^{-20}, 10^{-19}, 5 \cdot 10^{-19}, 10^{-18}$ e·cm. It was shown in section 5.6 that with present precision for magnet positioning at COSY it is possible to achieve a lower limit of $D < 10^{-19}$ e·cm for deuteron EDM value. Fourier analysis allows us to distinguish between the EDM and magnet misalignment effects. Further calculation is performed using RF Wien Filter and improvement of the method is demonstrated using the correlation between slope of time dependence of vertical spin component $S_y(t)$ and Fourier amplitude $F(\omega_s)$. The upper limit of EDM measured value can be determined using the correlation between slope and Fourier ampli-

tudes $F(\omega_s)$ with four ranges of $F(\omega_o - \omega_s)$ for various EDM values. At present, this method is the only one that permits the experimental verification of systematic uncertainties due to the magnet misalignments in the EDM measurements using a storage ring.

Bibliography

- [1] A. D. Sakharov, “Violation of CP-invariance, C-asymmetry, and baryon asymmetry of the Universe”, in *In the intermissions... Collected Works on Research into the Essentials of Theoretical Physics in Russian Federal Nuclear Center, Arzamas-16* (1998), pp. 84–87.
- [2] *JEDI Collaboration*, <http://collaborations.fz-juelich.de/ikp/jedi/>.
- [3] F. Abusaif et al., arXiv preprint arXiv:1912.07881, <https://doi.org/10.48550/arXiv.1912.07881> (2019).
- [4] D. J. Griffiths, *Introduction to Elementary Particles* (John Wiley & Sons, Ltd, 1987).
- [5] M. Sozzi, *Discrete symmetries and CP violation: From experiment to theory* (Oxford University Press, 2008).
- [6] T. D. Lee and C. N. Yang, Phys. Rev. **104**, 254 (1956).
- [7] C. S. Wu et al., Phys. Rev. **105**, 1413 (1957).
- [8] M. Goldhaber et al., Phys. Rev. **109**, 1015 (1958).
- [9] G. Backenstoss et al., Phys. Rev. Lett. **6**, 415 (1961).
- [10] A. Angelopoulos et al., Phys. Lett. B **444**, 43 (1998).
- [11] J. Schwinger, Phys. Rev. **82**, 914 (1951).
- [12] J. H. Christenson et al., Phys. Rev. Lett. **13**, 138 (1964).
- [13] N. Cabibbo, Phys. Rev. Lett. **10**, 531 (1963).
- [14] M. Kobayashi and T. Maskawa, Prog. Theor. Phys. **49**, 652 (1973).
- [15] B. Aubert et al. (BABAR Collaboration), Phys. Rev. Lett. **87**, 091801 (2001).
- [16] K. Abe et al. (Belle Collaboration), Phys. Rev. Lett. **87**, 091802 (2001).

- [17] I. B. Khriplovich and S. K. Lamoreaux, *CP Violation Without Strangeness: Electric Dipole Moments of Particles, Atoms, and Molecules* (Springer, Berlin, Heidelberg, 1997).
- [18] J. M. Pendlebury et al., Phys. Rev. D **92**, 092003 (2015).
- [19] J. Baron et al., Science **343**, 269 (2014).
- [20] W. C. Griffith et al., Phys. Rev. Lett. **102**, 101601 (2009).
- [21] G. W. Bennett et al. (Muon (g-2) Collaboration), Phys. Rev. D **80**, 052008 (2009).
- [22] J. H. Smith et al., Phys. Rev. **108**, 120 (1957).
- [23] F. J. M. Farley et al., Phys. Rev. Lett. **93**, 052001 (2004).
- [24] J. Pretz, Hyperfine Interact. **214**, 111 (2013).
- [25] T. Fukuyama, Int. J. Mod. Phys. A **27**, 1230015 (2012).
- [26] W. Dekens et al., J. High Energ. Phys. **2014**, 69 (2014).
- [27] R. Maier, Nucl. Instrum. Methods Phys. Res. A: Accel. Spectrom. Detect. Assoc. Equip **390**, 1 (1997).
- [28] Z. Bagdasarian et al., Phys. Rev. ST Accel. Beams **17**, 052803 (2014).
- [29] D. Eversmann et al. (JEDI Collaboration), Phys. Rev. Lett. **115**, 094801 (2015).
- [30] G. Guidoboni et al. (JEDI Collaboration), Phys. Rev. Lett. **117**, 054801 (2016).
- [31] N. Hempelmann et al. (JEDI Collaboration), Phys. Rev. Lett. **119**, 014801 (2017).
- [32] A. Saleev et al. (JEDI Collaboration), Phys. Rev. Accel. Beams **20**, 072801 (2017).
- [33] P. Lenisa and F. Rathmann, Nucl. Phys. News **27**, 10 (2017).
- [34] G. Guidoboni et al. (JEDI Collaboration), Phys. Rev. Accel. Beams **21**, 024201 (2018).
- [35] N. Hempelmann et al. (JEDI Collaboration), Phys. Rev. Accel. Beams **21**, 042002 (2018).
- [36] F. Rathmann et al., Phys. Rev. Accel. Beams **23**, 024601 (2020).

- [37] W. Hillert, in CAS - CERN Accelerator School 2019: Introduction to Accelerator Physics (July 2021).
- [38] V. Schmidt and A. Lehrach, J. Phys. Conf. Ser. **874**, 012051 (2017).
- [39] K. Wille, *The physics of particle accelerators: an introduction* (Clarendon Press, 2000).
- [40] J. Buon, in Cas,Cern Accelerator School 5 General Accelerator Physics Course (Sept. 1992), pp. 89–116.
- [41] B. J. Holzer, 10.5170/CERN-2013-007.27 (2014).
- [42] F. Tecker, Proceedings of the CAS-CERN Accelerator School: Advanced Accelerator Physics, 1 (2016).
- [43] D. Edwards and M. Syphers, “Acceleration and phase stability”, in *An introduction to the physics of high energy accelerators* (John Wiley & Sons, Ltd, 1993) Chap. 2, pp. 18–56.
- [44] G. Guidoboni, “Spin Coherence Time studies for a polarized deuteron beam at COSY”, PhD thesis (Universita degli Studi di Ferrara, 2013).
- [45] D. Sagan, Nucl. Instrum. Methods Phys. Res. A: Accel. Spectrom. Detect. Assoc. Equip. **558**, 356 (2006).
- [46] S. Y. Lee, *Spin Dynamics and Snakes in Synchrotrons* (World Scientific, 1997).
- [47] G. G. Ohlsen, Rep. Prog. Phys. **35**, 717 (1972).
- [48] M. H. Levitt, *Spin dynamics : basics of nuclear magnetic resonance*, 2nd ed. (John Wiley & Sons, 2008), p. 714.
- [49] NIST, <https://physics.nist.gov/cuu/Constants/>.
- [50] V. Bargmann et al., Phys. Rev. Lett. **2**, 435 (1959).
- [51] T. Fukuyama and A. J. Silenko, Int. J. Mod. Phys. A **28**, 1350147 (2013).
- [52] A. Y. Silenko, Russ. Phys. J. **48**, 788 (2005).
- [53] F. Abusaif et al. (CPEDM Collaboration), *Storage ring to search for electric dipole moments of charged particles: Feasibility study. Storage Ring to Search for Electric Dipole Moments of Charged Particles - Feasibility Study*, CERN Yellow Reports: Monographs (CERN, Geneva, Jan. 2021).

- [54] G. W. Bennett et al. (Muon (g-2) Collaboration), Phys. Rev. D **80**, 052008 (2009).
- [55] A. Lehrach et al., PoS **SPIN2018**, 144 (2019).
- [56] M. Rosenthal, “Experimental Benchmarking of Spin Tracking Algorithms for Electric Dipole Moment Searches at the Cooler Synchrotron COSY”, PhD Thesis (RWTH Aachen University, 2016), 208p.
- [57] A. Skawran and A. Lehrach, J. Phys. Conf. Ser. **874**, 012050 (2017).
- [58] A. A. Skawran, “Comparison of Frozen and Quasi Frozen Spin Concepts for a Deuteron Electrical Dipole Moment Storage Ring”, Master’s thesis (RWTH Aachen University, 2017), p. 80.
- [59] Y. Senichev et al., in (6th International Particle Accelerator Conference, Richmond, VA (USA), May 2015), pp. 213–215.
- [60] E. Valetov et al., in Proc. of International Computational Accelerator Physics Conference (ICAP’15), Shanghai, China, 12-16 October 2015, 12 (Feb. 2016), pp. 172–174.
- [61] W. M. Morse et al., Phys. Rev. ST Accel. Beams **16**, 114001 (2013).
- [62] D. J. Miller, Contemp. Phys. **55**, 148 (2014).
- [63] Y. F. Orlov et al., Phys. Rev. Lett. **96**, 214802 (2006).
- [64] J. Slim et al., Nucl. Instrum. Methods Phys. Res. A: Accel. Spectrom. Detect. Assoc. Equip. **828**, 116 (2016).
- [65] A. Aggarwal and A. Magiera, Acta Phys. Pol. B **51**, 373 (2020).
- [66] Y. Senichev and A. Aksentyev, J. Phys. Conf. Ser. **1686**, 012068 (2020).
- [67] P. J. Mohr et al., J. Phys. Chem. Ref. Data **37**, 1187 (2008).
- [68] D. M. Bishop and L. M. Cheung, Phys. Rev. A **20**, 381 (1979).
- [69] T. Ericson and M. Rosa-Clot, Nucl. Phys. A **405**, 497 (1983).
- [70] A. Magiera, Phys. Rev. Accel. Beams **20**, 094001 (2017).
- [71] B. D. Muratori et al., Phys. Rev. ST Accel. Beams **18**, 064001 (2015).
- [72] A. Magiera et al., J. Phys. G: Nucl. Part. Phys. **49**, 015004 (2021).
- [73] F. Müller, “Polarimeter Development for Electric Dipole Moment Measurements in Storage Rings”, PhD Thesis (RWTH Aachen, Aachen, 2019), p. 171.

- [74] H.-H. Adam et al. (WASA-at-COSY), arXiv, nucl-ex/0411038, 1 (2004).
- [75] I. Keshelashvili et al., J. Phys. Conf. Ser. **1162**, 012029 (2019).
- [76] F. Müller et al., J. Instrum. **15**, P12005 (2020).
- [77] R. Weidmann et al., Rev. Sci. Instrum. **67**, 1357 (1996).
- [78] A. Andres, “Polarisation Measurements for Storage Ring Electric Dipole Moment Investigations”, Master’s thesis (RWTH Aachen University, 2020), p. 85.
- [79] H. Stein et al., At. Energy **94**, 24 (2003).
- [80] R. A. Maier, Nucl. Phys. News **7**, 5 (1997).
- [81] V. Bocharov et al., AIP Conf. Proc. **821**, 308 (2006).
- [82] V. Kamerdzhev et al., in Proc. 5th International Particle Accelerator Conference (IPAC’14), Dresden, Germany, June 15-20, 2014, International Particle Accelerator Conference 5 (July 2014), pp. 765–767.
- [83] D. Prasuhn et al., Nucl. Instrum. Methods Phys. Res. A: Accel. Spectrom. Detect. Assoc. Equip. **441**, 167 (2000).
- [84] D. Möhl et al., Phys. Rep. **58**, 73 (1980).
- [85] V. S. Morozov et al., Phys. Rev. ST Accel. Beams **7**, 024002 (2004).
- [86] Y. S. Derbenev and A. M. Kondratenko, Zh. Eksp. Teor. Fiz. **64**, 1918 (1973).
- [87] P. Benati et al., Phys. Rev. ST Accel. Beams **15**, 124202 (2012).
- [88] T. Wagner et al., J. Instrum. **16**, T02001 (2021).
- [89] V. Schmidt, “Analysis of Closed-Orbit Deviations for a first direct Deuteron Electric Dipole Moment Measurement at the Cooler Synchrotron COSY”, Master’s thesis (RWTH Aachen University, 2017), 91 p.
- [90] Y. Chung et al., in Proceedings of International Conference on Particle Accelerators (IEEE, 1993), 2263–2265 vol.3.
- [91] V. Poncza, “Extensive optimization of a simulation model for the electric dipole moment measurement at the Cooler Synchrotron COSY”, PhD thesis (RWTH Aachen University, Aachen, 2021), p. 1.

Appendix A

Derivatives For Quadrupole For The Full Half-Symmetric Function

$$\begin{aligned}
\frac{\partial B_x}{\partial x} &= \frac{i(1+b^2)}{8(1-b^2)} \left(-\frac{e^{-i\bar{h}+\sqrt{2}z}}{1+e^{-i\bar{h}+\sqrt{2}z}} - \frac{e^{i\bar{h}+\sqrt{2}z}}{1+e^{i\bar{h}+\sqrt{2}z}} + \frac{e^{-ih+\sqrt{2}z}}{1+e^{-ih+\sqrt{2}z}} + \frac{e^{ih+\sqrt{2}z}}{1+e^{ih+\sqrt{2}z}} \right) \\
&\quad + \frac{i}{8} \left(\frac{e^{-i\bar{h}_2+\sqrt{2}z}}{1+e^{-i\bar{h}_2+\sqrt{2}z}} + \frac{e^{i\bar{h}_2+\sqrt{2}z}}{1+e^{i\bar{h}_2+\sqrt{2}z}} - \frac{e^{-ih_2+\sqrt{2}z}}{1+e^{-ih_2+\sqrt{2}z}} - \frac{e^{ih_2+\sqrt{2}z}}{1+e^{ih_2+\sqrt{2}z}} \right), \\
\frac{\partial B_x}{\partial y} &= 1 - \frac{1}{8} \left(\frac{e^{-i\bar{h}+\sqrt{2}z}}{1+e^{-i\bar{h}+\sqrt{2}z}} + \frac{e^{i\bar{h}+\sqrt{2}z}}{1+e^{i\bar{h}+\sqrt{2}z}} + \frac{e^{-ih+\sqrt{2}z}}{1+e^{-ih+\sqrt{2}z}} + \frac{e^{ih+\sqrt{2}z}}{1+e^{ih+\sqrt{2}z}} \right) \\
&\quad + \left(\frac{i(1+b^2)}{8(1-b^2)} \right) \left(\frac{e^{-i\bar{h}_2+\sqrt{2}z}}{1+e^{-i\bar{h}_2+\sqrt{2}z}} + \frac{e^{i\bar{h}_2+\sqrt{2}z}}{1+e^{i\bar{h}_2+\sqrt{2}z}} + \frac{e^{-ih_2+\sqrt{2}z}}{1+e^{-ih_2+\sqrt{2}z}} + \frac{e^{ih_2+\sqrt{2}z}}{1+e^{ih_2+\sqrt{2}z}} \right), \\
\frac{\partial B_x}{\partial z} &= \left(\frac{b}{4(1-b^2)} \right) \left(\frac{e^{-i\bar{h}+\sqrt{2}z}}{1+e^{-i\bar{h}+\sqrt{2}z}} - \frac{e^{i\bar{h}+\sqrt{2}z}}{1+e^{i\bar{h}+\sqrt{2}z}} - \frac{e^{-ih+\sqrt{2}z}}{1+e^{-ih+\sqrt{2}z}} + \frac{e^{ih+\sqrt{2}z}}{1+e^{ih+\sqrt{2}z}} \right) \\
&\quad + \left(\frac{ib}{4(1-b^2)} \right) \left(-\frac{e^{-i\bar{h}_2+\sqrt{2}z}}{1+e^{-i\bar{h}_2+\sqrt{2}z}} + \frac{e^{i\bar{h}_2+\sqrt{2}z}}{1+e^{i\bar{h}_2+\sqrt{2}z}} - \frac{e^{-ih_2+\sqrt{2}z}}{1+e^{-ih_2+\sqrt{2}z}} + \frac{e^{ih_2+\sqrt{2}z}}{1+e^{ih_2+\sqrt{2}z}} \right).
\end{aligned}
\tag{A.1}$$

$$\begin{aligned}
\frac{\partial B_y}{\partial x} &= 1 - \left(\frac{(1+b^2)}{8(1-b^2)} \right) \left(\frac{e^{-i\bar{h}+\sqrt{2}z}}{1+e^{-i\bar{h}+\sqrt{2}z}} + \frac{e^{i\bar{h}+\sqrt{2}z}}{1+e^{i\bar{h}+\sqrt{2}z}} + \frac{e^{-ih+\sqrt{2}z}}{1+e^{-ih+\sqrt{2}z}} + \frac{e^{ih+\sqrt{2}z}}{1+e^{ih+\sqrt{2}z}} \right) \\
&\quad - \frac{1}{8} \left(\frac{e^{-i\bar{h}_2+\sqrt{2}z}}{1+e^{-i\bar{h}_2+\sqrt{2}z}} + \frac{e^{i\bar{h}_2+\sqrt{2}z}}{1+e^{i\bar{h}_2+\sqrt{2}z}} + \frac{e^{-ih_2+\sqrt{2}z}}{1+e^{-ih_2+\sqrt{2}z}} + \frac{e^{ih_2+\sqrt{2}z}}{1+e^{ih_2+\sqrt{2}z}} \right), \\
\frac{\partial B_y}{\partial y} &= \frac{i}{8} \left(\frac{e^{-i\bar{h}+\sqrt{2}z}}{1+e^{-i\bar{h}+\sqrt{2}z}} + \frac{e^{i\bar{h}+\sqrt{2}z}}{1+e^{i\bar{h}+\sqrt{2}z}} - \frac{e^{-ih+\sqrt{2}z}}{1+e^{-ih+\sqrt{2}z}} - \frac{e^{ih+\sqrt{2}z}}{1+e^{ih+\sqrt{2}z}} \right) \\
&\quad + \frac{i(1+b^2)}{8(1-b^2)} \left(-\frac{e^{-i\bar{h}_2+\sqrt{2}z}}{1+e^{-i\bar{h}_2+\sqrt{2}z}} - \frac{e^{i\bar{h}_2+\sqrt{2}z}}{1+e^{i\bar{h}_2+\sqrt{2}z}} + \frac{e^{-ih_2+\sqrt{2}z}}{1+e^{-ih_2+\sqrt{2}z}} + \frac{e^{ih_2+\sqrt{2}z}}{1+e^{ih_2+\sqrt{2}z}} \right), \\
\frac{\partial B_y}{\partial z} &= \left(\frac{ib}{4(1-b^2)} \right) \left(-\frac{e^{-i\bar{h}+\sqrt{2}z}}{1+e^{-i\bar{h}+\sqrt{2}z}} + \frac{e^{i\bar{h}+\sqrt{2}z}}{1+e^{i\bar{h}+\sqrt{2}z}} - \frac{e^{-ih+\sqrt{2}z}}{1+e^{-ih+\sqrt{2}z}} + \frac{e^{ih+\sqrt{2}z}}{1+e^{ih+\sqrt{2}z}} \right) \\
&\quad + \left(\frac{b}{4(1-b^2)} \right) \left(\frac{e^{-i\bar{h}_2+\sqrt{2}z}}{1+e^{-i\bar{h}_2+\sqrt{2}z}} - \frac{e^{i\bar{h}_2+\sqrt{2}z}}{1+e^{i\bar{h}_2+\sqrt{2}z}} - \frac{e^{-ih_2+\sqrt{2}z}}{1+e^{-ih_2+\sqrt{2}z}} + \frac{e^{ih_2+\sqrt{2}z}}{1+e^{ih_2+\sqrt{2}z}} \right). \tag{A.2}
\end{aligned}$$

$$\begin{aligned}
\frac{\partial B_z}{\partial x} &= \left(\frac{b}{4(1-b^2)} \right) \left(\frac{e^{-i\bar{h}+\sqrt{2}z}}{1-e^{-i\bar{h}+\sqrt{2}z}} - \frac{e^{i\bar{h}+\sqrt{2}z}}{1+e^{i\bar{h}+\sqrt{2}z}} + \frac{e^{-ih+\sqrt{2}z}}{1+e^{-ih+\sqrt{2}z}} - \frac{e^{ih+\sqrt{2}z}}{1+e^{ih+\sqrt{2}z}} \right) \\
&\quad - \left(\frac{ib}{4(1+b^2)} \right) \left(\frac{e^{-i\bar{h}_2+\sqrt{2}z}}{1+e^{-i\bar{h}_2+\sqrt{2}z}} - \frac{e^{i\bar{h}_2+\sqrt{2}z}}{1+e^{i\bar{h}_2+\sqrt{2}z}} + \frac{e^{-ih_2+\sqrt{2}z}}{1+e^{-ih_2+\sqrt{2}z}} - \frac{e^{ih_2+\sqrt{2}z}}{1+e^{ih_2+\sqrt{2}z}} \right), \\
\frac{\partial B_z}{\partial y} &= \left(\frac{-ib}{4(1+b^2)} \right) \left(\frac{e^{-i\bar{h}+\sqrt{2}z}}{1-e^{-i\bar{h}+\sqrt{2}z}} - \frac{e^{i\bar{h}+\sqrt{2}z}}{1+e^{i\bar{h}+\sqrt{2}z}} + \frac{e^{-ih+\sqrt{2}z}}{1+e^{-ih+\sqrt{2}z}} - \frac{e^{ih+\sqrt{2}z}}{1+e^{ih+\sqrt{2}z}} \right) \\
&\quad + \left(\frac{b}{4(1-b^2)} \right) \left(\frac{e^{-i\bar{h}_2+\sqrt{2}z}}{1+e^{-i\bar{h}_2+\sqrt{2}z}} - \frac{e^{i\bar{h}_2+\sqrt{2}z}}{1+e^{i\bar{h}_2+\sqrt{2}z}} + \frac{e^{-ih_2+\sqrt{2}z}}{1+e^{-ih_2+\sqrt{2}z}} - \frac{e^{ih_2+\sqrt{2}z}}{1+e^{ih_2+\sqrt{2}z}} \right), \\
\frac{\partial B_z}{\partial z} &= \frac{1}{2} \left(-\frac{ib^2}{(1-b^4)} \right) \left(-\frac{e^{-i\bar{h}+\sqrt{2}z}}{1+e^{-i\bar{h}+\sqrt{2}z}} - \frac{e^{i\bar{h}+\sqrt{2}z}}{1+e^{i\bar{h}+\sqrt{2}z}} + \frac{e^{-ih+\sqrt{2}z}}{1+e^{-ih+\sqrt{2}z}} + \frac{e^{ih+\sqrt{2}z}}{1+e^{ih+\sqrt{2}z}} \right) \\
&\quad - \left(\frac{ib^2}{(1-b^4)} \right) \left(\frac{-e^{-i\bar{h}_2+\sqrt{2}z}}{1+e^{-i\bar{h}_2+\sqrt{2}z}} - \frac{e^{i\bar{h}_2+\sqrt{2}z}}{1+e^{i\bar{h}_2+\sqrt{2}z}} + \frac{e^{-ih_2+\sqrt{2}z}}{1+e^{-ih_2+\sqrt{2}z}} + \frac{e^{ih_2+\sqrt{2}z}}{1+e^{ih_2+\sqrt{2}z}} \right). \tag{A.3}
\end{aligned}$$

Where,

$$\bar{h} = \frac{1}{\sqrt{2}} \left(\frac{1}{b} + b \right) x - \frac{i}{\sqrt{2}} \left(\frac{1}{b} - b \right) y, \quad (\text{A.4})$$

$$h = \frac{1}{\sqrt{2}} \left(\frac{1}{b} + b \right) x + \frac{i}{\sqrt{2}} \left(\frac{1}{b} - b \right) y, \quad (\text{A.5})$$

$$\bar{h}_2 = \frac{1}{\sqrt{2}} \left(\frac{1}{b} + b \right) y - \frac{i}{\sqrt{2}} \left(\frac{1}{b} - b \right) x, \quad (\text{A.6})$$

$$h_2 = \frac{1}{\sqrt{2}} \left(\frac{1}{b} + b \right) y + \frac{i}{\sqrt{2}} \left(\frac{1}{b} - b \right) x. \quad (\text{A.7})$$